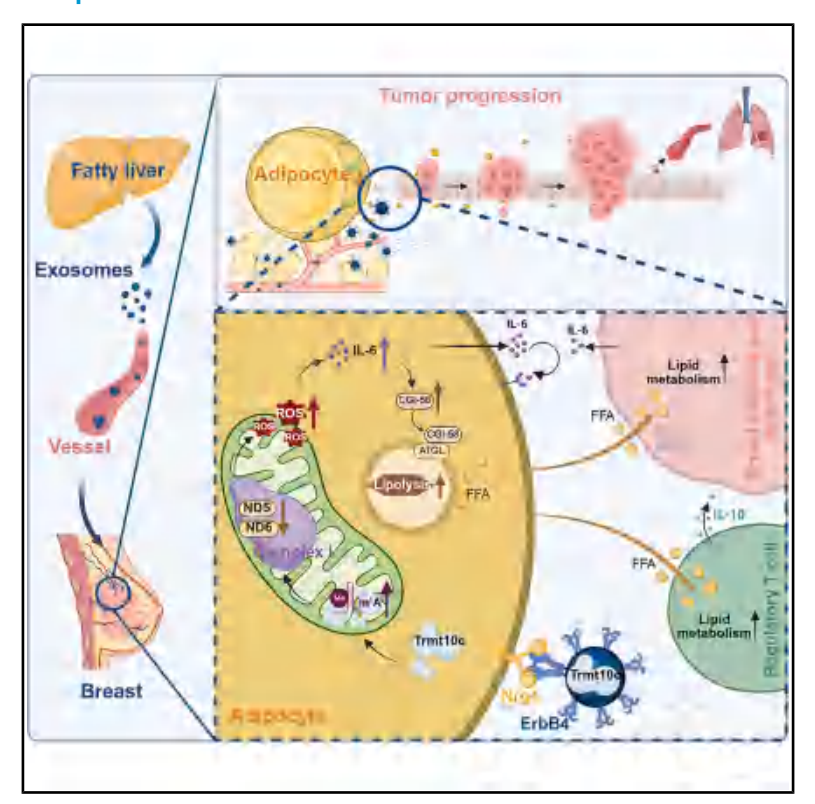
# Liver-breast communication of adipocyte-oriented exosomes drives primary mammary cancer progression

# **Graphical abstract**



# **Authors**

Chunni Li, Yiwen Lu, Yihong Li, ..., Jin Jin, Dongming Kuang, Shicheng Su

# Correspondence

sushch@mail.sysu.edu.cn

# In brief

Li et al. demonstrate that fatty livers foster a favorable metabolic landscape for breast cancer via adipocyte-oriented exosomes. These exosomes display tropism to mammary adipocytes through the ErbB4-Nrg4 axis. Exosomal TRMT10C triggers adipocyte ROS production, boosts IL-6 secretion, and subsequently enhances free fatty acid release, thereby facilitating tumor initiation and growth.

# **Highlights**

- Fatty livers promote breast cancer by releasing mammary adipocyte-tropic exosomes
- An ErbB4-Nrg4 axis determines adipocyte tropism of fatty liver exosomes
- Exosomal TRMT10C induces adipocyte FFA release via mitochondrial mRNA m<sup>1</sup>A modification
- ErbB4<sup>+</sup> exosomes predict the prognosis of patients with breast cancer and comorbid NAFLD



# **Article**

# Liver-breast communication of adipocyte-oriented exosomes drives primary mammary cancer progression

Chunni Li,<sup>1,2,14</sup> Yiwen Lu,<sup>1,2,14</sup> Yihong Li,<sup>1,2,14</sup> Ting Liu,<sup>3,14</sup> Hong Deng,<sup>4,14</sup> Mingchao Gao,<sup>5</sup> Boxuan Zhou,<sup>6</sup> Jiayu Liu,<sup>1,2</sup> Junchao Cai,<sup>7</sup> Di Huang,<sup>1,2</sup> Linbin Yang,<sup>1,2</sup> Jin Jin,<sup>8</sup> Dongming Kuang,<sup>9</sup> and Shicheng Su<sup>1,2,3,10,11,12,13,15,\*</sup>

<sup>1</sup>Guangdong Provincial Key Laboratory of Malignant Tumor Epigenetics and Gene Regulation, Medical Research Center, Sun Yat-Sen Memorial Hospital, Sun Yat-Sen University, Guangzhou 510120, China

# **SUMMARY**

The incidence of certain types of extrahepatic cancers significantly increases in nonalcoholic fatty liver disease (NAFLD), the mechanisms of which are elusive. Here, we demonstrate that NAFLD is correlated with a higher risk of breast cancer in individuals with atypical hyperplasia and poor prognosis in patients with breast cancer. In mice, fatty liver exosomes are preferentially accumulated in adipocytes, and their enrichment in mammary adipocytes fosters a pro-tumor breast microenvironment. Adipocyte tropism is dictated by the binding of exosomal ErbB4 to neuregulin 4 (Nrg4). tRNA methyltransferase 10 homolog C (TRMT10C) in fatty liver exosomes translocates to mitochondria and inhibits Nd5 and Nd6 mRNA translation by inducing  $N^1$ -methyladenosine modifications in adipocytes. ND5 and ND6 reduction increases reactive oxygen species and consequently enhances free fatty acid release, which fuels tumor progression. Plasma ErbB4<sup>+</sup> exosomes are an independent prognostic factor for patients with breast cancer and comorbid NAFLD. Collectively, we reveal a liver-breast metabolic remote interaction that drives cancer development.

### INTRODUCTION

Nonalcoholic fatty liver disease (NAFLD) impacts approximately 30% of adults worldwide. <sup>1-3</sup> It is the fastest-increasing etiology of hepatocellular carcinoma. <sup>4</sup> Furthermore, the incidences of certain types of extrahepatic cancers also increase in NAFLD. <sup>2</sup> However, its underlying mechanisms are elusive. <sup>2</sup> The prevailing hypothesis is that NAFLD concurrent metabolic disorders, such as obesity and insulin resistance, are attributed to the development of extrahepatic cancers. However, over 40% of NAFLD individuals are non-obese, <sup>5</sup> and NAFLD itself is an independent

risk factor of extrahepatic cancers distinct from other metabolic factors. <sup>2,6</sup> Moreover, a large cohort study shows that breast cancer is the sole extrahepatic cancer significantly associated with NAFLD in females, especially in non-obese individuals. <sup>7</sup> These clinical findings raise a question of whether there is a specific interaction between fatty livers and breast cancer beyond the known general factors.

The major cell type in breast is adipocytes that store and release free fatty acids (FFAs).<sup>8,9</sup> Moreover, breast carcinogenesis is regulated by fat tissues in which breast epithelial cells are embedded.<sup>10</sup> Along with cytokines, elevated lipolysis in

<sup>&</sup>lt;sup>2</sup>Breast Tumor Center, Sun Yat-Sen Memorial Hospital, Sun Yat-Sen University, Guangzhou 510120, China

<sup>&</sup>lt;sup>3</sup>School of Basic Medical Sciences, Southern Medical University, Guangzhou 510515, China

<sup>&</sup>lt;sup>4</sup>Department of Infectious Diseases, the Third Affiliated Hospital, Sun Yat-Sen University, Guangzhou 510630, China

<sup>&</sup>lt;sup>5</sup>Department of Urology, Sun Yat-Sen Memorial Hospital, Sun Yat-Sen University, Guangzhou 510120, China

Department of Breast Disease Center, the First Affiliated Hospital, Nanchang University, Nanchang 330006, China

<sup>&</sup>lt;sup>7</sup>Zhongshan School of Medicine, Sun Yat-Sen University, Guangzhou 510080, China

<sup>&</sup>lt;sup>8</sup>Center for Neuroimmunology and Health Longevity, the Third Affiliated Hospital, Sun Yat-Sen University, Guangzhou 510630, China

<sup>&</sup>lt;sup>9</sup>Guangdong Province Key Laboratory of Pharmaceutical Functional Genes, MOE Key Laboratory of Gene Function and Regulation, School of Life Sciences, Sun Yat-Sen University, Guangzhou 510275, China

<sup>&</sup>lt;sup>10</sup>New Cornerstone Science Laboratory, Sun Yat-Sen University, Guangzhou 510080, China

<sup>&</sup>lt;sup>11</sup>Biotherapy Center, Sun Yat-Sen Memorial Hospital, Sun Yat-Sen University, Guangzhou 510120, China

<sup>&</sup>lt;sup>12</sup>Department of Immunology, Zhongshan School of Medicine, Sun Yat-Sen University, Guangzhou 510080, China

<sup>&</sup>lt;sup>13</sup>State Key Laboratory of Medical Proteomics, Beijing Proteome Research Center, National Center for Protein Sciences, Beijing Institute of Lifeomics, Beijing 102200, China

<sup>&</sup>lt;sup>14</sup>These authors contributed equally

<sup>15</sup>Lead contact

<sup>\*</sup>Correspondence: sushch@mail.sysu.edu.cn https://doi.org/10.1016/j.cmet.2025.08.012



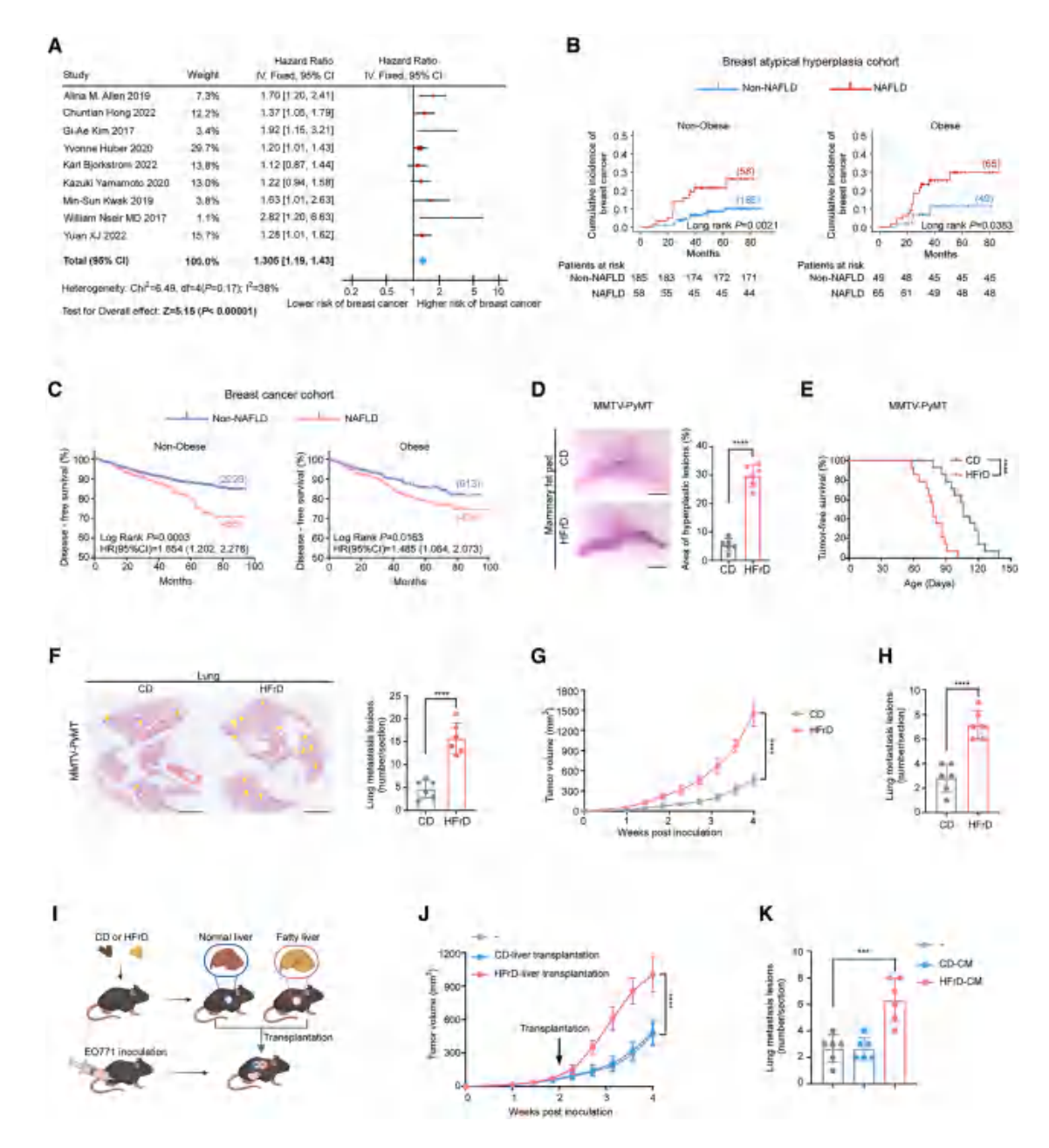


Figure 1. NAFLD increases the risk of breast cancer in humans and mice

- (A) Forest plots and combined estimates of the effect of NAFLD on breast cancer occurrence in the general population (n = 9 studies).
- (B) Cumulative breast cancer incidence in patients with breast atypical hyperplasia who did or did not have concomitant NAFLD.
- (C) Kaplan-Meier survival curves for DFS of patients with breast cancer stratified by obesity status.
- (D) Representative whole-mount carmine staining images (left) and the percentage of the hyperplastic lesion area (right) in mammary fat pads harvested from MMTV-PyMT mice fed either a control diet (CD) or a high-fructose diet (HFrD) (n = 6 mice per group). LN, lymph node. Scale bars, 5 mm.
- (E) Kinetics of mammary tumor onset in MMTV-PyMT mice fed either CD or HFrD (n = 14 mice per group).
- (F) Representative hematoxylin and eosin (H&E) staining images of lung metastases (left) and quantification (right) in MMTV-PyMT mice fed either CD or HFrD (n = 6 mice per group). Scale bars, 2.5 mm.
- (G and H) C57BL/6 mice fed either CD or HFrD were inoculated with EO771 cells (n = 6 mice per group).
- (G) Tumor growth curves.
- (H) Quantification of lung metastasis.

(I and J) Mice fed either CD or HFrD were used as liver transplantation donors. CD-fed mice bearing EO771 grafts were transplanted with or without normal or fatty livers (n = 6 mice per group). Experimental schematic (I) and tumor growth curves (J) are shown.

(legend continued on next page)

# **Article**



adipocytes fuels the initiation and progression of cancer cells via releasing FFAs. 11,12

Extracellular vesicles (EVs), which consist of microvesicles and exosomes, regulate inter-organ communication via their cargo. <sup>13–15</sup> EVs also mediate intercellular transfer of mitochondria, which regulates systemic metabolic homeostasis. <sup>16,17</sup> Circulating EVs exhibit organotropism, which is directed by their transmembrane proteins. <sup>18,19</sup> EVs from primary tumors orchestrate pre-metastatic niches, which are permissive for the colonization of metastatic cancer cells. <sup>19</sup> The latest data demonstrate that tumor-derived EVs impair metabolic functions of livers. <sup>20</sup> However, whether dysfunction of a distant organ can conversely induce a pro-tumorigenic milieu in the primary site remains largely unclear.

Here, we revealed that fatty livers transmit signals of lipid metabolic disorders to breast via mitochondrion-locating methyltransferase encapsulated in mammary adipose-tropic exosomes, which accelerates initiation and progression of breast cancer.

### **RESULTS**

# NAFLD is associated with human breast cancer independent of obesity

A historical cohort study including 25,947 individuals shows that breast cancer is the sole extrahepatic cancer significantly associated with NAFLD in females.7 To validate the connection between NAFLD and breast cancer in a larger population, we searched the PubMed, Embase, Web of Science, and Scopus databases in the meta-analysis. The cohort comprised eleven studies involving 141,273 females, including 5,532 patients with breast cancer (Figure S1A; Table S1). Nine present incidence data in the general population, and two provide survival data in patients with breast cancer. The Newcastle-Ottawa quality assessment scale (NOS) score indicated that all eleven studies have high quality (Table S1). Meta-analysis showed a significant correlation between NAFLD and an elevated risk of incidence of breast cancer in the general population (Figure 1A) and worse recurrence-free survival (RFS) in patients with breast cancer (Figure S1B).

To further confirm this observation, we recruited a cohort comprising 357 patients with breast atypical hyperplasia. Among them, 123 (34.45%) had NAFLD (Table S2). The risk of developing breast cancer was significantly higher in patients with NAFLD (p value for trend < 0.0001; HR = 3.442, 95% confidence interval [CI]: 1.918–6.177, p < 0.0001) (Figure S1C). Because NAFLD was strongly associated with obesity, which promotes tumor progression, p we categorized participants into two groups: obese (body mass index [BMI] p 25 kg/m²) and nonobese (BMI < 25 kg/m²). p NAFLD showed a significant association with an increased incidence of breast cancer in both obese (p value for trend = 0.0383; HR = 2.993, 95% CI: 1.007–8.897, p = 0.0486) and non-obese (p value for trend = 0.0021; HR = 3.085,

95% CI: 1.450-6.566, p = 0.0035) subjects with breast atypical hyperplasia (Figure 1B).

Furthermore, we evaluated the prognostic value of NAFLD in 3,781 patients with breast cancer. Among them, 942 patients were diagnosed with NAFLD (Table S3). Patients with NAFLD had shorter disease-free survival (DFS), but not overall survival (OS), than those without NAFLD (Figures S1D and S1E), which is in agreement with previous studies. 23,24 Consistent with future incident breast cancer in patients with atypical hyperplasia, the sub-stratified analysis revealed that NAFLD was significantly correlated with worse DFS in both obese and non-obese subgroups (Figure 1C). Patients with NAFLD have higher levels of fasting plasma glucose (FPG).25 All participants were categorized into three groups according to FPG. 25,26 We found that NAFLD was associated with worse DFS of patients and was an independent prognostic factor across all subgroups (Table S4). Collectively, these clinical data indicated that NAFLD is correlated with tumorigenicity and progression of breast cancer.

### **Fatty livers promote breast cancer**

Next, we investigated whether animal models can recapitulate the impact of NAFLD on human breast cancer. To exclude obesity as a confounding factor, we fed MMTV-PyMT mice, which spontaneously develop breast cancer, a high-fructose diet (HFrD) that induces NAFLD without obvious weight gain.<sup>27,28</sup> Mice fed HFrD exhibited liver steatosis (Figure S1F) with body weights comparable to those of mice fed a control diet (CD) (Figure S1G). Moreover, other confounding factors, including fasting glucose and insulin levels, were also comparable at 8 weeks of age (Figure S1H) when HFrD-fed mice exhibited more initial hyperplastic foci coverage in the mammary gland (Figure 1D). Furthermore, HFrD-fed mice exhibited an earlier onset of the first mammary tumor (Figure 1E). In parallel, lung metastases were markedly increased in mice fed HFrD (Figure 1F). Driving breast cancer progression by non-obese NAFLD was not limited to this experimental setup, as similar data were obtained in HFrD-fed C57BL/6 mice inoculated with syngeneic EO771 breast cancer cells (Figures 1G and 1H).

NAFLD can cause systemic disorders. To investigate whether fatty livers alone can promote breast cancer progression, we transplanted liver grafts from HFrD-fed mice or CD-fed ones into CD-fed recipients inoculated orthotopically with EO771 cells (Figures 1I and S1I).<sup>29</sup> Mice receiving transplanted fatty livers exhibited larger tumors (Figure 1J) but not significantly more lung metastases (Figure S1J) compared with mice receiving normal livers and those without transplantation. Steatosis in livers from HFrD-fed mice gradually subsided when transplanted to CD-fed recipients, which may cause the differences observed in lung metastases (Figure S1K). To circumvent this caveat, we generated conditioned medium (CM) by culturing liver slices in medium for 16 h.<sup>30</sup> Consistent with HFrD-fed mice, EO771 tumor-bearing mice treated with fatty liver CM had larger orthotopic tumors (Figure S1L) and more lung metastases

<sup>(</sup>K) Mice bearing EO771 tumors were intravenously injected with or without conditioned medium (CM) from livers of CD-fed or HFrD-fed mice. Quantification of lung metastasis (n = 6 mice per group).

Statistics were performed using the two-sided log-rank test (B, C, and E), Student's t test (D, F, and H), two-way ANOVA (G and J), or one-way ANOVA (K). \*\*\*\*p < 0.001, \*\*\*\*p < 0.0001. Data are represented as mean  $\pm$  SD.



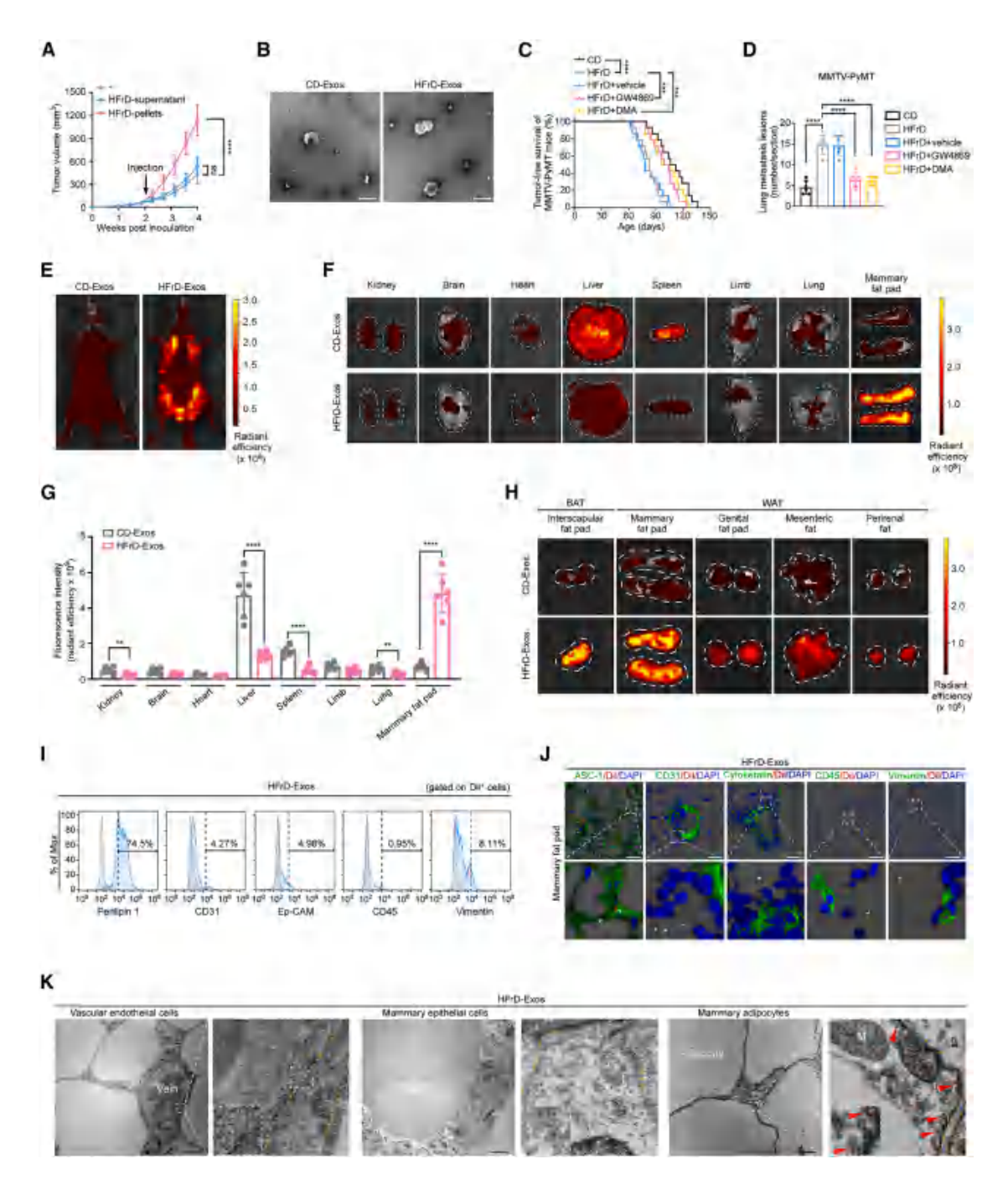


Figure 2. Fatty livers promote breast cancer via mammary adipocyte-tropic exosomes

(A) Supernatants and pellets separated from liver CM of HFrD-fed mice were injected into EO771 tumor-bearing mice intravenously. Tumor growth curves (n = 6 mice per group).

(B) Representative electron microscopy image of the exosome isolated from liver CM of CD-fed or HFrD-fed mice. Scale bar, 200 nm.

(C and D) MMTV-PyMT mice fed HFrD were intraperitoneally administered with vehicle control, GW4869, or DMA. Kinetics of mammary tumor onset (n = 14 mice per group) (C) and quantification of lung metastasis lesions (n = 6 mice per group) (D).

(E–H) Mice were intravenously injected with Dil-labeled exosomes (Exos) isolated from liver CM of CD-fed or HFrD-fed mice (n = 6 mice per group). After 24 h, mice (E) and harvested tissues (F) were monitored by *in vivo* imaging system (IVIS) and quantified (G). (H) Representative images of indicated adipose tissues. BAT, brown adipose tissue; WAT, white adipose tissue.

- (I and J) Mice were administered intravenously with Dil-labeled exosomes isolated from liver CM of HFrD-fed mice.
- (I) Representative flow cytometry histograms for the percentage of indicated cells in the total  $Dil^+$  cells from mammary fat pads (n = 6 mice per group).
- (J) Representative immunofluorescence images of mammary fat pad cryosections. Scale bars, 50 μm.

(legend continued on next page)

# **Article**



(Figure 1K). Collectively, these results suggested that fatty livers promote progression of breast cancer.

# Fatty livers promote breast cancer via mammary adipocyte-tropic exosomes

To explore the fatty liver factor(s) that promote breast cancer, we prepared supernatants containing soluble factors and crude pellets by ultracentrifugation from liver CM<sup>31</sup> (Figure S2A) and intravenously injected different fractions into EO771 tumor-bearing mice. We observed that crude pellets but not supernatants increased tumor size (Figure 2A). The crude pellets contained exosomes and microvesicles. Therefore, we further separated exosomes and microvesicles (Figure S2A)31 and verified them by western blotting (Figure S2B). Exosomes rather than microvesicles significantly promoted tumor growth (Figure S2C). The isolated exosomes were subjected to transmission electron microscopy (TEM) (Figure 2B) and nanoparticle tracking analysis (NTA) (Figure S2D) to confirm their morphology and size distribution, respectively. Exosome preparations were enriched for the exosome markers ALIX and CD81 and devoid of the endoplasmic reticulum marker calnexin (Figure S2E) or lipoprotein (Figures 2B and S2F), confirming their purity. NTA showed that the numbers of exosomes released from fatty livers of HFrD-fed mice were significantly higher than those from normal livers (Figure S2D). The elevated liver-derived exosome numbers were also observed in another mouse NAFLD model induced by a highfat diet (HFD) (Figure S2G). HFrD-fed mice exhibited significantly elevated serum exosome concentrations (Figure S2H). Moreover, we intravenously injected exosomes from HFrD-fed mice into mice in various concentrations, with 30 µg exosomes resulting in serum exosome concentrations the most comparable to HFrD-fed mice (Figure S2H). Furthermore, we administered HFrD-fed MMTV-PyMT mice and HFrD-fed EO771 tumorbearing mice with GW4869 and dimethylamiloride (DMA), two clinically relevant reagents that inhibit the release of exosomes. We found that primary tumor progression (Figures 2C and S2I) and lung metastases (Figures 2D and S2J) were significantly reduced in both models. Taken together, these data suggested that fatty livers drive the development of breast cancer via exosomes.

To visualize the distribution of fatty liver exosomes, we injected 1,1'-dioctadecyl-3,3,3',3'-tetramethylindocarbocyanine perchlorate (Dil)-labeled exosomes isolated from liver CM into C57BL/6 mice intravenously and quantified exosome biodistribution in different organs by *in vivo* imaging system (IVIS). Exosomes derived from livers of HFrD (Figures 2E-2G) and HFD-fed mice (Figure S2K) but not exosomes derived from livers of CD-fed mice predominantly accumulated in mammary fat pads. To investigate the uptake of fatty liver exosomes across different adipose tissues, we harvested several white adipose tissues (WATs) and interscapular fat pads as main brown adipose tissues (BATs). Although the signals were highly abundant in BATs (Figures 2H and S2L), BATs constitute only a minor

amount of adipose tissue in adult humans, and the physiological relevance of human BATs remains a topic of debate. <sup>32,33</sup> Therefore, we focused on WATs due to the clinical relevance. Among all WATs, the signals of fatty liver exosomes were highest in mammary fat pads (Figures 2H and S2L). By comparison, tumor-derived exosomes did not show significant enrichment in mammary fat pads (Figure S2M).

We further visualized the cellular distribution of fatty liver exosomes in mammary fat pads and found that they were predominantly taken up by perilipin 1<sup>+</sup> or ASC-1<sup>+</sup> adipocytes but not by Ep-CAM<sup>+</sup> or cytokeratin<sup>+</sup> epithelial cells, CD31<sup>+</sup> vascular endothelial cells, CD45+ immune cells, or vimentin+ fibroblasts (Figures 2I, 2J, and S2N-S2P). Because tumor cells can uptake exosomes,<sup>34</sup> we injected Dil-labeled fatty liver exosomes into EO771 tumor-bearing mice. In contrast to adipocytes, tumor cells showed little exosome uptake (Figure S2Q). We injected FM1-43FX dye-labeled fatty liver exosomes into C57BL/6 mice, and electron microscopy also showed these exosomes primarily in adipocytes (Figure 2K). Given the mammary adipocyte tropism of fatty liver exosomes, EO771 cells were injected subcutaneously into the dorsolateral flank of mice, which is poor of adipose tissues, and performed liver transplantation 2 weeks after injection. In contrast with mammary fat pad injection, transplantation of fatty livers did not significantly increase tumor growth (Figure S2R). Collectively, these data suggested that fatty livers secrete exosomes that preferentially migrate to mammary adipocytes and subsequently drive breast cancer progression.

# An ErbB4-Nrg4 axis determines the mammary adipocyte enrichment of fatty liver exosomes

EVs present cell-type-specific proteins reflecting cellular origin. 35,36 We performed a proteomic analysis of exosomes using liquid chromatography-tandem mass spectrometry (LC-MS/MS) (Figure 3A; Table S5). Albumin as the hepatocyte marker was very abundant in liver exosomes (Figure S3A), whereas lipoprotein in exosomes was barely detected (Table S5). We isolated primary hepatocytes<sup>37</sup> and other four major cell types<sup>38–41</sup> from fatty livers and separated exosomes from their CM. Injection of exosomes derived from hepatocytes, but not equal amounts of exosomes from other cell types, led to accumulation of exosomes in mammary fat pads (Figure S3B), suggesting that mammary adipose-tropic fatty liver exosomes are mainly secreted by hepatocytes.

Specific targeting to recipient cells is mediated by exosome membrane proteins. <sup>19,34,42</sup> To identify the membrane protein(s) dictating mammary adipose tropism, the top five upregulated membrane proteins in fatty liver exosomes (Figure S3C; Table S5) were knocked out in murine hepatocyte AML12 cells (Figure S3D). To recapitulate lipid overload in hepatocytes *in vitro*, we treated AML12 cells with palmitic acid (PA). <sup>43,44</sup> We intravenously injected Dil-labeled exosomes isolated from CM of PA-treated AML12 cells into mice. Consistently, exosomes

(K) Mice were injected with FM1-43FX-labeled exosomes isolated from liver CM of HFrD-fed mice. Mammary fat pads were harvested and imaged by TEM. Red arrows indicate the exosomes. Yellow dashed lines, cell borders. M, mitochondria. Scale bars, 5 µm.

Statistics were performed using two-way ANOVA (A), two-sided log-rank test (C), one-way ANOVA (D), or Student's t test (G). Ns, not significant; \*\*p < 0.01, \*\*\*p < 0.001, \*\*\*\*p < 0.001. Data are represented as mean  $\pm$  SD.



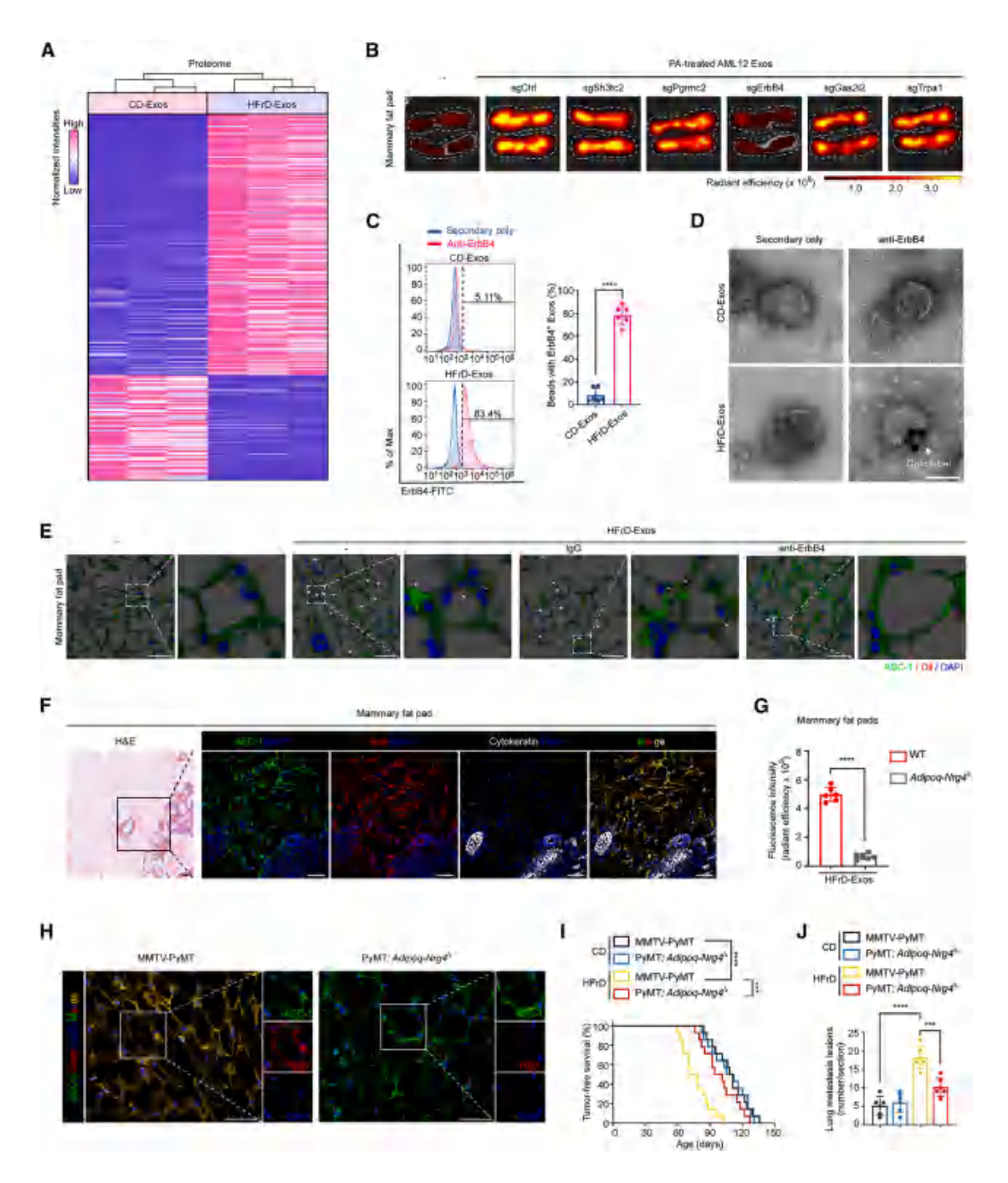


Figure 3. An ErbB4-Nrg4 axis determines mammary adipocyte enrichment of fatty liver exosomes

(A) Proteomic analysis of liver exosomes (Exos) from CD-fed and HFrD-fed mice (n = 3 independent experiments). Samples were pooled from 2 mice per group for each experiment. Heatmap representing proteins with statistically significant differences.

- (B) Exosomes separated from palmitic acid (PA)-treated AML12 cells with indicated protein knockout were labeled with Dil and intravenously injected into mice. Representative IVIS images of mammary fat pads.
- (C) Representative histograms (left) and quantification (right) of the percentage of  $ErbB4^+$  exosomes in exosomes isolated from livers of mice fed either CD or HFrD (n = 6 independent experiments). Samples were pooled from 2 mice per group for each experiment.
- (D) Representative micrographs of IG-TEM of exosomes isolated from livers of mice fed either CD or HFrD. The white arrow indicates the gold label. Scale bar, 100 nm.
- (E) Mice were injected with Dil-labeled fatty liver exosomes pretreated with or without anti-ErbB4 antibody or control immunoglobulin G (IgG). Representative immunofluorescence images of mammary fat pad cryosections. Scale bars, 50 µm.
- (F) Representative H&E-stained (left) and immunofluorescence images (right) of normal mammary fat pads. Scale bars, 50 µm.
- (G) Dil-labeled fatty liver exosomes were injected into wild-type (WT) mice or  $Adipoq-Nrg4^{\Delta}$  mice. Quantification of Dil fluorescence intensity of mammary fat pads by IVIS (n = 6 mice per group).

# **Article**



from PA-treated AML12 cells preferentially accumulated in mammary fat pads (Figure S3E). More importantly, the knockout of receptor tyrosine-protein kinase erbB4 (*ErbB4*) rather than other membrane proteins abolished this effect (Figures 3B and S3F). Next, we performed flow cytometry (Figure S3G) and found that the proportions of ErbB4<sup>+</sup> exosomes in liver exosomes from HFrD- and HFD-fed mice were much higher than those in normal liver exosomes (Figures 3C and S3H), which was corroborated by enzyme-linked immunosorbent assay (ELISA) and immunoblotting (Figures S3I–S3L). Similarly, ErbB4 levels on exosomes derived from PA-treated AML12 cells were significantly higher (Figures S3M and S3N). Immunogold-TEM (IG-TEM) revealed stronger ErbB4 signals in fatty liver exosomes compared with ErbB4 signals in normal liver exosomes (Figure 3D).

To examine the role of exosomal ErbB4 *in vivo*, fatty liver exosomes were pre-incubated with a neutralizing antibody against ErbB4, which abrogated the co-localization of fatty liver exosomes and mammary adipocytes (Figures 3E and S3O). Additionally, ErbB4 neutralization reversed the effects of intravenous injection of fatty liver exosomes on promoting tumor growth (Figure S3P) and metastases (Figure S3Q). Moreover, ErbB4 neutralization reversed the effects of exosomes from primary hepatocytes of fatty livers on promoting tumor growth (Figure S3R). Taken together, these data suggested that ErbB4 overexpressed in fatty liver exosomes mediates the exosome enrichment in mammary adipocytes.

ErbB4 binds to neuregulins (Nrgs) Nrg1, Nrg2, Nrg3, and Nrg4.45,46 We analyzed the expression profile of Nrgs across multiple organs using online microdata and found that Nrg4 was mainly expressed in fat pads, especially mammary ones (Figure S4A). By comparison, Nrg1-3 were predominantly expressed in the central nervous system (Figure S4B), which was validated by western blotting (Figure S4C). Furthermore, Nrg4 rather than Nrg1-3 was also expressed in other WATs, albeit their levels were lower than those in mammary fat pads (Figure S4D), Although BATs also had considerable Nrg4 expression (Figure S4D), the relevance of WATs as an Nrg4 source is more pronounced in humans, as BATs are scarce in adult humans.<sup>45</sup> Given the incapacity of exosomes to cross the bloodbrain barrier<sup>47</sup> and the mammary adipocyte tropism of fatty liver exosomes, we decided to focus on Nrg4. Nrg4 was mainly expressed by ASC-1+ adipocytes in mammary fat pads (Figure 3F). To specifically investigate the function of Nrg4 in adipocytes, we developed homozygous Adipoq-Nrg4<sup>△</sup> mice (Figures S4E and S4F). Adipocyte-conditional Nrg4 knockout abolished the accumulation of injected fatty liver exosomes in mammary fat pads (Figure 3G). Adipog-Nrg4<sup>\Delta</sup> mice inoculated with EO771 cells exhibited slower tumor growth (Figure S4G) and fewer metastases (Figure S4H) compared with wild-type littermates when they were injected with fatty liver exosomes. Moreover, we employed adipocyte Nrg4-deficient tumorigenic mice (PyMT; Adipoq-Nrg4<sup>\Delta</sup> mice) (Figures 3H and S4I). Adipocyte-specific deletion of Nrg4 significantly improved tumor-free survival (Figure 3I) and reduced metastases (Figure 3J) in HFrD-fed mice but not in CD-fed mice. Collectively, these data suggested that ErbB4 enriched in fatty liver exosomes binds to Nrg4 mainly expressed in mammary adipocytes and consequently mediates the preferential uptake of fatty liver exosomes by mammary adipocytes.

# Fatty liver exosomes promote breast cancer progression by inducing FFA release from adipocytes

Adipocytes can accelerate cancer progression by providing energy-dense lipids, such as FFAs. 8,11,12 Therefore, we performed 4,4-difluoro-1,3,5,7,8-pentamethyl-4-bora-3a,4a-diaza-s-indacene (BODIPY) staining and observed that the injection of fatty liver exosomes increased lipid accumulation in both abnormal ducts and tumor cells in mammary fat pads of MMTV-PyMT mice (Figure 4A). Consistently, abnormal ducts and tumor cells harvested from HFrD-fed mice exhibited significantly elevated lipid concentrations compared with those from CD-fed mice (Figures S5A and S5B), which was abrogated by ErbB4 neutralization (Figure S5A) or adipocyte-specific deletion of Nrg4 (Figure S5B). Similar results were observed in tumor cells in both EO771 tumor-bearing mice injected with fatty liver exosomes (Figure 4B) and those fed HFrD (Figures S5C and S5D).

FFAs released during lipolysis are the primary form of lipid transfer from adipose tissues to tumor cells. <sup>11,48</sup> We found that fatty liver exosome treatment induced FFA secretion by adipocytes from WATs, among which mammary adipocytes released the highest levels of FFAs (Figure 4C). Moreover, we observed a slight increase in serum FFAs in mice with exosome injection (Figure S5E). To investigate whether this slight serum FFA elevation may promote metastatic capacity of circulating tumor cells, we intravenously injected EO771 cells into mice and observed no appreciable effect of fatty liver exosomes on lung metastases (Figure S5F). Since fatty liver exosomes increased FFA release in mesenteric adipocytes, we employed Apc-L850X mice, which spontaneously develop colorectal cancer, <sup>49</sup> and found similar tumor numbers and volumes in mice injected with or without fatty liver exosomes (Figure S5G).

Fatty liver exosome injection dramatically increased the release of FFAs in mammary adipocytes separated from MMTV-PyMT mice (Figure 4D). Anti-ErbB4 antibody treatment (Figures S5H and S5I) and the conditional knockout of *Nrg4* in adipocytes (Figures S5J and S5K) dramatically reversed the increased FFA release of mammary adipocytes in HFrD-fed mice. Of note, fatty liver exosome treatment had no appreciable effect on fasting glucose or insulin levels (Figures S5L and S5M).

To verify the role of fatty liver exosomes in mediating lipid transport from adipocytes to breast cancer cells, primary adipocytes were isolated and labeled with BODIPY. A significant increase in fluorescent lipids in EO771 cells co-cultured with mammary adipocytes isolated from mice injected with fatty liver

See also Figures S3 and S4 and Table S5.

<sup>(</sup>H) Representative immunofluorescence staining for ASC-1 and Nrg4 in mammary fat pads from indicated mice. Scale bars, 50 μm. (I and J) Indicated mice were fed either a CD or HFrD. Kinetics of mammary tumor onset (*n* = 14 mice per group) (I) and quantification of lung metastasis (*n* = 6 mice per group) (J).

Statistics were performed using Student's t test (C and G), the two-sided log-rank test (I), or one-way ANOVA (J). \*\*\*p < 0.001, \*\*\*\*p < 0.0001. Data are represented as mean  $\pm$  SD.



# **Cell Metabolism Article**

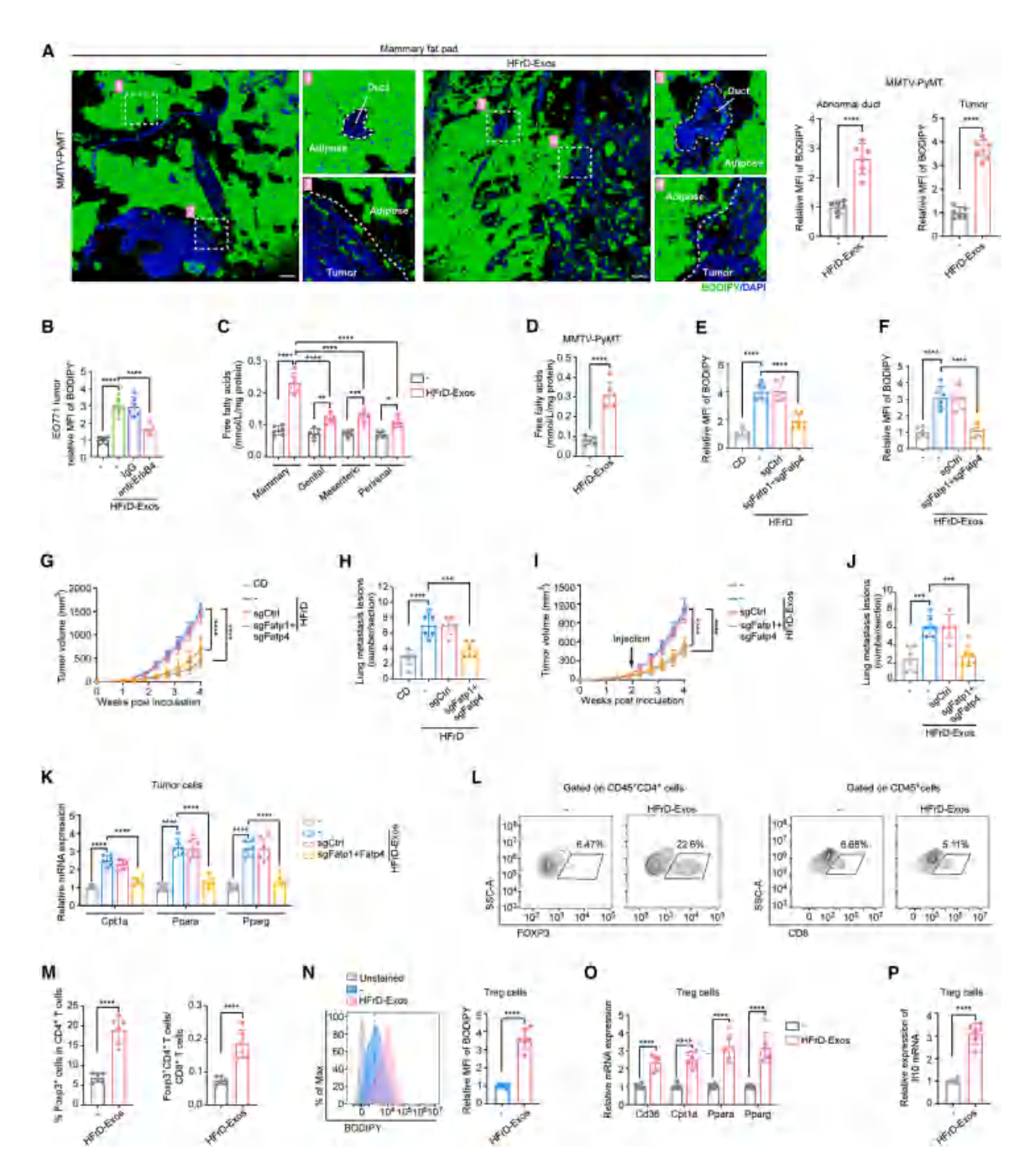


Figure 4. Fatty liver exosomes promote breast cancer progression by inducing FFA release from adipocytes

(A) MMTV-PyMT mice were administered intravenously without or with fatty liver exosomes. Representative images (left) and quantification of BODIPY (right) in indicated cells of mammary fat pads (n = 6 mice per group). MFI, mean fluorescence intensity. Scale bars, 100  $\mu$ m.

(B) EO771 tumor-bearing mice injected with or without fatty liver exosomes were administered with anti-ErbB4 antibody or IgG. Quantification of BODIPY intensity in tumor cells (n = 6 mice per group).

(C and D) After being injected with or without fatty liver exosomes, adipocytes were isolated from indicated adipose tissues from C57BL/6 mice (C) and mammary adipose tissue of MMTV-PyMT mice (D). Quantification of FFA levels in adipocytes (n = 6 mice per group).

(legend continued on next page)

# **Article**



exosomes (Figure S5N). However, this effect was abrogated by Nrg4 knockout in adipocytes (Figure S5N). Membrane proteins that mediate cellular lipid trafficking include fatty acid transport proteins (FATPs) and CD36.50,51 We found that Fatp4 and Fatp1 were mainly expressed in tumor cells from MMTV-PyMT mice (Figure S50) and EO771 cells (Figures S5P and S5Q), while other Fatps and Cd36 were barely expressed. To address the functional role of Fatp4 and Fatp1, we co-cultured Fatp4- and Fatp1-deficient EO771 cells with BODIPY-labeled 3T3-L1 adipocytes, which were pretreated with normal liver exosomes or fatty ones (Figures S5R-S5V). We observed significantly increased levels of fluorescent lipids in EO771 cells co-cultured with 3T3-L1 adipocytes pretreated with fatty liver exosomes compared with those co-cultured with 3T3-L1 adipocytes pretreated with normal liver exosomes (Figure S5V). More importantly, the simultaneous knockout of Fatp1 and Fatp4 in EO771 cells abolished this effect (Figure S5V). Consistently, lipid uptake by tumor cells was significantly elevated in EO771 tumor-bearing mice fed HFrD (Figure 4E) or injected with fatty liver exosomes (Figure 4F), which was abrogated by knockout of Fatp1 and Fatp4 in EO771 cells. FATP1 and FATP4 ablation reduced tumor growth and metastases in EO771 tumor-bearing mice fed HFrD (Figures 4G and 4H) and those injected with fatty liver exosomes (Figures 4I and 4J).

FFAs can support tumor progression by upregulating lipid metabolism of tumor cells. 11 We found that tumor cells from mice receiving fatty liver exosomes expressed significantly higher levels of FFA metabolism-related genes, including carnitine palmitoyltransferase 1A (CPT1A), peroxisome proliferatoractivated receptor alpha (PPARα), and PPARγ (Figure 4K).<sup>52</sup> FATP1 and FATP4 ablation in EO771 cells abrogated this effect (Figure 4K). Tumor-infiltrating regulatory T (Treg) cells can take up FFAs, which enhance their lipid metabolism and suppressive function.<sup>52</sup> We found that the frequencies of Treg cells in total CD4<sup>+</sup> T cells and the ratio of Treg cells: CD8<sup>+</sup> T cells were significantly increased in tumors from mice injected with fatty liver exosomes (Figures 4L, 4M, and S5W). Additionally, Treg cells from mice receiving fatty liver exosomes had significantly elevated lipid content (Figure 4N), expression of FFA metabolism-related genes (Figure 40), and interleukin (IL)-10 expression (Figure 4P). Taken together, these data suggested that fatty liver exosomes promote tumor progression by triggering mammary adipocytes to release FFAs, which are then taken up by tumor cells and Treg cells.

# Fatty liver exosomes increase mammary adipocyte lipolysis via TRMT10C

Given the ability of fatty liver exosomes to enhance FFA release, we conducted a comprehensive lipidomic analysis and observed a comparable total lipid abundance and similar lipid class distributions between normal liver exosomes and fatty ones (Figures 5A and 5B). Exosomes mediate the functions of recipient cells via containing cargoes. <sup>20,53,54</sup> To investigate which exosome content is responsible for the enhanced lipolysis in adipocytes, we reviewed the proteomic data. The top five enriched proteins identified by comparative proteomic analysis (Figure 5C; Table S5) were knocked out in AML12 cells (Figure S6A). 3T3-L1 adipocytes pretreated with exosomes separated from PA-treated AML12 cells significantly increased FFA release, while depletion of mitochondrial tRNA methyltransferase 10 homolog C (Trmt10c) in AML12 cells rather than other upregulated proteins reversed this effect (Figure S6B). 3T3-L1 adipocytes treated with exosomes from AML12 cells with TRMT10C overexpression (Figure S6C) exhibited significantly increased FFA release (Figure S6D). TRMT10C was highly enriched in exosomes from liver CM and primary hepatocyte CM of HFrD- and HFD-fed mice (Figures S6E-S6H). TRMT10C is the catalytic component of the mitochondrial methyltransferase. 55 TRMT10C colocalized with Tom20, a marker of mitochondria (Figure 5D). Co-localization analysis revealed a high Pearson's correlation coefficient between TRMT10C and Tom20 in both adipocytes from mice administered with and without fatty liver exosomes (Figure S6I). Moreover, the level of TRMT10C was significantly higher in adipocytes of mice injected with fatty liver exosomes (Figure 5E), with a specific distribution in mitochondrial but not cytosolic fractions (Figure S6J). Adipocytes isolated from mice injected with fatty liver exosomes exhibited comparable Trmt10c mRNA levels (Figure S6K) compared with those isolated from untreated mice. Western blot demonstrated a significant decrease in TRMT10C expression in Trmt10cknockout AML12 cells (Figure S6L) and their exosomes (Figure S6M). Protein contents remain unaltered in Trmt10c knockout AML12 cell-derived exosomes (Figure S6N). EO771 cells exhibited increased fluorescent lipids when co-cultured with 3T3-L1 adipocytes pretreated with exosomes from PAtreated AML12 CM, compared with those with exosomes from control AML12 cells (Figure S6O). Importantly, knockout of Trmt10c, which had no significant effect on lipid contents of exosomes from PA-treated AML12 cells themselves (Figure S6P), abrogated this effect (Figure S6O).

(E–K) EO771 cells with or without Fatp1 and Fatp4 knockout were inoculated into mice fed either CD or HFrD (E, G, and H) or injected with or without fatty liver exosomes (F and I–K) (n = 6 mice per group).

(E and F) Quantification of BODIPY intensity in tumor cells.

(G and I) Tumor growth curves.

(H and J) Quantification of lung metastasis.

(K) Expression of fatty acid metabolism-related genes in tumor cells.

(L-P) EO771 tumor-bearing mice were intravenously injected without or with fatty liver exosomes, and tumor-infiltrating leukocytes were isolated.

(L and M) Representative plots (L) and quantification (M) of the percentages of regulatory T (Treg) cells in total CD4<sup>+</sup> T cells and the ratio of Treg cells to CD8<sup>+</sup> T cells (n = 6 independent experiments). Samples were pooled from 2 mice per group for each experiment.

(N-P) Treg cells were isolated by flow sorting (n = 6 independent experiments). Samples were pooled from 2 mice per group for each experiment.

(N) Representative histograms (left) and quantification of BODIPY intensity (right).

(O and P) The expression of fatty acid metabolism-related genes (O) and II10 (P).

Statistics were performed using Student's t test (A, D, and M–P), one-way ANOVA (B, E, F, H, J, and K), or two-way ANOVA (C, G, and I). \*p < 0.05, \*\*p < 0.01, \*\*\*p < 0.001, \*\*\*\*p < 0.001. Data are represented as mean  $\pm$  SD.

See also Figure S5.

# **CellPress**

# **Cell Metabolism Article**

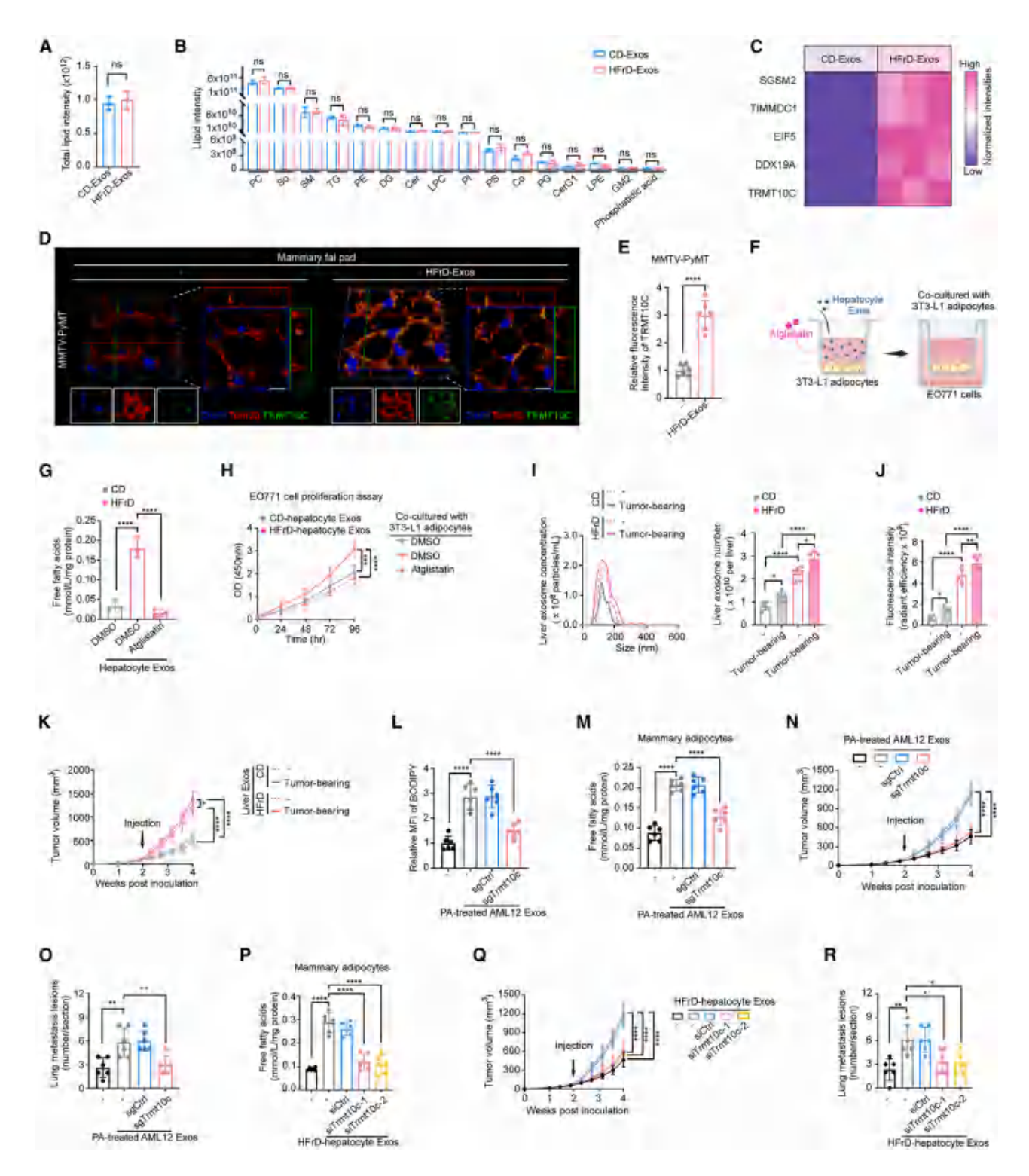


Figure 5. Fatty liver exosomes increase mammary adipocyte lipolysis via TRMT10C

(A and B) Lipidomic analysis of exosomes derived from liver CM of mice fed either CD or HFrD (n = 3 independent experiments). Samples were pooled from 2 mice per group for each experiment. PC, phosphatidylcholine; So, sphingosine; SM, sphingomyelin; TG, triglyceride; PE, phosphatidylethanolamine; DG, diglyceride; Cer, ceramide; LPC, lyso-phosphatidylcholine; PI, phosphatidylinositol; PS, phosphatidylserine; Co, coenzyme; PG, phosphatidylglycerol; CerG1, monoglycosylceramide; LPE, lyso-phosphatidylethanolamine; GM2, gangliosides 2.

- (A) Comparison of the total lipid content.
- (B) The intensities of all detected lipid classes.
- (C) Top five significantly enriched proteins in fatty liver exosomes evaluated by mass spectrometry.

# **Article**



To determine whether fatty liver-derived factors directly requlate tumor growth, we exposed EO771 cells to CM from hepatocytes of mice fed either a CD or HFrD. Colorimetric assay revealed no significant impact on EO771 cell proliferation (Figure S6Q). By comparison, when we pretreated 3T3-L1 adipocytes with exosomes from primary hepatocyte CM and co-cultured these 3T3-L1 adipocytes with EO771 cells (Figure 5F), we observed that both FFA release by adipocytes and tumor cell proliferation were significantly increased by exosomes from hepatocytes of HFrD-fed mice (Figures 5G and 5H). To investigate whether adipocyte-derived FFAs drive this proliferative effect, we treated 3T3-L1 adipocytes with hepatocyte-derived exosomes in the presence of atglistatin, a selective inhibitor of adipose triglyceride lipase (ATGL), before co-culture. Both FFA release by adipocytes and tumor cell proliferation were effectively blocked by atglistatin (Figures 5G and 5H). Collectively, these data suggested that FFAs released from adipocytes in response to fatty liver exosomes, rather than other factors secreted by fatty livers, promote breast cancer progression.

Extrahepatic tumor-derived EVs and particles (EVPs) support fatty liver formation.<sup>20</sup> We observed significantly increased levels of hepatic lipid droplet accumulation in tumor-bearing mice fed either CD or HFrD compared with tumor-free controls (Figure S6R). Moreover, the numbers of liver exosomes and exosomal levels of ErbB4 and TRMT10C were significantly higher in mice bearing EO771 tumors compared with tumor-free littermates, regardless of their diet (Figures 5I and S6S-S6U). Furthermore, we injected Dil-labeled liver exosomes into CDfed mice. Signals of liver exosomes from tumor-bearing mice accumulating in mammary fat pads were significantly increased compared with those from mice without tumors in both the CDfed and HFrD-fed conditions (Figure 5J). To investigate the effects of these exosomes on tumor growth, we intravenously injected exosomes into CD-fed EO771 tumor-bearing mice. Liver exosomes from HFrD-fed donors markedly enhanced tumor growth compared with those from CD-fed donors (Figure 5K). Furthermore, liver exosomes derived from HFrD-fed tumorbearing mice had a significantly stronger effect on promoting tumor progression compared with those from HFrD-fed tumor-free counterparts (Figure 5K). Liver exosomes from CD-fed tumorbearing mice exhibited a tendency to enhance tumor growth. Nevertheless, this difference did not reach statistical significance (Figure 5K). Collectively, these data, together with the previous study, <sup>20</sup> suggest that fatty livers and breast cancer form a vicious cycle via EVs.

Consistent with the results of in vitro experiments, tumor cells harvested from EO771 tumor-bearing mice treated with PAtreated AML12 cell-derived exosomes exhibited significantly elevated lipid concentration, which was abolished by Trmt10c knockout in AML12 cells (Figure 5L). Moreover, mice injected with PA-treated AML12 cell-derived exosomes dramatically increased the release of FFAs in mammary adipocytes, which was dramatically reversed by Trmt10c deletion (Figure 5M). In addition, mice injected with PA-treated AML12 cell-derived exosomes accelerated tumor growth (Figure 5N) and metastases (Figure 50), which were also abrogated by Trmt10c knockout. Similar results were obtained using the model of primary hepatocytes from HFrD-fed mice (Figures 5P-5R and S6V). Collectively, these data suggested that fatty liver exosomes promote breast cancer progression by increasing lipolysis in adipocytes via exosomal TRMT10C.

# Exosomal TRMT10C mediates FFA release in adipocytes via m<sup>1</sup>A in mitochondrial mRNAs

TRMT10C mediates the N¹-methylation of guanine (m¹G) and adenosine (m¹A) of mRNAs and tRNAs in mitochondria. 55-57 Ultra-performance LC-MS/MS (UPLC-MS/MS) showed that the levels of m¹A but not m¹G in mitochondrial mRNAs of adipocytes separated from mice injected with PA-treated AML12 cell-derived exosomes were upregulated, which was rescued

(D and E) Representative immunofluorescence images (D) and quantification (E) of TRMT10C in mammary fat pads of mice with indicated treatment (n = 6 mice per group). Scale bars, 10  $\mu$ m.

(F–H) 3T3-L1 adipocytes were treated with exosomes isolated from livers of CD-fed or HFrD-fed mice in the presence of atglistatin or vehicle DMSO and co-cultured with EO771 cells (n = 3 independent experiments).

- (F) Schematics.
- (G) Quantification of FFA levels in 3T3-L1 adipocytes.
- (H) The proliferation rates of EO771 cells.
- (I–K) Mice fed either CD or HFrD were inoculated with or without EO771 cells. Exosomes were isolated from liver CM of indicated mice (n = 6 mice per group).
- (I) Representative nanoparticle tracking analysis (NTA) profiles (left) and quantification of particle numbers of indicated exosomes (right).
- (J) Liver exosomes were labeled with Dil and injected into mice. Quantification of the Dil intensity in mammary fat pads by IVIS.
- (K) Tumor growth curves of CD-fed EO771 tumor-bearing mice injected with indicated exosomes.
- (L–O) Following transduction without or with control (sgCtrl) or *Trmt10c* sgRNA (sgTrmt10c), AML12 cells were treated with PA. Exosomes isolated from these cells were injected into mice with (L, N, and O) or without (M) inoculation with EO771 cells (n = 6 mice per group).
- (L) Quantification of BODIPY intensity in tumor cells.
- (M) Quantification of FFA levels in mammary adipocytes.
- (N) Tumor growth curves.
- (O) Quantification of lung metastasis.
- (P–R) Primary hepatocytes isolated from HFrD-fed mice were transfected with the indicated small interfering RNA (siRNA) and injected into mice without (P) or with (Q and R) EO771 cell inoculation (n = 6 mice per group).
- (P) Quantification of FFA levels in mammary adipocytes.
- (Q) Tumor growth curves.
- (R) Quantification of lung metastasis.

Statistics were performed using Student's t test (A, B, and E), one-way ANOVA (G, I, J, L, M, O, P, and R), or two-way ANOVA (H, K, N, and Q). Ns, not significant;  $^*p < 0.05$ ,  $^{**}p < 0.01$ ,  $^{***}p < 0.001$ ,  $^{****}p < 0.0001$ . Data are represented as mean  $\pm$  SD. See also Figure S6.

# **CellPress**

# **Cell Metabolism Article**

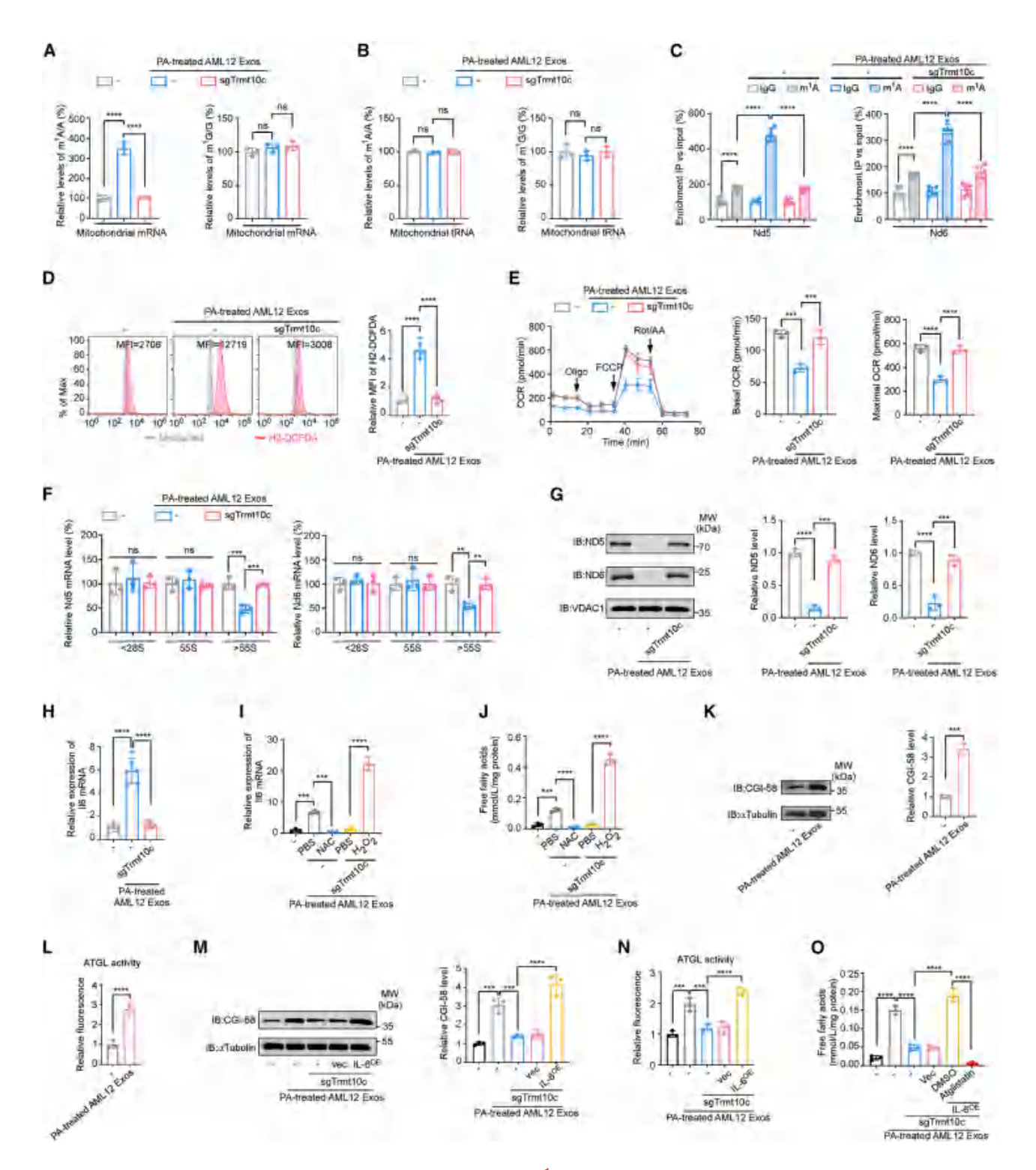


Figure 6. Exosomal TRMT10C mediates FFA release in adipocytes via m<sup>1</sup>A in mitochondrial mRNAs

(A-D) AML12 cells without or with Trmt10c knockout were treated with PA, and exosomes were obtained and administered to mice.

(A-C) The mitochondrial RNAs were extracted from isolated adipocytes.

(A and B) Quantification of the m<sup>1</sup>A/A ratio (left) and m<sup>1</sup>G/G ratio (right) in mitochondrial mRNAs (A) and tRNAs (B) by ultra-performance liquid chromatography-tandem mass spectrometry (UPLC-MS/MS) (*n* = 3 independent experiments). Samples were pooled from 10 mice per group for each experiment. (C) m<sup>1</sup>A-RIP-qPCR analysis of mitochondrial Nd5 (left) and Nd6 (right) mRNAs in adipocytes (*n* = 6 independent experiments). Samples were pooled from 10 mice per group for each experiment.

# **Article**



by Trmt10c knockout in AML12 cells (Figure 6A). By comparison, no changes were observed in the levels of m<sup>1</sup>A or m<sup>1</sup>G in mitochondrial tRNAs (Figure 6B). An m<sup>1</sup>A RNA immunoprecipitation-qPCR (m<sup>1</sup>A-RIP-qPCR) assay demonstrated a significantly increased m<sup>1</sup>A antibody enrichment of Nd5 and Nd6 mRNAs in adipocytes isolated from mice treated with PA-treated AML12 exosomes (Figure 6C), whereas no such effect was observed in other mitochondrial mRNAs (Figure S7A). To determine whether TRMT10C mediates m<sup>1</sup>A methylation of mitochondrial Nd5 and Nd6 mRNAs, we knocked out and overexpressed TRMT10C in 3T3-L1 adipocytes, respectively (Figure S7B). We observed that Trmt10c knockout led to abrogation of methylation at mitochondrial Nd5 and Nd6 mRNAs, whereas TRMT10C overexpression resulted in a marked increase in methylation levels (Figure S7C). It has been reported that downregulation of ND5 and ND6 proteins, which are subunits of mitochondrial complex I,58 increases mitochondrial reactive oxygen species (ROS).59 We observed that mice injected with PAtreated AML12 cell-derived exosomes had increased levels of ROS in mammary adipocytes, which were abrogated by Trmt10c knockout in AML12 cells (Figure 6D). Consistently, oxygen consumption rate was significantly reduced in 3T3-L1 adipocytes treated with exosomes derived from PA-treated AML12 cells, which was rescued by Trmt10c knockout in AML12 cells (Figure 6E). To investigate whether exosomal TRMT10C increases mitochondrial ROS via ND5 and ND6, nuclear-formatted Nd5 and Nd6 genes incorporating a mitochondrial targeting sequence were overexpressed in 3T3-L1 adipocytes (Figures S7D-S7F). Increased mitochondrial ROS induced by exosomal TRMT10C was abrogated by the simultaneous overexpression of ND5 and ND6 (Figure S7G). These data suggested that exosomal TRMT10C increases mitochondrial ROS by catalyzing m<sup>1</sup>A modification of Nd5 and Nd6 mRNAs in adipocytes.

The m<sup>1</sup>A modification within the coding sequence regions of mRNAs influences mRNA stability and inhibits translation.<sup>57,60,61</sup> Therefore, we evaluated whether exosomal TRMT10C regulates the mRNA levels of Nd5 and Nd6. We observed comparable levels

of Nd5 and Nd6 mRNAs in 3T3-L1 adipocytes treated with or without PA-treated AML12 cell-derived exosomes (Figure S7H). To investigate RNA translation efficiency, we performed mitochondrial ribosome profiling. 62 Mitochondrial non-translating fraction (<28S), translation initiation fraction (<55S, including 28S and 39S ribosomes and 55S monosomes), and translation-active polysomes (>55S) were isolated (Figures S7I and S7J). Polysome profiling in 3T3-L1 adipocytes displayed that PA-treated AML12 cell-derived exosomes resulted in reduced Nd5 and Nd6 mRNA abundance in translation-active polysome portions, which generally have high translation efficiency (Figure 6F). 57,60 This phenomenon was abrogated by Trmt10c knockout in AML12 cells (Figure 6F), suggesting that exosomal TRMT10C suppresses the translation of Nd5 and Nd6 mRNAs. Overexpression of TRMT10C significantly decreased ND5 and ND6 protein levels in 3T3-L1 adipocytes (Figure S7K). Consistently, mammary adipocytes in mice injected with PA-treated AML12 exosomes exhibited decreased protein levels of ND5 and ND6, which were reversed by Trmt10c knockout in AML12 cells (Figure 6G). These data suggested that exosomal TRMT10C inhibits the translation of ND5 and ND6 by inducing m<sup>1</sup>A modification and consequently increases mitochondrial ROS.

Mitochondrial ROS can increase the production of IL-6, <sup>63–65</sup> which promotes lipolysis in adipocytes. <sup>64,66</sup> Because elevated FFA release in adipocytes can be triggered by exosomal TRMT10C, which promotes ROS production, we asked whether TRMT10C increases IL-6 production. We found that adipocytes from mice injected with exosomes from PA-treated AML12 cells exhibited a significant upregulation of IL-6 mRNA expression, which was abrogated by *Trmt10c* knockout in AML12 cells (Figure 6H).

Next, we investigated whether exosomal TRMT10C promotes IL-6 production by increasing mitochondrial ROS. PA-treated AML12 exosomes significantly increased IL-6 expression in 3T3-L1 adipocytes, which was attenuated by antioxidant *N*-acetyl-L-cysteine (NAC) treatment (Figure 6I). By contrast, exosomes isolated from PA-treated AML12 cells with *Trmt10c* 

See also Figure S7.

<sup>(</sup>D) Mammary adipocytes were stained with 2', 7'-dichlorodihydrofluorescein diacetate (H2-DCFDA) for ROS detection. Representative histograms (left) and quantification (right) (n = 6 mice per group).

<sup>(</sup>E) AML12 cells transduced with sgCtrl or sgTrmt10c were treated with PA. Oxygen consumption rate (OCR) of 3T3-L1 adipocytes exposed to exosomes separated from indicated AML12 cells was measured (*n* = 3 independent experiments). Representative oxygen consumption curves (left) and quantification of basal OCR (middle) and maximal OCR (right). Oligo, oligomycin; FCCP, fluorocarbonyl cyanide phenylhydrazone; Rot/AA, rotenone and antimycin A.

<sup>(</sup>F) AML12 cells without or with *Trmt10c* knockout were treated with PA. 3T3-L1 adipocytes were pretreated with exosomes from indicated AML12 cells. Nd5 (left) and Nd6 (right) mRNA levels in <28S, 55S, and >55S ribosomes in 3T3-L1 adipocytes (n = 3 independent experiments). Samples were pooled from 2 mice per group for each experiment.

<sup>(</sup>G) Representative immunoblots and quantification of ND5 and ND6 in mammary adipocytes of mice injected with exosomes isolated from indicated AML12 cells (n = 3) independent experiments).

<sup>(</sup>H) II6 mRNA levels in mammary adipocytes of mice injected with exosomes from indicated AML12 cells (n = 6 mice per group).

<sup>(</sup>I and J) 3T3-L1 adipocytes were treated with exosomes from indicated AML12 cells in the presence of  $H_2O_2$  or NAC. II6 mRNA (I) and FFA levels (J) were measured (n = 3 independent experiments).

<sup>(</sup>K and L) Primary mammary adipocytes were isolated from mice injected with PA-treated AML12 cell-derived exosomes.

<sup>(</sup>K) Representative immunoblots (left) and quantification (right) of CGI-58 (n = 3 independent experiments).

<sup>(</sup>L) Adipose triglyceride lipase (ATGL) activity measured by fluorescence-based lipase activity assay (n = 3 independent experiments).

<sup>(</sup>M-O) 3T3-L1 adipocytes transduced with indicated lentiviruses were treated with exosomes from PA-treated AML12 cells.

<sup>(</sup>M) Representative immunoblots (left) and quantification (right) of CGI-58 (n = 3 independent experiments).

<sup>(</sup>N) ATGL activity (n = 3 independent experiments).

<sup>(</sup>O) 3T3-L1 adipocytes were treated with atglistatin or DMSO, and FFA levels were quantified (n = 3 independent experiments).

Statistics were performed using the one-way ANOVA test (A–J and M–O) or Student's t test (K and L). Ns, not significant; \*\*p < 0.001, \*\*\*\*p < 0.0001. Data are mean  $\pm$  SD.



# Cell Metabolism Article

knockout did not increase IL-6 expression in 3T3-L1 adipocytes, which was rescued by  $\rm H_2O_2$  (a hazardous ROS) treatment (Figure 6I). Consistently, the elevated FFA release induced by PA-treated AML12 exosomes was abrogated by NAC treatment (Figure 6J).  $\rm H_2O_2$  significantly increased FFA release in 3T3-L1 adipocytes pretreated with exosomes from PA-treated AML12 cells with Trmt10c knockout (Figure 6J).

IL-6 promotes lipolysis of adipocytes by activating ATGL via increasing CGI-58. 66 We observed that levels of CGI-58 in mammary adipocytes of mice injected with PA-treated AML12 exosomes were significantly higher (Figure 6K), which was accompanied by the enhanced activity of ATGL (Figure 6L). The upregulation of CGI-58 and enhanced ATGL activity were recapitulated in 3T3-L1 adipocytes incubated with PA-treated AML12 exosomes (Figures 6M and 6N). *Trmt10c* knockout in AML12 cells abrogated the PA-treated AML12 exosome-mediated elevation of CGI-58 expression, ATGL activity, and FFA production in 3T3-L1 adipocytes, which was rescued by IL-6 over-expression in adipocytes (Figures 6M-6O and S7L). ATGL inhibition by atglistatin completely abolished the IL-6-mediated rescue of FFA release (Figure 6O).

Tumor cells also stimulate adipocyte lipolysis by secreting IL-6. <sup>67</sup> We observed that the elevation of FFA released from mammary adipocytes in EO771 tumor-bearing mice induced by fatty liver exosome injection was partially reduced by *II6* knockout in tumor cells (Figures S7M and S7N). In summary, these data suggested that exosomal TRMT10C promotes IL-6 production by increasing mitochondrial ROS via m<sup>1</sup>A modification of Nd5 and Nd6 mRNAs. Subsequently, adipocyte IL-6 induced by exosomal TRMT10C, together with tumor-derived IL-6, enhances FFA release by stimulating CGI-58-ATGL-mediated lipolysis.

# ErbB4\* exosomes predict the prognosis of patients with breast cancer and comorbid NAFLD

To investigate the clinical importance of ErbB4<sup>+</sup> exosomes, we obtained plasma samples from 3.013 patients with breast cancer. including 731 patients with NAFLD and 2,282 patients without NAFLD (Table S6). Patients with breast cancer and comorbid NAFLD exhibited significantly elevated levels of ErbB4 on circulating exosomes (crExos) compared with those without NAFLD (Figure 7A). Levels of plasma ErbB4<sup>+</sup> exosomes significantly increased in correlation with the progression of NAFLD severity (Figure 7B). Furthermore, we evaluated the prognostic relevance of ErbB4<sup>+</sup> crExos in patients with breast cancer who had NAFLD (Table S7). The ErbB4+ crExoshigh group presented poorer DFS and OS compared with the ErbB4+ crExos low group across all subtypes of breast cancer (Figures 7C-7F). Multivariate Cox regression analysis confirmed the ErbB4+ crExos as an independent prognostic marker for survival of patients with breast cancer who had NAFLD (Table S8). Collectively, these findings suggested that ErbB4+ crExos may serve as a potential non-invasive prognostic biomarker for patients with breast cancer and comorbid NAFLD.

# **DISCUSSION**

Exosomes derived from primary tumors create a pre-metastatic niche in distant organs. 42,68 Here, we uncovered an opposite direction of inter-organ exosome communication in malignant dis-

eases by showing exosomes derived from a distant organ with metabolic disorders foster a pro-tumorigenic milieu for primary tumors.

The impact of NAFLD on extrahepatic cancers has recently attracted increased attention. However, the mechanisms responsible for the connection between extrahepatic cancer and NAFLD remain poorly defined.<sup>2</sup> It has been reported that the only non-liver malignancy significantly correlated with NAFLD in women is breast cancer in a large-scale cohort study. This clinical observation suggests a specific distant communication of metabolic information between a digestive organ and a female reproductive organ beyond the reported general factors, such as systemic insulin resistance 69-71 and pro-inflammatory cytokines. 12 Here, we showed that fatty liver hepatocyte-derived exosomes preferentially bind to mammary adipocytes, which exhibit the highest level of lipolysis among all WATs, and elicit a protumorigenic niche in the breast. Studies have shown a relationship between fatty livers and increased lipolysis, which is attributed to systemic insulin resistance.<sup>73</sup> Therefore, our study expands the current paradigm of NAFLD-related lipolysis by highlighting the role of fatty liver exosomes. Moreover, a previous study shows that EVs secreted from cancer cells disrupt lipid metabolism in livers.<sup>20</sup> Our data support this study and further suggest that fatty livers and breast cancer form a vicious cycle via EVs.

Tissue tropism of exosomes is determined by ligands on the surface of exosomes and specific expression of their receptors in tissues.42 Nrg4 are subjected to extensive alternative mRNA splicing and therefore have diverse protein products, including transmembrane proteins and secreted extracellular fragments.74,75 Our data demonstrated that ErbB4 integrated in the membrane of fatty hepatocyte-derived exosomes binds to Nrg4 in mammary adipocytes and consequently dictates the accumulation of exosomes from fatty livers in breast adipose. Interestingly, it has been reported that soluble Nrg4 activates ErbB4 signaling in hepatocytes, suppresses de novo lipogenesis, and inhibits NAFLD progression. 45,76 These seemingly contradicting observations can be reconciled by the opposite effects of bidirectional signaling molecules. For example, sympathetic axons secrete tumor necrosis factor alpha (TNF-α), which suppresses neurite growth via TNF receptor 1 (TNFR1).77,78 Conversely, soluble forms of TNFR1 act as a ligand of membrane-integrated TNF- $\alpha$  and enhance axon growth via TNF- $\alpha$ reverse signals.<sup>79</sup> Similar opposite bidirectional effects have also been reported with receptor activator of nuclear factorkappa B (RANK) and RANK ligand (RANKL). Osteocytic RANKL binds to RANK in osteoclasts to induce bone removal. In contrast, vesicular RANK derived from osteoclasts promotes bone formation by binding to membrane-integrated RANKL in osteoblasts.80,81 Together with these previous reports, our data demonstrated an emerging concept that forward and reverse signaling of the same molecular couples may exert different or even opposite functions in different models.

Consistent with a previous study, we found that Nrg4 is also highly expressed in BATs in mice. 45 However, the relevance of WATs as an Nrg4 source is more pronounced in humans, as BATs are scarce in adult humans. 45 Recent studies show that tumor cells induce the browning of WATs, which promotes tumor metastasis 82 and exacerbates cancer-associated cachexia. 83 These events are more relevant to the advanced stage of cancer.

# **Article**



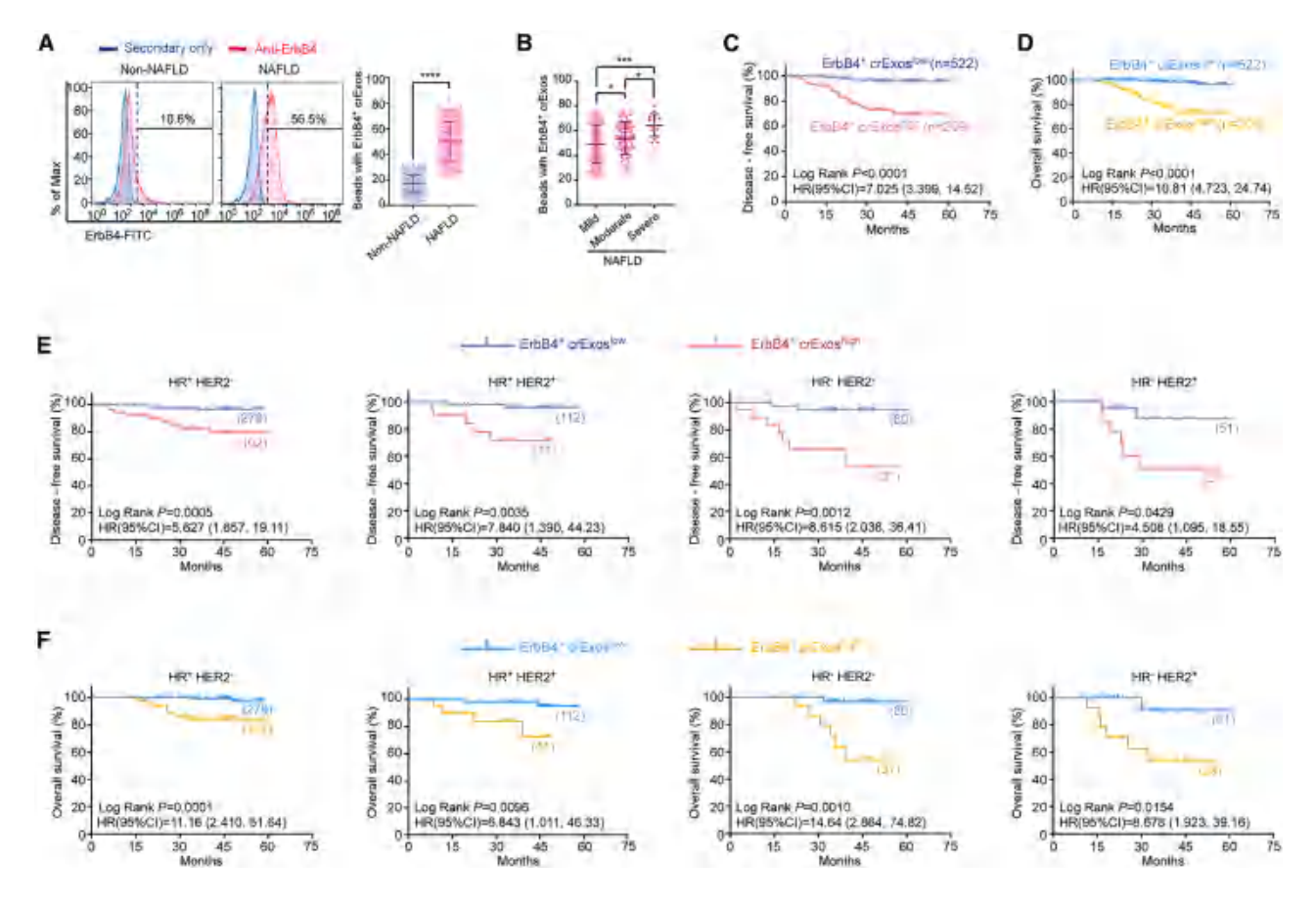


Figure 7. ErbB4<sup>+</sup> exosomes predict the prognosis of patients with breast cancer and comorbid NAFLD

(A and B) Circulating exosomes (crExos) were isolated from the plasma of 3,013 patients with breast cancer, of whom 731 had comorbid NAFLD. (A) Representative histograms (left) and quantification (right) of the percentage of ErbB4+ exosomes.

(B) Quantification of the percentages of ErbB4<sup>+</sup> exosomes across different NAFLD severities.

(C and D) Kaplan-Meier curves for DFS (C) and OS (D) of patients with breast cancer and comorbid NAFLD with high and low levels of ErbB4<sup>+</sup> crExos. (E and F) Kaplan-Meier curves for DFS (E) and OS (F) of patients with breast cancer and comorbid NAFLD, stratified by high or low levels of plasma ErbB4<sup>+</sup> crExos in different subtypes.

Statistics were performed using the Mann-Whitney U test (A), the Kruskal-Wallis test (B), or the two-sided log-rank test (C-F). p < 0.05, p < 0.001, p < 0.001, p < 0.001. Data are represented as mean p < 0.001.

See also Tables S6-S8.

However, our study focuses on the early dynamics of tumor initiation and primary tumor development. Among WATs, mammary fat pads exhibit the highest Nrg4 expression and the highest fatty liver exosome enrichment. Furthermore, epithelial cells are directly embedded within fat tissues in mammary glands. Therefore, mammary epithelial cells have a closer proximity to adipocytes than epithelial cells in other organs, which renders them more susceptible to pro-tumor signals derived from adipocytes. Previous in vitro data show that Nrg4 knockdown in 3T3-L1 adipocytes results in increased levels of lipolysis.84 Interestingly, our in vivo data showed that FFA release levels were comparable in adipocytes from wild-type mice and mice with adipocyte-specific depletion of Nrg4. Consistently, it has been reported that Nrg4 knockout mice have similar plasma triglyceride and non-esterified fatty acid levels to wild-type ones. 85 The disparity is probably due to differences between a cell line and adipocytes in vivo.

Adipocytes serve as critical functional components within the tumor microenvironment. 86,87 The notion that adipocyte-derived

lipids provide potent energy sources that fuel the progression of tumor cells<sup>8,11,12</sup> is further supported by our study. However, although the role of adipocytes in cancer development has been well documented, the mechanisms of adipocyte disorder in the tumor microenvironment are much less studied. Emerging reports demonstrate that biological mediators secreted from cancer cells alter signaling and functions of adipocytes. 8,11,67,82,88 Different from this conventional wisdom, our study showed that mammary adipocytes can be remotely regulated by TRMT10C in exosomes derived from a digestive organ with lipid metabolic disorder. Fatty acids can be transported from adipocytes to the extracellular space either by passive diffusion<sup>89</sup> or by facilitating proteins, including fatty acid translocase/CD36.90 We showed that fatty liver exosome-induced FFAs released from mammary adipocytes are taken up by breast cancer cells via FATP1 and FATP4.

TRMT10C necessitates the cofactor SDR5C1 to demonstrate methyltransferase activity on mitochondrial tRNAs, 55,91 while it





acts independently to methylate mitochondrial mRNAs. 57,92 m<sup>1</sup>A modifications at coding sequence regions in mitochondrial RNA can prevent the translation of modified codons due to the Watson-Crick disruptive nature. 57,92,93 Although endogenous expression of TRMT10C has been documented to be linked to mitochondrial dysfunction<sup>92</sup> and cancer progression,<sup>94</sup> the role of exogenous TRMT10C derived from other cells is unknown. Here, we found that TRMT10C could be shuttled from hepatocytes to mammary adipocytes via exosomes. The imported TRMT10C was finally located in the recipients' mitochondria, probably due to the mitochondrial targeting signals of TRMT10C.91 Similar to the function of endogenous TRMT10C, exogenous TRMT10C mediates m1A hypermethylation and translation suppression of Nd5 and Nd6 mRNAs in mammary adipocytes. ND5 and ND6 are oxidative phosphorylation proteins responsible for the electron transport chain, disruption of which results in excessive mitochondrial ROS production. 92,95,96 We<sup>97</sup> and others <sup>64,65</sup> have shown that mitochondrial ROS activates the nuclear factor κB (NF-κB) pathway, which upregulates IL-6 expression. Furthermore, IL-6 has been demonstrated to trigger lipolysis and FFA release in adipocytes by activating the JAK-STAT signaling pathway. 66,98 In agreement, we observed that TRMT10C-induced ROS causes a marked increase in FFA release in adipocytes via IL-6.

In summary, we revealed a liver-breast metabolic axis that drives tumor development and identified circulating ErbB4<sup>+</sup> exosomes as a plasma-based biomarker and potential therapeutic target for breast cancer in patients with NAFLD.

# **Limitations of the study**

Although we demonstrate a liver-breast metabolic interaction in promoting mammary cancer development, there are limitations in our study. First, this study primarily focuses on the role of fatty liver exosomes in supporting primary breast tumors and is limited for pre-metastatic niches and metastases in general. The effects of fatty liver exosomes in pre-metastatic niche warrant further exploration, given the critical role of EVs in promoting pre-metastatic niche formation and subsequent metastasis. <sup>19,34,42</sup> Another limitation is that our study does not include blood insulin data of patients with breast cancer. Additional investigations are needed to assess whether insulin levels contribute to lipolysis in mammary adipocytes induced by fatty liver exosomes in humans.

# RESOURCE AVAILABILITY

### **Lead contact**

Further information and requests for resources and reagents should be directed to and will be fulfilled by the lead contact, Shicheng Su (sushch@mail.svsu.edu.cn).

### **Materials availability**

This study did not generate unique reagents.

# Data and code availability

- All materials and related protocols can be found in the STAR Methods section of this paper, with relevant papers also cited for further reference. Additional information can be obtained from the authors upon reasonable request, provided permission is granted by Sun Yat-Sen Memorial Hospital.
- This paper does not report custom code.

- The mass spectrometry proteomics data have been deposited to the ProteomeXchange Consortium via the PRIDE partner repository with the dataset identifier PRIDE: PXD067453.
- Unprocessed data in this manuscript are available in Data S1.

### **ACKNOWLEDGMENTS**

This work was supported by grants from the National Key Research and Development Program of China (2023YFC3404500), the Guangdong Major Project of Basic Research (2023B0303000018), the Natural Science Foundation of China (92057210, 82125017, 92359302, and 82322030), the New Cornerstone Science Foundation through the New Cornerstone Investigator Program and the XPLORER PRIZE, the Guangdong Basic and Applied Basic Research Foundation (2024B1515040006), the Guangdong Provincial Clinical Research Center for Breast Diseases (2023B110005), and the Guangdong Basic and Applied Basic Research Foundation (2025A1515012431).

### **AUTHOR CONTRIBUTIONS**

C.L., Y. Lu, Y. Li, H.D., J.C., D.H., L.Y., J.J., D.K., and S.S. conceived ideas and designed experiments. S.S. conducted experiments. C.L., Y. Lu, Y. Li, and T.L. performed experiments and acquired data. M.G., B.Z., and J.L. analyzed data. C.L., Y. Lu, Y. Li, and S.S. wrote the paper.

### **DECLARATION OF INTERESTS**

The authors declare no competing interests.

### **STAR**\*METHODS

Detailed methods are provided in the online version of this paper and include the following:

- KEY RESOURCES TABLE
- EXPERIMENTAL MODEL AND SUBJECT DETAILS
  - o Patients and plasma samples
  - o Experimental animals
  - o Cell lines and cell culture
- METHOD DETAILS
  - Meta-analysis
  - Dietary interventions
  - Animal studies
  - Whole-mount mammary gland carmine staining
  - o Orthotopic mouse liver transplantation
  - o Histological analyses
  - o Isolation of cells from mouse livers
  - Preparation of conditioned medium (CM) from mouse livers and cells
  - o CM fractionation
  - O Serum exosome quantification
  - In vivo treatment with CM and CM fractions
  - o In vivo exosome treatment
  - In vivo distribution of exosomes
  - o Neutralization of ErbB4 in exosomes
  - Western blot
  - o Lipoprotein isolation
  - o Transmission electron microscope (TEM) analysis
  - TEM analysis for cryosections
  - o Isolation of primary cells from mouse mammary fat pads
  - o Isolation of tumor-infiltrating leukocytes
  - $\circ\,$  Flow cytometry and cell sorting
  - o Immunofluorescence
  - o Liquid chromatography-tandem mass spectrometry (LC-MS/MS)
  - o siRNA transfection
  - Flow cytometry analysis of ErbB4 levels on exosomes
  - o Enzyme-linked immunosorbent assay (ELISA)
  - $\circ$  Gene knockout using CRISPR/Cas9

# **Article**



- o Online data analysis
- Adipogenic differentiation
- o Quantification of free fatty acid (FFA)
- o Assessment of lipid transfer between cells
- o Isolation of primary tumor cells
- o Quantitative real-time PCR (qRT-PCR)
- o Lentiviral vector-mediated overexpression
- o Lipidomic analysis
- Cell proliferation assay
- o Cytosolic and mitochondrial fractionation
- Mitochondrial RNA purification
- Quantitative analysis of RNA modification levels using UPLC-MS/MS
- o m<sup>1</sup>A RNA immunoprecipitation-qPCR
- Oxygen consumption rate (OCR) assay
- Mitochondrial ribosome profiling
- o ATGL activity assay
- Detection of ErbB4<sup>+</sup> exosomes in human plasma
- QUANTIFICATION AND STATISTICAL ANALYSIS

### SUPPLEMENTAL INFORMATION

Supplemental information can be found online at https://doi.org/10.1016/j.cmet.2025.08.012.

Received: November 14, 2024 Revised: July 16, 2025 Accepted: August 30, 2025

### **REFERENCES**

- Fan, J.G., Kim, S.U., and Wong, V.W.S. (2017). New trends on obesity and NAFLD in Asia. J. Hepatol. 67, 862–873. https://doi.org/10.1016/j. ihep.2017.06.003.
- Thomas, J.A., Kendall, B.J., El-Serag, H.B., Thrift, A.P., and Macdonald, G.A. (2024). Hepatocellular and extrahepatic cancer risk in people with non-alcoholic fatty liver disease. Lancet Gastroenterol. Hepatol. 9, 159–169. https://doi.org/10.1016/S2468-1253(23)00275-3.
- Powell, E.E., Wong, V.W.S., and Rinella, M. (2021). Non-alcoholic fatty liver disease. Lancet 397, 2212–2224. https://doi.org/10.1016/S0140-6736(20)32511-3.
- Huang, D.Q., El-Serag, H.B., and Loomba, R. (2021). Global epidemiology of NAFLD-related HCC: trends, predictions, risk factors and prevention. Nat. Rev. Gastroenterol. Hepatol. 18, 223–238. https://doi.org/10.1038/s41575-020-00381-6.
- Ye, Q., Zou, B., Yeo, Y.H., Li, J., Huang, D.Q., Wu, Y., Yang, H., Liu, C., Kam, L.Y., Tan, X.X.E., et al. (2020). Global prevalence, incidence, and outcomes of non-obese or lean non-alcoholic fatty liver disease: a systematic review and meta-analysis. Lancet Gastroenterol. Hepatol. 5, 739–752. https://doi.org/10.1016/S2468-1253(20)30077-7.
- Mantovani, A., Petracca, G., Beatrice, G., Csermely, A., Tilg, H., Byrne, C. D., and Targher, G. (2022). Non-alcoholic fatty liver disease and increased risk of incident extrahepatic cancers: a meta-analysis of observational cohort studies. Gut 71, 778–788. https://doi.org/10.1136/ gutjnl-2021-324191.
- Kim, G.A., Lee, H.C., Choe, J., Kim, M.J., Lee, M.J., Chang, H.S., Bae, I. Y., Kim, H.K., An, J., Shim, J.H., et al. (2017). Association between nonalcoholic fatty liver disease and cancer incidence rate. Published online November 2, 2017. J. Hepatol. https://doi.org/10.1016/j.jhep.2017. 09.012.
- Panaroni, C., Fulzele, K., Mori, T., Siu, K.T., Onyewadume, C., Maebius, A., and Raje, N. (2022). Multiple myeloma cells induce lipolysis in adipocytes and uptake fatty acids through fatty acid transporter proteins. Blood 139, 876–888. https://doi.org/10.1182/blood.2021013832.

- Rosen, E.D., and Spiegelman, B.M. (2006). Adipocytes as regulators of energy balance and glucose homeostasis. Nature 444, 847–853. https://doi.org/10.1038/nature05483.
- Brown, K.A., and Scherer, P.E. (2023). Update on adipose tissue and cancer. Endocr. Rev. 44, 961–974. https://doi.org/10.1210/endrev/ bnad015.
- Nieman, K.M., Kenny, H.A., Penicka, C.V., Ladanyi, A., Buell-Gutbrod, R., Zillhardt, M.R., Romero, I.L., Carey, M.S., Mills, G.B., Hotamisligil, G.S., et al. (2011). Adipocytes promote ovarian cancer metastasis and provide energy for rapid tumor growth. Nat. Med. 17, 1498–1503. https://doi.org/10.1038/nm.2492.
- Zhang, M., Di Martino, J.S., Bowman, R.L., Campbell, N.R., Baksh, S.C., Simon-Vermot, T., Kim, I.S., Haldeman, P., Mondal, C., Yong-Gonzales, V., et al. (2018). Adipocyte-derived lipids mediate melanoma progression via FATP proteins. Cancer Discov. 8, 1006–1025. https://doi.org/10. 1158/2159-8290.CD-17-1371.
- Kalluri, R., and McAndrews, K.M. (2023). The role of extracellular vesicles in cancer. Cell 186, 1610–1626. https://doi.org/10.1016/j.cell.2023. 03.010.
- Cheng, L., and Hill, A.F. (2022). Therapeutically harnessing extracellular vesicles. Nat. Rev. Drug Discov. 21, 379–399. https://doi.org/10.1038/ s41573-022-00410-w.
- Tkach, M., and Théry, C. (2016). Communication by extracellular vesicles: where we are and where we need to go. Cell 164, 1226–1232. https://doi.org/10.1016/j.cell.2016.01.043.
- Borcherding, N., Jia, W., Giwa, R., Field, R.L., Moley, J.R., Kopecky, B.J., Chan, M.M., Yang, B.Q., Sabio, J.M., Walker, E.C., et al. (2022). Dietary lipids inhibit mitochondria transfer to macrophages to divert adipocytederived mitochondria into the blood. Cell Metab. 34, 1499–1513.e8. https://doi.org/10.1016/j.cmet.2022.08.010.
- Brestoff, J.R., Wilen, C.B., Moley, J.R., Li, Y., Zou, W., Malvin, N.P., Rowen, M.N., Saunders, B.T., Ma, H., Mack, M.R., et al. (2021). Intercellular mitochondria transfer to macrophages regulates white adipose tissue homeostasis and is impaired in obesity. Cell Metab. 33, 270–282.e8. https://doi.org/10.1016/j.cmet.2020.11.008.
- Patras, L., Shaashua, L., Matei, I., and Lyden, D. (2023). Immune determinants of the pre-metastatic niche. Cancer Cell 41, 546–572. https://doi.org/10.1016/j.ccell.2023.02.018.
- Peinado, H., Zhang, H., Matei, I.R., Costa-Silva, B., Hoshino, A., Rodrigues, G., Psaila, B., Kaplan, R.N., Bromberg, J.F., Kang, Y., et al. (2017). Pre-metastatic niches: organ-specific homes for metastases. Nat. Rev. Cancer 17, 302–317. https://doi.org/10.1038/nrc.2017.6.
- Wang, G., Li, J., Bojmar, L., Chen, H., Li, Z., Tobias, G.C., Hu, M., Homan, E.A., Lucotti, S., Zhao, F., et al. (2023). Tumour extracellular vesicles and particles induce liver metabolic dysfunction. Nature 618, 374–382. https://doi.org/10.1038/s41586-023-06114-4.
- Avgerinos, K.I., Spyrou, N., Mantzoros, C.S., and Dalamaga, M. (2019).
   Obesity and cancer risk: Emerging biological mechanisms and perspectives. Metabolism 92, 121–135. https://doi.org/10.1016/j.metabol.2018.
   11.001.
- World Health Organization. Regional Office for the Western Pacific (2000). The Asia-Pacific Perspective: Redefining Obesity and Its Treatment (Health Communications Australia). https://iris.who.int/ handle/10665/206936.
- Lee, Y.S., Lee, H.S., Chang, S.W., Lee, C.U., Kim, J.S., Jung, Y.K., Kim, J. H., Seo, Y.S., Yim, H.J., Lee, C.H., et al. (2019). Underlying nonalcoholic fatty liver disease is a significant factor for breast cancer recurrence after curative surgery. Medicine 98, e17277. https://doi.org/10.1097/MD. 0000000000017277
- 24. Ocak Duran, A., Yildirim, A., Inanc, M., Karaca, H., Berk, V., Bozkurt, O., Ozaslan, E., Ucar, M., and Ozkan, M. (2015). Hepatic steatosis is associated with higher incidence of liver metastasis in patients with metastatic breast cancer; an observational clinical study. J. BUON 20, 963–969.



# Cell Metabolism Article

- Jimba, S., Nakagami, T., Takahashi, M., Wakamatsu, T., Hirota, Y., Iwamoto, Y., and Wasada, T. (2005). Prevalence of non-alcoholic fatty liver disease and its association with impaired glucose metabolism in Japanese adults. Diabet. Med. 22, 1141–1145. https://doi.org/10.1111/ j.1464-5491.2005.01582.x.
- World Health Organization. (2006). Definition and diagnosis of diabetes mellitus and intermediate hyperglycaemia. Report of a WHO/IDF consultation. https://www.who.int/publications/i/item/definition-and-diagnosis-ofdiabetes-mellitus-and-intermediate-hyperglycaemia.
- Zhao, S., Jang, C., Liu, J., Uehara, K., Gilbert, M., Izzo, L., Zeng, X., Trefely, S., Fernandez, S., Carrer, A., et al. (2020). Dietary fructose feeds hepatic lipogenesis via microbiota-derived acetate. Nature 579, 586–591. https://doi.org/10.1038/s41586-020-2101-7.
- Hebbard, L., and George, J. (2011). Animal models of nonalcoholic fatty liver disease. Nat. Rev. Gastroenterol. Hepatol. 8, 35–44. https://doi.org/ 10.1038/nrgastro.2010.191.
- Yokota, S., Ueki, S., Ono, Y., Kasahara, N., Pérez-Gutiérrez, A., Kimura, S., Yoshida, O., Murase, N., Yasuda, Y., Geller, D.A., et al. (2016). Orthotopic mouse liver transplantation to study liver biology and allograft tolerance. Nat. Protoc. 11, 1163–1174. https://doi.org/10.1038/nprot. 2016.073.
- Miotto, P.M., Yang, C.H., Keenan, S.N., De Nardo, W., Beddows, C.A., Fidelito, G., Dodd, G.T., Parker, B.L., Hill, A.F., Burton, P.R., et al. (2024). Liver-derived extracellular vesicles improve whole-body glycae-mic control via inter-organ communication. Nat. Metab. 6, 254–272. https://doi.org/10.1038/s42255-023-00971-z.
- Chen, G., Huang, A.C., Zhang, W., Zhang, G., Wu, M., Xu, W., Yu, Z., Yang, J., Wang, B., Sun, H., et al. (2018). Exosomal PD-L1 contributes to immunosuppression and is associated with anti-PD-1 response. Nature 560, 382–386. https://doi.org/10.1038/s41586-018-0392-8.
- Cypess, A.M., Cannon, B., Nedergaard, J., Kazak, L., Chang, D.C., Krakoff, J., Tseng, Y.H., Schéele, C., Boucher, J., Petrovic, N., et al. (2025). Emerging debates and resolutions in brown adipose tissue research. Cell Metab. 37, 12–33. https://doi.org/10.1016/j.cmet.2024.11.002.
- Cypess, A.M. (2022). Reassessing human adipose tissue. N. Engl. J. Med. 386, 768–779. https://doi.org/10.1056/NEJMra2032804.
- Becker, A., Thakur, B.K., Weiss, J.M., Kim, H.S., Peinado, H., and Lyden,
   D. (2016). Extracellular vesicles in cancer: cell-to-cell mediators of metastasis. Cancer Cell 30, 836–848. https://doi.org/10.1016/j.ccell. 2016.10.009.
- van Niel, G., D'Angelo, G., and Raposo, G. (2018). Shedding light on the cell biology of extracellular vesicles. Nat. Rev. Mol. Cell Biol. 19, 213–228. https://doi.org/10.1038/nrm.2017.125.
- Garcia-Martin, R., Brandao, B.B., Thomou, T., Altindis, E., and Kahn, C. R. (2022). Tissue differences in the exosomal/small extracellular vesicle proteome and their potential as indicators of altered tissue metabolism. Cell Rep. 38, 110277. https://doi.org/10.1016/j.celrep.2021.110277.
- Xu, M., Xu, H.H., Lin, Y., Sun, X., Wang, L.J., Fang, Z.P., Su, X.H., Liang, X.J., Hu, Y., Liu, Z.M., et al. (2019). LECT2, a ligand for Tie1, plays a crucial role in liver fibrogenesis. Cell 178, 1478–1492.e20. https://doi.org/10.1016/j.cell.2019.07.021.
- Zhang, H., Chen, T., Ren, J., Xia, Y., Onuma, A., Wang, Y., He, J., Wu, J., Wang, H., Hamad, A., et al. (2021). Pre-operative exercise therapy triggers anti-inflammatory trained immunity of Kupffer cells through metabolic reprogramming. Nat. Metab. 3, 843–858. https://doi.org/10.1038/ s42255-021-00402-x.
- Winkler, M., Staniczek, T., Kürschner, S.W., Schmid, C.D., Schönhaber, H., Cordero, J., Kessler, L., Mathes, A., Sticht, C., Neßling, M., et al. (2021). Endothelial GATA4 controls liver fibrosis and regeneration by preventing a pathogenic switch in angiocrine signaling. J. Hepatol. 74, 380–393. https://doi.org/10.1016/j.jhep.2020.08.033.
- Tanimizu, N., Ichinohe, N., Sasaki, Y., Itoh, T., Sudo, R., Yamaguchi, T., Katsuda, T., Ninomiya, T., Tokino, T., Ochiya, T., et al. (2021). Generation of functional liver organoids on combining hepatocytes and cholangio-

- cytes with hepatobiliary connections ex vivo. Nat. Commun. *12*, 3390. https://doi.org/10.1038/s41467-021-23575-1.
- Mederacke, I., Dapito, D.H., Affò, S., Uchinami, H., and Schwabe, R.F. (2015). High yield and high-purity isolation of hepatic stellate cells from normal and fibrotic mouse livers. Nat. Protoc. 10, 305–315. https://doi. org/10.1038/nprot.2015.017.
- Hoshino, A., Costa-Silva, B., Shen, T.L., Rodrigues, G., Hashimoto, A., Tesic Mark, M., Molina, H., Kohsaka, S., Di Giannatale, A., Ceder, S., et al. (2015). Tumour exosome integrins determine organotropic metastasis. Nature 527, 329–335. https://doi.org/10.1038/nature15756.
- Joshi-Barve, S., Barve, S.S., Amancherla, K., Gobejishvili, L., Hill, D., Cave, M., Hote, P., and McClain, C.J. (2007). Palmitic acid induces production of proinflammatory cytokine interleukin-8 from hepatocytes. Hepatology 46, 823–830. https://doi.org/10.1002/hep.21752.
- 44. Wu, X., Poulsen, K.L., Sanz-Garcia, C., Huang, E., McMullen, M.R., Roychowdhury, S., Dasarathy, S., and Nagy, L.E. (2020). MLKL-dependent signaling regulates autophagic flux in a murine model of nonalcohol-associated fatty liver and steatohepatitis. J. Hepatol. 73, 616–627. https://doi.org/10.1016/j.jhep.2020.03.023.
- Wang, G.X., Zhao, X.Y., Meng, Z.X., Kern, M., Dietrich, A., Chen, Z., Cozacov, Z., Zhou, D., Okunade, A.L., Su, X., et al. (2014). The brown fat-enriched secreted factor Nrg4 preserves metabolic homeostasis through attenuation of hepatic lipogenesis. Nat. Med. 20, 1436–1443. https://doi.org/10.1038/nm.3713.
- Gassmann, M., Casagranda, F., Orioli, D., Simon, H., Lai, C., Klein, R., and Lemke, G. (1995). Aberrant neural and cardiac development in mice lacking the ErbB4 neuregulin receptor. Nature 378, 390–394. https://doi.org/10.1038/378390a0.
- Terstappen, G.C., Meyer, A.H., Bell, R.D., and Zhang, W. (2021).
   Strategies for delivering therapeutics across the blood-brain barrier.
   Nat. Rev. Drug Discov. 20, 362–383. https://doi.org/10.1038/s41573-021-00139-v.
- Pascual, G., Avgustinova, A., Mejetta, S., Martín, M., Castellanos, A., Attolini, C.S.O., Berenguer, A., Prats, N., Toll, A., Hueto, J.A., et al. (2017). Targeting metastasis-initiating cells through the fatty acid receptor CD36. Nature 541, 41–45. https://doi.org/10.1038/nature20791.
- Schatoff, E.M., Goswami, S., Zafra, M.P., Foronda, M., Shusterman, M., Leach, B.I., Katti, A., Diaz, B.J., and Dow, L.E. (2019). Distinct colorectal cancer-associated APC mutations dictate response to tankyrase inhibition. Cancer Discov. 9, 1358–1371. https://doi.org/10.1158/2159-8290. CD-19-0289.
- Alicea, G.M., Rebecca, V.W., Goldman, A.R., Fane, M.E., Douglass, S. M., Behera, R., Webster, M.R., Kugel, C.H., 3rd, Ecker, B.L., Caino, M. C., et al. (2020). Changes in aged fibroblast lipid metabolism induce age-dependent melanoma cell resistance to targeted therapy via the fatty acid transporter FATP2. Cancer Discov. 10, 1282–1295. https://doi.org/10.1158/2159-8290.CD-20-0329.
- Veglia, F., Tyurin, V.A., Blasi, M., De Leo, A., Kossenkov, A.V., Donthireddy, L., To, T.K.J., Schug, Z., Basu, S., Wang, F., et al. (2019). Fatty acid transport protein 2 reprograms neutrophils in cancer. Nature 569, 73–78. https://doi.org/10.1038/s41586-019-1118-2.
- Kumagai, S., Togashi, Y., Sakai, C., Kawazoe, A., Kawazu, M., Ueno, T., Sato, E., Kuwata, T., Kinoshita, T., Yamamoto, M., et al. (2020). An oncogenic alteration creates a microenvironment that promotes tumor progression by conferring a metabolic advantage to regulatory T cells. Immunity 53, 187–203.e8. https://doi.org/10.1016/j.immuni.2020.06.016.
- Rodrigues, G., Hoshino, A., Kenific, C.M., Matei, I.R., Steiner, L., Freitas, D., Kim, H.S., Oxley, P.R., Scandariato, I., Casanova-Salas, I., et al. (2019). Tumour exosomal CEMIP protein promotes cancer cell colonization in brain metastasis. Nat. Cell Biol. 21, 1403–1412. https://doi.org/10.1038/s41556-019-0404-4.
- 54. Yoshida, M., Satoh, A., Lin, J.B., Mills, K.F., Sasaki, Y., Rensing, N., Wong, M., Apte, R.S., and Imai, S.I. (2019). Extracellular vesicle-contained eNAMPT delays aging and extends lifespan in mice. Cell Metab. 30, 329–342.e5. https://doi.org/10.1016/j.cmet.2019.05.015.

# **Article**



- 55. Vilardo, E., Nachbagauer, C., Buzet, A., Taschner, A., Holzmann, J., and Rossmanith, W. (2012). A subcomplex of human mitochondrial RNase P is a bifunctional methyltransferase–extensive moonlighting in mitochondrial tRNA biogenesis. Nucleic Acids Res. 40, 11583–11593. https://doi. org/10.1093/nar/gks910.
- Reinhard, L., Sridhara, S., and Hällberg, B.M. (2017). The MRPP1/MRPP2 complex is a tRNA-maturation platform in human mitochondria. Nucleic Acids Res. 45. 12469–12480. https://doi.org/10.1093/nar/qkx902.
- Safra, M., Sas-Chen, A., Nir, R., Winkler, R., Nachshon, A., Bar-Yaacov, D., Erlacher, M., Rossmanith, W., Stern-Ginossar, N., and Schwartz, S. (2017). The m1A landscape on cytosolic and mitochondrial mRNA at single-base resolution. Nature 551, 251–255. https://doi.org/10.1038/nature/24456
- Kampjut, D., and Sazanov, L.A. (2020). The coupling mechanism of mammalian respiratory complex I. Science 370, eabc4209. https://doi. org/10.1126/science.abc4209.
- Ishikawa, K., Takenaga, K., Akimoto, M., Koshikawa, N., Yamaguchi, A., Imanishi, H., Nakada, K., Honma, Y., and Hayashi, J.I. (2008). ROSgenerating mitochondrial DNA mutations can regulate tumor cell metastasis. Science 320, 661–664. https://doi.org/10.1126/science.1156906.
- Kuang, W., Jin, H., Yang, F., Chen, X., Liu, J., Li, T., Chang, Y., Liu, M., Xu, Z., Huo, C., et al. (2022). ALKBH3-dependent m<sup>1</sup>A demethylation of Aurora A mRNA inhibits ciliogenesis. Cell Discov. 8, 25. https://doi.org/10.1038/s41421-022-00385-3.
- 61. Wu, Y., Chen, Z., Xie, G., Zhang, H., Wang, Z., Zhou, J., Chen, F., Li, J., Chen, L., Niu, H., et al. (2022). RNA m<sup>1</sup>A methylation regulates glycolysis of cancer cells through modulating ATP5D. Proc. Natl. Acad. Sci. USA 119, e2119038119. https://doi.org/10.1073/pnas.2119038119.
- Morscher, R.J., Ducker, G.S., Li, S.H.J., Mayer, J.A., Gitai, Z., Sperl, W., and Rabinowitz, J.D. (2018). Mitochondrial translation requires folatedependent tRNA methylation. Nature 554, 128–132. https://doi.org/10. 1038/nature25460.
- 63. Nathan, C., and Cunningham-Bussel, A. (2013). Beyond oxidative stress: an immunologist's guide to reactive oxygen species. Nat. Rev. Immunol. *13*, 349–361. https://doi.org/10.1038/nri3423.
- 64. He, F., Huang, Y., Song, Z., Zhou, H.J., Zhang, H., Perry, R.J., Shulman, G.I., and Min, W. (2021). Mitophagy-mediated adipose inflammation contributes to type 2 diabetes with hepatic insulin resistance. J. Exp. Med. 218, e20201416. https://doi.org/10.1084/jem.20201416.
- 65. Li, Z., Low, V., Luga, V., Sun, J., Earlie, E., Parang, B., Shobana Ganesh, K., Cho, S., Endress, J., Schild, T., et al. (2022). Tumor-produced and aging-associated oncometabolite methylmalonic acid promotes cancer-associated fibroblast activation to drive metastatic progression. Nat. Commun. 13, 6239. https://doi.org/10.1038/s41467-022-33862-0.
- Perry, R.J., Camporez, J.G., Kursawe, R., Titchenell, P.M., Zhang, D., Perry, C.J., Jurczak, M.J., Abudukadier, A., Han, M.S., Zhang, X.M., et al. (2015). Hepatic acetyl CoA links adipose tissue inflammation to hepatic insulin resistance and type 2 diabetes. Cell 160, 745–758. https:// doi.org/10.1016/j.cell.2015.01.012.
- 67. Rupert, J.E., Narasimhan, A., Jengelley, D.H.A., Jiang, Y., Liu, J., Au, E., Silverman, L.M., Sandusky, G., Bonetto, A., Cao, S., et al. (2021). Tumorderived IL-6 and trans-signaling among tumor, fat, and muscle mediate pancreatic cancer cachexia. J. Exp. Med. 218, e20190450. https://doi.org/10.1084/jem.20190450.
- Costa-Silva, B., Aiello, N.M., Ocean, A.J., Singh, S., Zhang, H., Thakur, B. K., Becker, A., Hoshino, A., Mark, M.T., Molina, H., et al. (2015). Pancreatic cancer exosomes initiate pre-metastatic niche formation in the liver. Nat. Cell Biol. 17, 816–826. https://doi.org/10.1038/ncb3169.
- Samuel, V.T., and Shulman, G.I. (2018). Nonalcoholic fatty liver disease as a nexus of metabolic and hepatic diseases. Cell Metab. 27, 22–41. https://doi.org/10.1016/j.cmet.2017.08.002.
- Lonardo, A., Nascimbeni, F., Mantovani, A., and Targher, G. (2018).
   Hypertension, diabetes, atherosclerosis and NASH: Cause or consequence? J. Hepatol. 68, 335–352. https://doi.org/10.1016/j.jhep.2017.

- Petersen, M.C., Vatner, D.F., and Shulman, G.I. (2017). Regulation of hepatic glucose metabolism in health and disease. Nat. Rev. Endocrinol. 13, 572–587. https://doi.org/10.1038/nrendo.2017.80.
- Adolph, T.E., Grander, C., Grabherr, F., and Tilg, H. (2017). Adipokines and non-alcoholic fatty liver disease: multiple interactions. Int. J. Mol. Sci. 18, 1649. https://doi.org/10.3390/ijms18081649.
- Samuel, V.T., and Shulman, G.I. (2012). Mechanisms for insulin resistance: common threads and missing links. Cell 148, 852–871. https://doi.org/10.1016/j.cell.2012.02.017.
- Hayes, N.V.L., Blackburn, E., Smart, L.V., Boyle, M.M., Russell, G.A., Frost, T.M., Morgan, B.J.T., Baines, A.J., and Gullick, W.J. (2007). Identification and characterization of novel spliced variants of neuregulin 4 in prostate cancer. Clin. Cancer Res. 13, 3147–3155. https://doi.org/ 10.1158/1078-0432.CCR-06-2237.
- Hayes, N.V., Newsam, R.J., Baines, A.J., and Gullick, W.J. (2008). Characterization of the cell membrane-associated products of the Neuregulin 4 gene. Oncogene 27, 715–720. https://doi.org/10.1038/sj. onc.1210689.
- Guo, L., Zhang, P., Chen, Z., Xia, H., Li, S., Zhang, Y., Kobberup, S., Zou, W., and Lin, J.D. (2017). Hepatic neuregulin 4 signaling defines an endocrine checkpoint for steatosis-to-NASH progression. J. Clin. Invest. 127, 4449–4461. https://doi.org/10.1172/JCl96324.
- Neumann, H., Schweigreiter, R., Yamashita, T., Rosenkranz, K., Wekerle, H., and Barde, Y.A. (2002). Tumor necrosis factor inhibits neurite outgrowth and branching of hippocampal neurons by a rho-dependent mechanism. J. Neurosci. 22, 854–862. https://doi.org/10.1523/ JNEUROSCI.22-03-00854.2002.
- Gutierrez, H., O'Keeffe, G.W., Gavaldà, N., Gallagher, D., and Davies, A.M. (2008). Nuclear factor kappa B signaling either stimulates or inhibits neurite growth depending on the phosphorylation status of p65/RelA. J. Neurosci. 28, 8246–8256. https://doi.org/10.1523/JNEUROSCI.1941-08.2008.
- Kisiswa, L., Osório, C., Erice, C., Vizard, T., Wyatt, S., and Davies, A.M. (2013). TNFα reverse signaling promotes sympathetic axon growth and target innervation. Nat. Neurosci. *16*, 865–873. https://doi.org/10.1038/pp.3430
- Ikebuchi, Y., Aoki, S., Honma, M., Hayashi, M., Sugamori, Y., Khan, M., Kariya, Y., Kato, G., Tabata, Y., Penninger, J.M., et al. (2018). Coupling of bone resorption and formation by RANKL reverse signalling. Nature 561, 195–200. https://doi.org/10.1038/s41586-018-0482-7.
- 81. Jones, D.H., Kong, Y.Y., and Penninger, J.M. (2002). Role of RANKL and RANK in bone loss and arthritis. Ann. Rheum. Dis. *61*, ii32–ii39. https://doi.org/10.1136/ard.61.suppl\_2.ii32.
- Wei, G., Sun, H., Dong, K., Hu, L., Wang, Q., Zhuang, Q., Zhu, Y., Zhang, X., Shao, Y., Tang, H., et al. (2021). The thermogenic activity of adjacent adipocytes fuels the progression of ccRCC and compromises anti-tumor therapeutic efficacy. Cell Metab. 33, 2021–2039.e8. https://doi.org/10.1016/j.cmet.2021.08.012.
- Kir, S., White, J.P., Kleiner, S., Kazak, L., Cohen, P., Baracos, V.E., and Spiegelman, B.M. (2014). Tumour-derived PTH-related protein triggers adipose tissue browning and cancer cachexia. Nature 513, 100–104. https://doi.org/10.1038/nature13528.
- Díaz-Sáez, F., Balcells, C., Rosselló, L., López-Soldado, I., Romero, M., Sebastián, D., López-Soriano, F.J., Busquets, S., Cascante, M., Ricart, W., et al. (2024). Neuregulin 4 downregulation alters mitochondrial morphology and induces oxidative stress in 3T3-L1 adipocytes. Int. J. Mol. Sci. 25, 11718. https://doi.org/10.3390/ijms252111718.
- Chen, Z., Wang, G.X., Ma, S.L., Jung, D.Y., Ha, H., Altamimi, T., Zhao, X. Y., Guo, L., Zhang, P., Hu, C.R., et al. (2017). Nrg4 promotes fuel oxidation and a healthy adipokine profile to ameliorate diet-induced metabolic disorders. Mol. Metab. 6, 863–872. https://doi.org/10.1016/j.molmet. 2017.03.016.
- Wu, Q., Li, B., Li, Z., Li, J., Sun, S., and Sun, S. (2019). Cancer-associated adipocytes: key players in breast cancer progression. J. Hematol. Oncol. 12, 95. https://doi.org/10.1186/s13045-019-0778-6.



- Attané, C., and Muller, C. (2020). Drilling for oil: tumor-surrounding adipocytes fueling cancer. Trends Cancer 6, 593–604. https://doi.org/10.1016/j.trecan.2020.03.001.
- Dirat, B., Bochet, L., Dabek, M., Daviaud, D., Dauvillier, S., Majed, B., Wang, Y.Y., Meulle, A., Salles, B., Le Gonidec, S., et al. (2011). Cancer-associated adipocytes exhibit an activated phenotype and contribute to breast cancer invasion. Cancer Res. 71, 2455–2465. https://doi.org/10.1158/0008-5472.CAN-10-3323.
- Hamilton, J.A., and Kamp, F. (1999). How are free fatty acids transported in membranes? Is it by proteins or by free diffusion through the lipids? Diabetes 48, 2255–2269. https://doi.org/10.2337/diabetes.48.12.2255.
- Daquinag, A.C., Gao, Z., Fussell, C., Immaraj, L., Pasqualini, R., Arap, W., Akimzhanov, A.M., Febbraio, M., and Kolonin, M.G. (2021). Fatty acid mobilization from adipose tissue is mediated by CD36 posttranslational modifications and intracellular trafficking. JCI Insight 6, e147057. https://doi.org/10.1172/jci.insight.147057.
- Bhatta, A., Dienemann, C., Cramer, P., and Hillen, H.S. (2021). Structural basis of RNA processing by human mitochondrial RNase P. Nat. Struct. Mol. Biol. 28, 713–723. https://doi.org/10.1038/s41594-021-00637-y.
- Jörg, M., Plehn, J.E., Kristen, M., Lander, M., Walz, L., Lietz, C., Wijns, J., Pichot, F., Rojas-Charry, L., Wirtz Martin, K.M., et al. (2024). N1-methylation of adenosine (m<sup>1</sup>A) in ND5 mRNA leads to complex I dysfunction in Alzheimer's disease. Mol. Psychiatry 29, 1427–1439. https://doi.org/10. 1038/s41380-024-02421-y.
- Sun, H., Li, K., Liu, C., and Yi, C. (2023). Regulation and functions of nonm<sup>6</sup>A mRNA modifications. Nat. Rev. Mol. Cell Biol. 24, 714–731. https:// doi.org/10.1038/s41580-023-00622-x.
- Wang, Q., Zhang, Q., Huang, Y., and Zhang, J. (2020). m<sup>1</sup>A regulator TRMT10C predicts poorer survival and contributes to malignant behavior in gynecological cancers. DNA Cell Biol. 39, 1767–1778. https://doi.org/ 10.1089/dna.2020.5624.
- 95. Gong, W., Xu, J., Wang, Y., Min, Q., Chen, X., Zhang, W., Chen, J., and Zhan, Q. (2022). Nuclear genome-derived circular RNA circPUM1 localizes in mitochondria and regulates oxidative phosphorylation in esophageal squamous cell carcinoma. Signal Transduct. Target. Ther. 7, 40. https://doi.org/10.1038/s41392-021-00865-0.
- 96. Groß, C.J., Mishra, R., Schneider, K.S., Médard, G., Wettmarshausen, J., Dittlein, D.C., Shi, H., Gorka, O., Koenig, P.A., Fromm, S., et al. (2016). K<sup>+</sup> efflux-independent NLRP3 inflammasome activation by small molecules targeting mitochondria. Immunity 45, 761–773. https://doi.org/10.1016/j.immuni.2016.08.010.
- Zhao, Q., Liu, J., Deng, H., Ma, R., Liao, J.Y., Liang, H., Hu, J., Li, J., Guo, Z., Cai, J., et al. (2020). Targeting mitochondria-located circRNA SCAR alleviates NASH via reducing mROS output. Cell 183, 76–93.e22. https://doi.org/10.1016/j.cell.2020.08.009.
- Cernkovich, E.R., Deng, J., Bond, M.C., Combs, T.P., and Harp, J.B. (2008). Adipose-specific disruption of signal transducer and activator of transcription 3 increases body weight and adiposity. Endocrinology 149, 1581–1590. https://doi.org/10.1210/en.2007-1148.
- Zhao, L., Zhang, X., Coday, M., Garcia, D.O., Li, X., Mossavar-Rahmani, Y., Naughton, M.J., Lopez-Pentecost, M., Saquib, N., Shadyab, A.H., et al. (2023). Sugar-sweetened and artificially sweetened beverages and risk of liver cancer and chronic liver disease mortality. JAMA 330, 537–546. https://doi.org/10.1001/jama.2023.12618.
- Hsiao, C.C., Teng, P.H., Wu, Y.J., Shen, Y.W., Mar, G.Y., and Wu, F.Z. (2021). Severe, but not mild to moderate, non-alcoholic fatty liver disease associated with increased risk of subclinical coronary atherosclerosis.
   BMC Cardiovasc. Disord. 21, 244. https://doi.org/10.1186/s12872-021-02060-z.
- 101. Lee, Y.C., Wu, J.S., Yang, Y.C., Chang, C.S., Lu, F.H., and Chang, C.J. (2014). Moderate to severe, but not mild, nonalcoholic fatty liver disease associated with increased risk of gallstone disease. Scand. J. Gastroenterol. 49, 1001–1006. https://doi.org/10.3109/00365521.2014. 920912.

- 102. Liu, M., Kuo, F., Capistrano, K.J., Kang, D., Nixon, B.G., Shi, W., Chou, C., Do, M.H., Stamatiades, E.G., Gao, S., et al. (2020). TGF-β suppresses type 2 immunity to cancer. Nature 587, 115–120. https://doi.org/10.1038/s41586-020-2836-1.
- 103. Shi, X., Chen, Q., and Wang, F. (2019). Mesenchymal stem cells for the treatment of ulcerative colitis: a systematic review and meta-analysis of experimental and clinical studies. Stem Cell Res. Ther. 10, 266. https://doi.org/10.1186/s13287-019-1336-4.
- 104. Wells, G.A., Shea, B., O'Connell, D., Peterson, J., Welch, V., Losos, M., and Tugwell, P. (2014). The Newcastle-Ottawa Scale (NOS) for Assessing the Quality of Nonrandomised Studies in Meta-Analyses. Ottawa Health Research Institute, p. 7. https://www.ohri.ca/programs/clinical\_epidemiology/oxford.asp.
- 105. Elmahdi, R., Lemser, C.E., Thomsen, S.B., Allin, K.H., Agrawal, M., and Jess, T. (2022). Development of cancer among patients with pediatriconset inflammatory bowel disease: a meta-analysis of population-based studies. JAMA Netw. Open 5, e220595. https://doi.org/10.1001/jamanetworkopen.2022.0595.
- 106. Higgins, J.P.T., and Thompson, S.G. (2002). Quantifying heterogeneity in a meta-analysis. Stat. Med. 21, 1539–1558. https://doi.org/10.1002/ sim.1186
- Begg, C.B., and Mazumdar, M. (1994). Operating characteristics of a rank correlation test for publication bias. Biometrics 50, 1088–1101. https://doi.org/10.2307/2533446.
- 108. Luo, X., Li, Z., Chen, L., Zhang, X., Zhu, X., Wang, Z., and Chen, Y. (2023). Monocarboxylate transporter 1 in the liver modulates high-fat diet-induced obesity and hepatic steatosis in mice. Metabolism 143, 155537. https://doi.org/10.1016/j.metabol.2023.155537.
- Boyle, S.T., Faulkner, J.W., McColl, S.R., and Kochetkova, M. (2015). The chemokine receptor CCR6 facilitates the onset of mammary neoplasia in the MMTV-PyMT mouse model via recruitment of tumor-promoting macrophages. Mol. Cancer 14, 115. https://doi.org/10.1186/s12943-015-0394-1.
- 110. Perry, S.W., Schueckler, J.M., Burke, K., Arcuri, G.L., and Brown, E.B. (2013). Stromal matrix metalloprotease-13 knockout alters Collagen I structure at the tumor-host interface and increases lung metastasis of C57BL/6 syngeneic E0771 mammary tumor cells. BMC Cancer 13, 411. https://doi.org/10.1186/1471-2407-13-411.
- 111. Rosenthal, S.B., Liu, X., Ganguly, S., Dhar, D., Pasillas, M.P., Ricciardelli, E., Li, R.Z., Troutman, T.D., Kisseleva, T., Glass, C.K., et al. (2021). Heterogeneity of HSCs in a mouse model of NASH. Hepatology 74, 667–685. https://doi.org/10.1002/hep.31743.
- 112. Leslie, J., Macia, M.G., Luli, S., Worrell, J.C., Reilly, W.J., Paish, H.L., Knox, A., Barksby, B.S., Gee, L.M., Zaki, M.Y.W., et al. (2020). c-Rel orchestrates energy-dependent epithelial and macrophage reprogramming in fibrosis. Nat. Metab. 2, 1350–1367. https://doi.org/10.1038/s42255-020-00306-2.
- 113. Chen, X., Chen, S., Pang, J., Huang, R., You, Y., Zhang, H., Xiao, J., Xue, H., and Ling, W. (2023). Hepatic steatosis aggravates atherosclerosis via small extracellular vesicle-mediated inhibition of cellular cholesterol efflux. J. Hepatol. 79, 1491–1501. https://doi.org/10.1016/j.jhep.2023.08.023.
- 114. Koide, T., Mandai, S., Kitaoka, R., Matsuki, H., Chiga, M., Yamamoto, K., Yoshioka, K., Yagi, Y., Suzuki, S., Fujiki, T., et al. (2023). Circulating extracellular vesicle-propagated microRNA signature as a vascular calcification factor in chronic kidney disease. Circ. Res. 132, 415–431. https://doi.org/10.1161/CIRCRESAHA.122.321939.
- 115. Hu, C.H., Sui, B.D., Liu, J., Dang, L., Chen, J., Zheng, C.X., Shi, S., Zhao, N., Dang, M.Y., He, X.N., et al. (2022). Sympathetic neurostress drives osteoblastic exosomal MiR-21 transfer to disrupt bone homeostasis and promote osteopenia. Small Methods 6, e2100763. https://doi.org/10.1002/smtd.202100763.
- 116. Grivennikov, S.I., Wang, K., Mucida, D., Stewart, C.A., Schnabl, B., Jauch, D., Taniguchi, K., Yu, G.Y., Osterreicher, C.H., Hung, K.E., et al. (2012). Adenoma-linked barrier defects and microbial products drive

# **Article**



- IL-23/IL-17-mediated tumour growth. Nature *491*, 254–258. https://doi.org/10.1038/nature11465.
- 117. Wang, Z., Kim, S.Y., Tu, W., Kim, J., Xu, A., Yang, Y.M., Matsuda, M., Reolizo, L., Tsuchiya, T., Billet, S., et al. (2023). Extracellular vesicles in fatty liver promote a metastatic tumor microenvironment. Cell Metab. 35, 1209–1226.e13. https://doi.org/10.1016/j.cmet.2023.04.013.
- 118. Wu, S., Luo, M., To, K.K.W., Zhang, J., Su, C., Zhang, H., An, S., Wang, F., Chen, D., and Fu, L. (2021). Intercellular transfer of exosomal wild type EGFR triggers osimertinib resistance in non-small cell lung cancer. Mol. Cancer 20, 17. https://doi.org/10.1186/s12943-021-01307-9.
- 119. Liu, X., Lu, Y., Huang, J., Xing, Y., Dai, H., Zhu, L., Li, S., Feng, J., Zhou, B., Li, J., et al. (2022). CD16<sup>+</sup> fibroblasts foster a trastuzumab-refractory microenvironment that is reversed by VAV2 inhibition. Cancer Cell 40, 1341–1357.e13. https://doi.org/10.1016/j.ccell.2022.10.015.
- 120. Merij, L.B., da Silva, L.R., Palhinha, L., Gomes, M.T., Dib, P.R.B., Martins-Gonçalves, R., Toledo-Quiroga, K., Raposo-Nunes, M.A., Andrade, F.B., de Toledo Martins, S., et al. (2024). Density-based lipoprotein depletion improves extracellular vesicle isolation and functional analysis. J. Thromb. Haemost. 22, 1372–1388. https://doi.org/10.1016/j.jtha. 2024.01.010.
- 121. Xiao, L., Duan, R., Liu, W., Zhang, C., Ma, X., Xian, M., Wang, Q., Guo, Q., Xiong, W., Su, P., et al. (2025). Adoptively transferred tumor-specific IL-9-producing cytotoxic CD8<sup>+</sup> T cells activate host CD4<sup>+</sup> T cells to control tumors with antigen loss. Nat. Cancer 6, 718–735. https://doi.org/10.1038/s43018-025-00935-0.
- 122. Wang, H., Franco, F., Tsui, Y.C., Xie, X., Trefny, M.P., Zappasodi, R., Mohmood, S.R., Fernández-García, J., Tsai, C.H., Schulze, I., et al. (2020). CD36-mediated metabolic adaptation supports regulatory T cell survival and function in tumors. Nat. Immunol. 21, 298–308. https://doi.org/10.1038/s41590-019-0589-5.
- 123. Yoon, S., Woo, S.U., Kang, J.H., Kim, K., Kwon, M.H., Park, S., Shin, H.J., Gwak, H.S., and Chwae, Y.J. (2010). STAT3 transcriptional factor activated by reactive oxygen species induces IL6 in starvation-induced autophagy of cancer cells. Autophagy 6, 1125–1138. https://doi.org/10.4161/ auto.6.8.13547.
- 124. Ma, Z., Li, X., Mao, Y., Wei, C., Huang, Z., Li, G., Yin, J., Liang, X., and Liu, Z. (2022). Interferon-dependent SLC14A1(+) cancer-associated fibro-blasts promote cancer stemness via WNT5A in bladder cancer. Cancer Cell 40, 1550–1565.e17. https://doi.org/10.1016/j.ccell.2022.11.005.
- 125. Melo, S.A., Luecke, L.B., Kahlert, C., Fernandez, A.F., Gammon, S.T., Kaye, J., LeBleu, V.S., Mittendorf, E.A., Weitz, J., Rahbari, N., et al. (2015). Glypican-1 identifies cancer exosomes and detects early pancreatic cancer. Nature 523, 177–182. https://doi.org/10.1038/nature14581.
- 126. Liu, M., Bai, J., He, S., Villarreal, R., Hu, D., Zhang, C., Yang, X., Liang, H., Slaga, T.J., Yu, Y., et al. (2014). Grb10 promotes lipolysis and thermogenesis by phosphorylation-dependent feedback inhibition of mTORC1. Cell Metab. 19, 967–980. https://doi.org/10.1016/j.cmet.2014.03.018.
- 127. Rohm, M., Schäfer, M., Laurent, V., Üstünel, B.E., Niopek, K., Algire, C., Hautzinger, O., Sijmonsma, T.P., Zota, A., Medrikova, D., et al. (2016). An AMP-activated protein kinase-stabilizing peptide ameliorates adipose tissue wasting in cancer cachexia in mice. Nat. Med. 22, 1120–1130. https://doi.org/10.1038/nm.4171.

- 128. Shin, H., Ma, Y., Chanturiya, T., Cao, Q., Wang, Y., Kadegowda, A.K.G., Jackson, R., Rumore, D., Xue, B., Shi, H., et al. (2017). Lipolysis in brown adipocytes is not essential for cold-induced thermogenesis in mice. Cell Metab. 26, 764–777.e5. https://doi.org/10.1016/j.cmet.2017.09.002.
- 129. Kalfeist, L., Petit, S., Galland, L., Ghiringhelli, F., Ladoire, S., and Limagne, E. (2023). Simultaneous isolation of CD45 tumor-infiltrating lymphocytes, tumor cells, and associated fibroblasts from murine breast tumor model by MACS. Star Protoc. 4, 101951. https://doi.org/10.1016/j. xpro.2022.101951.
- 130. Nakai, K., Lin, H., Yamano, S., Tanaka, S., Kitamoto, S., Saitoh, H., Sakuma, K., Kurauchi, J., Akter, E., Konno, M., et al. (2023). Wnt activation disturbs cell competition and causes diffuse invasion of transformed cells through NF-κB-MMP21 pathway. Nat. Commun. 14, 7048. https://doi.org/10.1038/s41467-023-42774-6.
- 131. Wang, W., Wang, L., Lu, J., Siedlak, S.L., Fujioka, H., Liang, J., Jiang, S., Ma, X., Jiang, Z., da Rocha, E.L., et al. (2016). The inhibition of TDP-43 mitochondrial localization blocks its neuronal toxicity. Nat. Med. 22, 869–878. https://doi.org/10.1038/nm.4130.
- 132. Dorado, E., Doria, M.L., Nagelkerke, A., McKenzie, J.S., Maneta-Stavrakaki, S., Whittaker, T.E., Nicholson, J.K., Coombes, R.C., Stevens, M.M., and Takats, Z. (2024). Extracellular vesicles as a promising source of lipid biomarkers for breast cancer detection in blood plasma. J. Extracell. Vesicles 13, e12419. https://doi.org/10.1002/jev2.12419.
- 133. Montgomery, M.K., Bayliss, J., Nie, S., De Nardo, W., Keenan, S.N., Miotto, P.M., Karimkhanloo, H., Huang, C., Schittenhelm, R.B., Don, A. S., et al. (2022). Deep proteomic profiling unveils arylsulfatase A as a non-alcoholic steatohepatitis inducible hepatokine and regulator of glycemic control. Nat. Commun. 13, 1259. https://doi.org/10.1038/s41467-022-28889-2.
- 134. Liu, Y., Zhou, J., Li, X., Zhang, X., Shi, J., Wang, X., Li, H., Miao, S., Chen, H., He, X., et al. (2022). tRNA-m<sup>1</sup>A modification promotes T cell expansion via efficient MYC protein synthesis. Nat. Immunol. 23, 1433–1444. https://doi.org/10.1038/s41590-022-01301-3.
- 135. Zhang, L.S., Xiong, Q.P., Peña Perez, S., Liu, C., Wei, J., Le, C., Zhang, L., Harada, B.T., Dai, Q., Feng, X., et al. (2021). ALKBH7-mediated demethylation regulates mitochondrial polycistronic RNA processing. Nat. Cell Biol. 23, 684–691. https://doi.org/10.1038/s41556-021-00709-7.
- 136. Lv, K., Gong, C., Antony, C., Han, X., Ren, J.G., Donaghy, R., Cheng, Y., Pellegrino, S., Warren, A.J., Paralkar, V.R., et al. (2021). HectD1 controls hematopoietic stem cell regeneration by coordinating ribosome assembly and protein synthesis. Cell Stem Cell 28, 1275–1290.e9. https://doi.org/10.1016/j.stem.2021.02.008.
- 137. Zheng, Y., Chen, J., Macwan, V., Dixon, C.L., Li, X., Liu, S., Yu, Y., Xu, P., Sun, Q., Hu, Q., et al. (2024). S-acylation of ATGL is required for lipid droplet homoeostasis in hepatocytes. Nat. Metab. 6, 1549–1565. https://doi.org/10.1038/s42255-024-01085-w.
- 138. Basu, D., Manjur, J., and Jin, W. (2011). Determination of lipoprotein lipase activity using a novel fluorescent lipase assay. J. Lipid Res. 52, 826–832. https://doi.org/10.1194/jlr.D010744.





# **STAR**\*METHODS

# **KEY RESOURCES TABLE**

REAGENT or RESOURCE	SOURCE	IDENTIFIER
Antibodies		
Rabbit anti-mouse CD81	Abcam	Cat#ab109201; RRID: AB_10866464
Rabbit anti-mouse ALIX	Proteintech	Cat#12422-1-AP; RRID: AB_2162467
Rabbit anti-mouse ARF6	Proteintech	Cat#20225-1-AP; RRID: AB_10646481
Rabbit-anti-mouse calnexin	Proteintech	Cat#10427-2-AP; RRID: AB_2069033
Rabbit anti-mouse ErbB4	Proteintech	Cat#19943-1-AP; RRID: AB_10646486
Rabbit anti-mouse Nrg1	Proteintech	Cat#10527-1-AP; RRID: AB_2154659
Rabbit anti-mouse Nrg2	GeneTex	Cat#GTX12019
Rabbit anti-mouse Nrg3	Abcam	Cat#ab109256; RRID: AB_10864403
Rabbit anti-mouse Nrg4	GeneTex	Cat#GTX64845
Rabbit anti-mouse FATP1	Affinity Biosciences	Cat#DF7716; RRID: AB_2841185
Rabbit anti-mouse FATP4	Proteintech	Cat#11013-1-AP; RRID: AB_2190637
Rabbit anti-mouse TRMT10C	Proteintech	Cat#29087-1-AP; RRID: AB_2881239
Rabbit anti-mouse RPS16	Abcam	Cat#ab177951
Rabbit anti-mouse MRPS5	Thermo Fisher Scientific	Cat#PA5-75889; RRID: AB_2719617
Rabbit anti-mouse MT-ND6	Affinity Biosciences	Cat#DF9676; RRID: AB_2842872
Rabbit anti-mouse MT-ND5	Proteintech	Cat#55410-1-AP; RRID: AB_2881324
Rabbit anti-mouse CGI-58	Immunoway	Cat#YN4673
Nouse anti-mouse VDAC1	Proteintech	Cat#66345-1-lg; RRID: AB_2881725
Horseradish peroxidase (HRP)-Conjugated α-Tubulin	Proteintech	Cat#HRP-66031; RRID: AB_2687491
IRP-Conjugated GAPDH Antibody	Proteintech	Cat#HRP-60004; RRID: AB_2737588
HRP-linked anti-rabbit antibody	Cell Signaling Technology	Cat#7074; RRID: AB_2099233
IRP-linked anti-mouse antibody	Cell Signaling Technology	Cat#7076; RRID: AB_330924
Rabbit anti-mouse ErbB4	Cell Signaling Technology	Cat#4795T; RRID: AB_2099883
Brilliant Violet 421 anti-mouse CD31 Antibody	Biolegend	Cat#102423; RRID: AB_2650892
Brilliant Violet 421 Rat IgG2a, κ Isotype Ctrl Antibody	Biolegend	Cat#400535; RRID: AB_10933427
APC anti-mouse CD326 (Ep-CAM) Antibody	Biolegend	Cat#118213; RRID: AB_1134105
PC Rat IgG2a, κ Isotype Ctrl Antibody	Biolegend	Cat#400512; RRID: AB_2814702
lexa Fluor 700 anti-mouse CD45 Antibody	Biolegend	Cat#103127; RRID: AB_493715
Alexa Fluor 700 Rat IgG2b, κ Isotype Ctrl Antibody	Biolegend	Cat#400628; RRID: AB_493783
Brilliant Violet 510 anti-mouse CD45	Biolegend	Cat#103137; RRID: AB_2561392
Brilliant Violet 510-conjugated Rat IgG2b, κ Isotype Ctrl Antibody	Biolegend	Cat#400645; RRID: AB_3097656
PE/Cyanine7 anti-mouse CD3ε Antibody	Biolegend	Cat#100319; RRID: AB 312684
PE/Cyanine7 Armenian Hamster IgG	Biolegend	Cat#400921; RRID: AB_2905473
sotype Ctrl Antibody	- 3	
APC anti-mouse CD4	Biolegend	Cat#100515; RRID: AB_312718
PC-conjugated Rat IgG2a, κ Isotype Ctrl Antibody	Biolegend	Cat#400511; RRID: AB_2814702
ITC anti-mouse CD8a	Biolegend	Cat#100705; RRID: AB_312744
ITC-conjugated Rat IgG2a, κ Isotype Ctrl Antibody	Biolegend	Cat#400505; RRID: AB_2736919
lexa Fluor 488 anti-Vimentin Antibody	Biolegend	Cat#699305; RRID: AB_2888889
Nexa Fluor 488 Rat IgG2a, κ Isotype Ctrl Antibody	Biolegend	Cat#400525; RRID: AB_2864283
PE anti-mouse Foxp3	Biolegend	Cat#320007; RRID: AB_492981
PE-conjugated Mouse IgG1, κ Isotype Ctrl (ICFC) Antibody	Biolegend	Cat#400139; RRID: AB_493443
Rabbit anti-mouse Perilipin 1	9	,

# **Article**



Continued		
REAGENT or RESOURCE	SOURCE	IDENTIFIER
Rabbit anti-mouse ASC-1	GeneTex	Cat#GTX47874; RRID: AB_11168468
Rabbit anti-mouse CD31	Abcam	Cat#ab222783; RRID: AB_2905525
Rabbit anti-mouse Cytokeratin 8	Abcam	Cat# ab53280; RRID: AB_869901
Rat anti-mouse CD45	Abcam	Cat#ab23910; RRID: AB_447758
Nouse anti-mouse Vimentin	Abcam	Cat#ab20346; RRID: AB_445527
labbit anti-mouse Tom20	Proteintech	Cat#CL488-11802; RRID: AB_2919040
sotype control IgG antibody	Proteintech	Cat#98136-1-RR; RRID: AB_3672282
lexa Fluor 488-conjugated donkey anti-rabbit IgG	Thermo Fisher Scientific	Cat#A21206; RRID: AB_2535792
lexa Fluor 488-conjugated donkey anti-rat IgG	Thermo Fisher Scientific	Cat#A21208; RRID: AB_2535794
lexa Fluor 488-conjugated donkey anti-mouse IgG	Thermo Fisher Scientific	Cat#A21202; RRID: AB_141607
lexa Fluor 555-conjugated donkey anti-rabbit IgG	Thermo Fisher Scientific	Cat#A31572; RRID: AB_162543
lexa Fluor 647-conjugated donkey anti-rabbit IgG	Thermo Fisher Scientific	Cat#A31573; RRID: AB_2536183
nti-rabbit horseradish peroxidase HRP)-conjugated secondary antibody	Panovue	Cat#10015001030
ruStain FcX PLUS (anti-mouse CD16/32) Antibody	Biolegend	Cat#156603; RRID: AB_2783137
nti-mouse ErbB4 antibody	BioVision	Cat#A1047
nVivoMAb mouse IgG1 isotype control	Bioxcell	Cat#BE0083; RRID: AB_1107784
Goat anti-rabbit IgG (10nm Gold, 10 OD)	Abcam	Cat#ab270555
Mouse anti-mouse ErbB4	Santa Cruz Biotechnology	Cat#sc-8050; RRID: AB_627250
Rabbit anti-1-methyladenosine (m <sup>1</sup> A) antibody	Abcam	Cat#ab208196
acterial and virus strains		
entiV_Cas9_puro	Addgene	RRID: Addgene_108100
tiological samples	•	<u> </u>
Plasma samples of patients (used for	Sun Yat-Sen Memorial Hospital,	N/A
xosome flow cytometry analysis)	Sun Yat-Sen University	
	•	1971
hemicals, peptides, and recombinant proteins	•	Cat#11875093
chemicals, peptides, and recombinant proteins	Sun Yat-Sen University	
Chemicals, peptides, and recombinant proteins RIPM 1640 retal bovine serum (FBS)	Sun Yat-Sen University Gibco	Cat#11875093
Chemicals, peptides, and recombinant proteins RIPM 1640 (etal bovine serum (FBS) DMEM Oulbecco' modified Eagle's medium (DMEM)/F12	Sun Yat-Sen University  Gibco  Gibco	Cat#11875093 Cat#10099-141
chemicals, peptides, and recombinant proteins IPM 1640 etal bovine serum (FBS) IMEM Oulbecco' modified Eagle's medium (DMEM)/F12 nedium with glutamine and Hepes	Gibco Gibco Gibco	Cat#11875093 Cat#10099-141 Cat#11995065
chemicals, peptides, and recombinant proteins IIPM 1640 etal bovine serum (FBS) IMEM Pulbecco' modified Eagle's medium (DMEM)/F12 nedium with glutamine and Hepes Iodium palmitate (PA powder)	Gibco Gibco Gibco HyCyte	Cat#11875093 Cat#10099-141 Cat#11995065 Cat#TCM-G709
chemicals, peptides, and recombinant proteins al PM 1640 etal bovine serum (FBS) amelia MEM bulbecco' modified Eagle's medium (DMEM)/F12 nedium with glutamine and Hepes codium palmitate (PA powder) codium hydroxide (NaOH)	Gibco Gibco Gibco HyCyte Sigma-Aldrich	Cat#11875093 Cat#10099-141 Cat#11995065 Cat#TCM-G709 Cat#P9767
chemicals, peptides, and recombinant proteins clPM 1640 etal bovine serum (FBS) etal bovine serum (FBS	Gibco Gibco Gibco HyCyte Sigma-Aldrich Sigma-Aldrich	Cat#11875093 Cat#10099-141 Cat#11995065 Cat#TCM-G709 Cat#P9767 Cat#795429
chemicals, peptides, and recombinant proteins IPM 1640 etal bovine serum (FBS) IMEM Fullbecco' modified Eagle's medium (DMEM)/F12 nedium with glutamine and Hepes odium palmitate (PA powder) odium hydroxide (NaOH) farmine Alum shaled isoflurane	Gibco Gibco Gibco HyCyte  Sigma-Aldrich Sigma-Aldrich Stem Cell Technologies	Cat#11875093 Cat#10099-141 Cat#11995065 Cat#TCM-G709 Cat#P9767 Cat#795429 Cat#07070
Chemicals, peptides, and recombinant proteins RIPM 1640 Setal bovine serum (FBS) SMEM Sulbecco' modified Eagle's medium (DMEM)/F12 medium with glutamine and Hepes sodium palmitate (PA powder) Sodium hydroxide (NaOH) Carmine Alum shaled isoflurane Suprenorphine hydrochloride	Gibco Gibco Gibco Gibco HyCyte  Sigma-Aldrich Sigma-Aldrich Stem Cell Technologies RWD life science	Cat#11875093 Cat#10099-141 Cat#11995065 Cat#TCM-G709  Cat#P9767 Cat#795429 Cat#07070 Cat#R510-22
Chemicals, peptides, and recombinant proteins RIPM 1640 Petal bovine serum (FBS) PMEM Pulbecco' modified Eagle's medium (DMEM)/F12 Puedium with glutamine and Hepes Podium palmitate (PA powder) Podium hydroxide (NaOH) Poarmine Alum Published isoflurane Pouprenorphine hydrochloride Reparin sodium	Gibco Gibco Gibco Gibco HyCyte  Sigma-Aldrich Sigma-Aldrich Stem Cell Technologies RWD life science Sigma-Aldrich	Cat#11875093 Cat#10099-141 Cat#11995065 Cat#TCM-G709  Cat#P9767 Cat#795429 Cat#07070 Cat#R510-22 Cat#B-044S-1ML
chemicals, peptides, and recombinant proteins at IPM 1640 etal bovine serum (FBS) at IPM 1640 etal bovine serum (DMEM)/F12 etal bovine serum (FBS) etal bovi	Gibco Gibco Gibco Gibco HyCyte  Sigma-Aldrich Sigma-Aldrich Stem Cell Technologies RWD life science Sigma-Aldrich Sigma-Aldrich	Cat#11875093 Cat#10099-141 Cat#11995065 Cat#TCM-G709  Cat#P9767 Cat#795429 Cat#07070 Cat#R510-22 Cat#B-044S-1ML Cat#PHR8927
chemicals, peptides, and recombinant proteins cliPM 1640 etal bovine serum (FBS) etal bovine serum (DMEM)/F12 etal bovine serum (DMEM	Gibco Gibco Gibco Gibco HyCyte  Sigma-Aldrich Sigma-Aldrich Stem Cell Technologies RWD life science Sigma-Aldrich Sigma-Aldrich Macklin	Cat#11875093 Cat#10099-141 Cat#11995065 Cat#TCM-G709  Cat#P9767 Cat#795429 Cat#07070 Cat#R510-22 Cat#B-044S-1ML Cat#PHR8927 Cat#C877598
hemicals, peptides, and recombinant proteins  IPM 1640 etal bovine serum (FBS)  MEM ulbecco' modified Eagle's medium (DMEM)/F12 hedium with glutamine and Hepes odium palmitate (PA powder) odium hydroxide (NaOH) farmine Alum shaled isoflurane uprenorphine hydrochloride feparin sodium leftriaxone ermount Mounting Medium ank's balanced salt solution (HBSS)	Gibco Gibco Gibco Gibco HyCyte  Sigma-Aldrich Sigma-Aldrich Stem Cell Technologies RWD life science Sigma-Aldrich Sigma-Aldrich Sigma-Aldrich Sigma-Ficence Sigma-Company of the science	Cat#11875093 Cat#10099-141 Cat#11995065 Cat#TCM-G709  Cat#P9767 Cat#795429 Cat#07070 Cat#R510-22 Cat#B-044S-1ML Cat#PHR8927 Cat#C877598 Cat#WG10004160
chemicals, peptides, and recombinant proteins IPM 1640 etal bovine serum (FBS) MEM ullbecco' modified Eagle's medium (DMEM)/F12 dedium with glutamine and Hepes odium palmitate (PA powder) odium hydroxide (NaOH) darmine Alum delaled isoflurane uprenorphine hydrochloride eparin sodium deftriaxone ermount Mounting Medium ank's balanced salt solution (HBSS) EPES	Gibco Gibco Gibco Gibco HyCyte  Sigma-Aldrich Sigma-Aldrich Stem Cell Technologies RWD life science Sigma-Aldrich Sigma-Aldrich Sigma-Aldrich Sigma-Cell Technologies Gibco	Cat#11875093 Cat#10099-141 Cat#11995065 Cat#TCM-G709  Cat#P9767 Cat#795429 Cat#07070 Cat#R510-22 Cat#B-044S-1ML Cat#PHR8927 Cat#C877598 Cat#WG10004160 Cat#C14175500BT
chemicals, peptides, and recombinant proteins chemicals peptides, and recombinant proteins chemicals, peptides, peptides, and recombinant proteins chemicals, peptides, pe	Gibco Gibco Gibco Gibco HyCyte  Sigma-Aldrich Sigma-Aldrich Stem Cell Technologies RWD life science Sigma-Aldrich Sigma-Aldrich Sigma-Fildrich Sigma-Colored	Cat#11875093 Cat#10099-141 Cat#11995065 Cat#TCM-G709  Cat#P9767 Cat#795429 Cat#07070 Cat#R510-22 Cat#B-044S-1ML Cat#PHR8927 Cat#C877598 Cat#WG10004160 Cat#C14175500BT Cat#15630080
chemicals, peptides, and recombinant proteins chemicals peptides, and recombinant proteins chemicals, peptides, and recombinant proteins collagenase peptides, and recombinant proteins chemicals, peptides, peptides, and recombinant proteins chemicals, peptides, p	Gibco Gibco Gibco Gibco HyCyte  Sigma-Aldrich Sigma-Aldrich Stem Cell Technologies RWD life science Sigma-Aldrich Sigma-Aldrich Sigma-Aldrich Gibco Gibco Gibco Sigma-Aldrich	Cat#11875093 Cat#10099-141 Cat#11995065 Cat#TCM-G709  Cat#P9767 Cat#795429 Cat#07070 Cat#R510-22 Cat#B-044S-1ML Cat#PHR8927 Cat#C877598 Cat#WG10004160 Cat#C14175500BT Cat#P5147
Chemicals, peptides, and recombinant proteins RIPM 1640 Fetal bovine serum (FBS) DMEM Dulbecco' modified Eagle's medium (DMEM)/F12 Inedium with glutamine and Hepes Bodium palmitate (PA powder) Bodium hydroxide (NaOH) Carmine Alum Inhaled isoflurane Buprenorphine hydrochloride Reparin sodium Ceftriaxone Permount Mounting Medium Rank's balanced salt solution (HBSS) REPES Protease from Streptomyces griseus Collagenase D DD45 MicroBeads, mouse	Gibco Gibco Gibco Gibco HyCyte  Sigma-Aldrich Sigma-Aldrich Stem Cell Technologies RWD life science Sigma-Aldrich Sigma-Aldrich Sigma-Aldrich Gibco Gibco Gibco Gibco Sigma-Aldrich Roche	Cat#11875093 Cat#10099-141 Cat#11995065 Cat#7CM-G709  Cat#P9767 Cat#795429 Cat#07070 Cat#R510-22 Cat#B-044S-1ML Cat#PHR8927 Cat#C877598 Cat#WG10004160 Cat#C14175500BT Cat#P5147 Cat#P5147 Cat#11088866001
Accessome flow cytometry analysis) Chemicals, peptides, and recombinant proteins RIPM 1640 Fetal bovine serum (FBS) Chemicals peptides, and recombinant proteins RIPM 1640 Fetal bovine serum (FBS) Chemicals peptides and recombinant proteins RIPM 1640 Fetal bovine serum (FBS) Chemicals peptides and recombinant proteins RIPM 1640 Fetal bovine serum (FBS) Chemicals peptides and recombinant proteins Ripm 1640 Fetal bovine serum (FBS) Chemicals peptides and recombinant proteins Ripm 1640 Fetal bovine serum (FBS) Ripm 1640 Fetal bovine serum	Gibco Gibco Gibco Gibco HyCyte  Sigma-Aldrich Sigma-Aldrich Stem Cell Technologies RWD life science Sigma-Aldrich Sigma-Aldrich Sigma-Aldrich Gibco Gibco Gibco Gibco Sigma-Aldrich Roche Miltenyi Biotec	Cat#11875093 Cat#10099-141 Cat#11995065 Cat#7CM-G709  Cat#P9767 Cat#795429 Cat#07070 Cat#R510-22 Cat#B-044S-1ML Cat#PHR8927 Cat#C877598 Cat#WG10004160 Cat#C14175500BT Cat#15630080 Cat#P5147 Cat#11088866001 Cat#130052301
Chemicals, peptides, and recombinant proteins RIPM 1640 Petal bovine serum (FBS) PMEM Pulbecco' modified Eagle's medium (DMEM)/F12 Predium with glutamine and Hepes Rodium palmitate (PA powder) Rodium hydroxide (NaOH) Parmine Alum Panaled isoflurane Repernorphine hydrochloride Reparin sodium Petriaxone Permount Mounting Medium Rank's balanced salt solution (HBSS) RIEPES Protease from Streptomyces griseus Rodlagenase D RD45 MicroBeads, mouse RIPM 1640 REPS ROD166 REPS ROD176 REPS ROD	Gibco Gibco Gibco Gibco HyCyte  Sigma-Aldrich Sigma-Aldrich Stem Cell Technologies RWD life science Sigma-Aldrich Sigma-Aldrich Gibco Gibco Gibco Gibco Gibco Sigma-Aldrich Roche Miltenyi Biotec Miltenyi Biotec Miltenyi Biotec	Cat#11875093 Cat#10099-141 Cat#11995065 Cat#TCM-G709  Cat#P9767 Cat#795429 Cat#07070 Cat#R510-22 Cat#B-044S-1ML Cat#PHR8927 Cat#C877598 Cat#WG10004160 Cat#C14175500BT Cat#15630080 Cat#P5147 Cat#11088866001 Cat#130052301 Cat#130092007
Chemicals, peptides, and recombinant proteins RIPM 1640 Petal bovine serum (FBS) PMEM Pulbecco' modified Eagle's medium (DMEM)/F12 Puedium with glutamine and Hepes Podium palmitate (PA powder) Podium palmitate (PA powder) Podium hydroxide (NaOH) Poarmine Alum Pulaled isoflurane Pouprenorphine hydrochloride Peterparin sodium Petertriaxone Permount Mounting Medium Plank's balanced salt solution (HBSS) PEPES Protease from Streptomyces griseus Pollagenase D	Gibco Gibco Gibco Gibco HyCyte  Sigma-Aldrich Sigma-Aldrich Stem Cell Technologies RWD life science Sigma-Aldrich Sigma-Aldrich Sigma-Aldrich Gibco Gibco Gibco Gibco Sigma-Aldrich Roche Miltenyi Biotec Miltenyi Biotec	Cat#11875093 Cat#10099-141 Cat#11995065 Cat#TCM-G709  Cat#P9767 Cat#795429 Cat#07070 Cat#8510-22 Cat#B-044S-1ML Cat#PHR8927 Cat#C877598 Cat#WG10004160 Cat#C14175500BT Cat#15630080 Cat#P5147 Cat#11088866001 Cat#130052301 Cat#130092007 Cat#130105958



# **Cell Metabolism**Article

Continued		
REAGENT or RESOURCE	SOURCE	IDENTIFIER
Gey's balanced salt solution B (GBSS-B)	Sigma-Aldrich	Cat#G9779
Nycodenz	Accurate Chemical	Cat#AN1002424
Gelling agarose	Sigma-Aldrich	Cat#A9414
GW4869	MedChemExpress	Cat#HY-19363
Dimethylamiloride (DMA)	MedChemExpress	Cat#HY-138866
1,1'-dioctadecyl-3,3,3', 3'-tetramethylindocarbocyanine perchlorate (Dil) membrane dye	Thermo Fisher Scientific	Cat#D3911
Tissue-Tek O.C.T. Compound	Sakura Finetek	Cat#4583
RIPA lysis buffer	Thermo Fisher Scientific	Cat#89900
Protease Inhibitor Cocktail	Thermo Fisher Scientific	Cat#78440
NuPAGE LDS-Sample buffer (4×)	Thermo Fisher Scientific	Cat#NP0008
Bovine serum albumin (BSA)	Asegene	Cat#43035
SuperSignal West Femto Maximum Sensitivity Substrate	Thermo Fisher Scientific	Cat#34095
SuperSignal West Pico PLUS Chemiluminescent Substrate	Thermo Fisher Scientific	Cat#34580
FM1-43FX dye	Thermo Fisher Scientific	Cat#F35355
Collagenase type I	Biofroxx	Cat#1904GR001
DNase I	Roche	Cat#10104159001
RBC Lysis Buffer (10X)	Biolegend	Cat#420301
40% Percoll	GE Healthcare	Cat#170891
BD Horizon Fixable Viability Stain 780	BD Biosciences	Cat#565388
4,4-difluoro-1,3,5,7,8-pentamethyl-4-bora-3a, 4a-diaza-s-indacene (BODIPY 493/503)	Invitrogen	Cat#D3922
2', 7'-Dichlorodihydrofluorescein diacetate (H2-DCFDA) dye	MedChemExpress	Cat#HY-D0940
DAPI	Beyotime	Cat#C1006
ProLong Diamond Antifade Mountant	Thermo Fisher Scientific	Cat#P36970
Dithiothreitol (DTT)	Sigma-Aldrich	Cat#43816
Iodoacetamide (IAA)	Sigma-Aldrich	Cat#A3221
Acetonitrile (ACN)	Sigma-Aldrich	Cat#271004
Trypsin	Promega	Cat#V5280
Lipofectamine RNAiMAX	Invitrogen	Cat#13778030
Opti-MEM I Reduced Serum Medium	Gibco	Cat#31985070
Aldehyde/Sulfate Latex Beads	Invitrogen	Cat#A37304
Polybrene	Sigma-Aldrich	Cat#TR-1003
Puromycin	MedChemExpress	Cat#HY-B1743A
Atglistatin	MedChemExpress	Cat#HY-15859
TRizol Reagent	Invitrogen	Cat#15596026CN
TB Green Premix Ex Taq II (Tli RNaseH Plus)	Takara	Cat#RR820A
Cell counting kit-8 (CCK-8)	APEXBIO	Cat#CCK8-K1018-5
S1 nuclease	Takara	Cat#2410A
Alkaline phosphatase	Takara	Cat#2250A
Phosphodiesterase I	Sigma-Aldrich	Cat#P3243
RNase inhibitor	APExBIO	Cat#K1046
Pierce Protein A/G beads	Thermo Fisher Scientific  APExBIO	Cat#88802
Proteinase K		Cat#K1037
Chloramphenicol	Sigma-Aldrich	Cat#C0378
Cycloheximide	Sigma-Aldrich	Cat#239765

# **Article**



Continued		
REAGENT or RESOURCE	SOURCE	IDENTIFIER
Micrococcal nuclease	Beyotime	Cat#D7201S
SUPERase In RNase inhibitor	Invitrogen	Cat#AM2696
EnzChek lipase substrate	Thermo Fisher Scientific	Cat#E33955
Zwittergent 3-18	Sangon Biotech	Cat#A600556-0001
Critical commercial assays		
LabAssay NEFA	Wako	Cat#294-63601
Mouse insulin Enzyme-linked	Elabscience	Cat#E-EL-M1382
immunosorbent assay (ELISA) kit		
Pierce BCA protein assay kit	Thermo Fisher Scientific	Cat#23227
SPI-Pon 812R Embedding Kit	SPI Supplies	Cat#02660R-AB
Intracellular Fixation and Permeabilization kit	eBioscience	Cat#88-8824-00
PANO4-plex MIF Kit	Panovue	Cat#0079100020
Pierce quantitative colorimetric peptide assay	Thermo Fisher Scientific	Cat#23275
Mouse ErbB4 ELISA kit	Abebio	Cat#AE45297MO
Mouse TRMT10C ELISA kit	Abebio	Cat#AE22369MO
3T3-L1 Adipogenic Differentiation Kit	HyCyte	Cat#EFMX-D102R
Hifair III 1st Strand cDNA Synthesis Kit	YEASEN	Cat#11141ES60
Mitochondria Isolation Kit	Thermo Fisher Scientific	Cat#89874
Hieff NGS mRNA Isolation Master Kit	Yeasen	Cat#12603ES24
mirVana miRNA Isolation Kit	Invitrogen	Cat#AM1561
Deposited data		
Gene expression data of Nrg1, Nrg2, Nrg3 and Nrg4	Gene database	Gene: 211323, 100042150, 18183, 83961
Proteomics data	This paper	PRIDE: PXD067453
Experimental models: Cell lines		
Mouse: EO771 cells	ATCC	CRL-3461; RRID: CVCL_GR23
Mouse: AML12 cells	ATCC	CRL-2254; RRID: CVCL_0140
Mouse: 3T3-L1 cells	ATCC	CL-173; RRID: CVCL_0123
Experimental models: Organisms/strains		
Mouse: C57BL/6	Animal Experiment Center of Sun-Yat-Sen University	N/A
Mouse: B6.FVB-Tg(MMTV-PyVT)634Mul/LellJ	The Jackson Laboratory	Cat#022974; RRID: IMSR_JAX:022974
Mouse: B6.FVB-Tg(Adipoq-cre)1Evdr/J	The Jackson Laboratory	Cat#028020; RRID: IMSR_JAX:028020
Mouse: Nrg4 <sup>flox/flox</sup>	Shanghai Model Organisms Center, Inc	N/A
Mouse: Apc-L850X	Shanghai Model Organisms Center, Inc	Cat#NM-KI-200001; RRID: IMSR_NM-KI-200001
Oligonucleotides		
PCR primers, see Table S9	This paper	N/A
sgRNAs and siRNAs targeting sequences, see Table S9	This paper	N/A
Software and algorithms		
X-tile	N/A	N/A
Review Manager (RevMan) Version 5.4. Copenhagen	Cochrane training	https://training.cochrane.org/online-learning/core-software/revman
ImageJ	NIH	https://imagej.nih.gov/ij/
Nanoparticle Tracking Analysis (NTA) analytical software v3.0	Malvern Instruments	https://www.malvernpanalytical.com/ en/support/product-support/software/ nanosight-nta-software-update-v3-4-4
Living Image software v.3.0	Caliper Life Sciences	https://www.perkinelmer.com.cn/
		(Continued on next pag



Continued		
REAGENT or RESOURCE	SOURCE	IDENTIFIER
FlowJo	Treestar	https://www.flowjo.com/solutions/flowjo
Leica software	Leica Microsystems	https://www.leica-microsystems.com/ products/microscope-software/p/ leica-las-x-ls/downloads/
Analyst 1.6.3	Sciex	https://www.sciex.com.cn/products/ software/analyst-software
Wave software	Agilent Technologies	https://www.agilent.com.cn/zh-cn/ product/cell-analysis/real-time-cell- metabolic-analysis/xf-software/ seahorse-wave-desktop- software-740897
Prism 9.0	GraphPad Software	https://www.graphpad.com/
R v4.4.3	N/A	https://www.r-project.org/
BioRender	N/A	https://www.biorender.com/
Other		
High fructose diet (HFrD)	Teklad	Cat#89247
High fat diet (HFD)	Research Diets	Cat#D12492
Amicon Ultra-15 centrifugal filters with 10 kDa cutoff	Millipore	Cat#UFC901024
Polyvinylidene difluoride (PVDF) membranes	Roche	Cat#03010040001
Amicon Ultra 10K centrifugal filter tube	Merck Millipore	Cat#UFC901008
Transwell 6 well plates	Corning	Cat#3412
Oasis HLB 1 cc Vac Cartridge	Waters	Cat#186000383
LS Separation columns	Miltenyi Biotec	Cat#130-042-401
96-well 0.4-μm transwell system	Corning	Cat#3381
96-well opaque black plates	Corning	Cat#3915

### **EXPERIMENTAL MODEL AND SUBJECT DETAILS**

# **Patients and plasma samples**

To investigate the risk of breast cancer development in patients with NAFLD with who have breast atypical hyperplasia, a total of 357 female patients aged 18-85 years, who were diagnosed with atypical hyperplasia after surgical excision of breast lesions between January 2014 and December 2022 at the Sun Yat-Sen Memorial Hospital, Sun Yat-Sen University (Guangzhou, China), were included in this study. Patients who had been diagnosed with breast cancer, lobular carcinoma in situ, or contralateral breast cancer either before, at the time of, or within six months following surgical excision were excluded. HR and 95% CIs for breast cancer incidence were estimated using Cox proportional hazard regression models.<sup>99</sup>

Patient survival analysis was performed on two cohorts of female patients with invasive breast carcinoma (stage I-III). For survival analysis comparing patients with NAFLD and those without NAFLD, a total of 3,781 patients aged 18-85 who received breast surgery at the Sun Yat-Sen Memorial Hospital between January 2012 to December 2022 were included. Among these patients, there were 942 patients diagnosed with NAFLD. For survival analysis stratified by the fasting plasma glucose (FPG) levels, morning collections of patient blood samples were performed subsequent to a fast lasting no less than 10 hr. FPG values of all 3,781 participants were categorized into three groups according to the 2006 WHO criteria: normal fasting glucose (less than 6.1 mmol/L), impaired fasting glucose (ranging from 6.1 to 6.9 mmol/L) or diabetes (FPG of 7.0 mmol/L or higher). FPG values of all 3,781 participants with high levels of ErbB4+ circulating exosomes (crExos) and those with low levels, another cohort was included, comprising 3,013 patients who had breast surgery at Sun Yat-Sen Memorial Hospital between January 2019 and December 2023. Plasma samples were obtained from all patients in this cohort. In this cohort, 731 patients were diagnosed with NAFLD. The optimum cutoff point (61.8%) for categorizing patients into high and low ErbB4+ crExos group was identified by a minimal p-value approach using X-Tile statistical software, and the Kaplan-Meier method was applied to analyze survival data.

For all patients, data from abdominal ultrasound examinations, which were performed at the time of diagnosis of breast atypical hyperplasia or breast cancer, were collected. The diagnosis and severity of NAFLD were assessed via the abdominal ultrasonography performed by experienced clinical radiologists at Sun Yat-Sen Memorial Hospital as previously described.<sup>7,100</sup> Ultrasonographic signs of hepatic steatosis included bright parenchyma, liver-to-kidney contrast, deep beam attenuation, and bright vessel walls. Patients considered for NAFLD were verified for the absence of any of the following other possible causes of chronic liver disease: (1) being positive for hepatitis B surface antigen or antibodies against the hepatitis C virus; (2) consuming a significant amount of alcohol

# **Cell Metabolism**

# **Article**



(defined as more than 20 g per day); (3) having previous used of medications linked to fatty liver disease, including tamoxifen, methotrexate, or amiodarone; and (4) other recognized causes of chronic liver disease. The severity of NAFLD was classified into mild, moderate, and severe grades. Mild NAFLD is defined by s slight rise in liver echogenicity, mild weakening of ultrasound signal penetration, and a slight reduction in the clarity of intrahepatic vessel walls and diaphragm borders. Moderate NAFLD is characterized by a diffuse increase of liver echogenicity, more significant attenuation of ultrasound signal penetration, and reduced visibility of intrahepatic vessel walls—especially the peripheral branches. Severe NAFLD involves a marked increase of liver echogenicity, significant reduction in ultrasound signal penetration, and poor or absent visualization of intrahepatic vessel walls and diaphragm. <sup>100,101</sup> According to the World Health Organization's guidelines for populations in the Asia-Pacific region, obesity is defined by a body mass index (BMI) of 25 kg/m² or greater. <sup>22</sup>

All samples were collected from patients with informed consent, and all relevant procedures were conducted with the approval of the internal review and ethics boards of Sun Yat-Sen Memorial Hospital, Sun Yat-Sen University.

# **Experimental animals**

Female wild-type C57BL/6 mice were obtained from the Animal Experiment Center of Sun-Yat-Sen University. MMTV-PyMT mice and *Adipoq-Cre* mice were sourced from the Jackson Laboratory.  $Nrg4^{flox/flox}$  mice and Apc-L850X mice were purchased from Shanghai Model Organisms Center, Inc (Shanghai, China).  $Nrg4^{flox/flox}$  mice were crossed with Adipoq-Cre mice to generate mice with Nrg4 conditional knockout in adipocytes (Adipoq-Nrg4 $^{\Delta}$ ). Adipoq-Nrg4 $^{\Delta}$  mice were then crossed with MMTV-PyMT to generate PyMT; Adipoq-Nrg4 $^{\Delta}$  mice. Genotyping was performed by PCR on tail DNA with specific primers (sequences listed in Table S9). The PCR products were further confirmed by sequencing.

Under specific pathogen-free conditions of animal facility of the Laboratory Animal Resource Center of Sun Yat-Sen University, all mice were raised in individually ventilated cages where the maximum density was five mice per cage. A single investigator individually labeled littermates and randomly assigned them to different experimental groups before the animals received the designated treatment. Other researchers performed the analysis of subsequent experiments while being blinded to the treatment group. For tumor cell inoculation mouse models, tumors did not exceed the maximum volume of 2,000 mm³ in any experiment. For spontaneous breast cancer mouse models, the sum of individual tumor volumes in each mouse yield the total tumor burden, and the endpoint was set as either the total burden summed to 3,000 mm³ or a single tumor measured 2,000 mm³. All surgical and sampling procedures were preceded by intraperitoneal injection of 40 mg/kg pentobarbital sodium to anesthetize the mice, unless otherwise stated. All animal studies received approval and permission from the Institutional Review Boards and Animal Care and Use Committees of Sun Yat-Sen University.

# **Cell lines and cell culture**

Mouse cell lines including EO771 (breast cancer), AML12 (hepatocyte), and 3T3-L1 (pre-adipocyte) were obtained from the American Type Culture Collection (ATCC). EO771 cells were grown in RPMI 1640 (Gibco, 11875093) containing 10% fetal bovine serum (FBS, Gibco, 10099-141). AML12 cells were grown in Dulbecco' modified Eagle's medium (DMEM)/F12 medium (HyCyte, TCM-G709), with supplements of 10% FBS, 1% insulin, and  $1\mu M$  dexamethasone. DMEM (Gibco, 11995065) supplemented with 10% FBS served as the culture medium for 3T3-L1 pre-adipocytes. Cells were cultured in a humidified incubator at  $37^{\circ} C$  with 5% CO $_2$  and regular testing was conducted to verify that they were not contaminated with mycoplasma.

In some experiments, AML12 cells were exposed to a pathophysiologically relevant concentration of palmitic acid (PA) to induce fat accumulation as previously described. AB Briefly, 13.92 mg PA powder (Sigma-Aldrich, P9767) was resolved in 5 mL 0.1M NaOH at 70°C. The mixture was then added to 5 mL 10% fatty acid-free BSA, and dissolution was achieved by gently shaking at 37°C overnight. AML12 cells were exposed to 0.5 mM PA for 24 h. 3T3-L1 adipocytes received treatment with 10  $\mu$ g/mL exosomes separated from PA-treated AML12 cells for 3 days. Culture media and 3T3-L1 adipocytes were collected for subsequent analysis. To prepare conditioned medium for exosome isolation, ultracentrifugation of FBS at 100,000  $\times$  g for 4 hr yielded exosome-depleted FBS.

# **METHOD DETAILS**

### **Meta-analysis**

A systematic literature search covering the period from the inception date up to 31st December 2022 was performed using PubMed, Web of Science, Embase, and Scopus databases, focusing on all observational cohort studies that examine breast cancer incidence in humans with and without NAFLD. The search strategy was: ((breast neoplasms[MeSH Terms]) OR (breast tumor) OR (breast cancer) OR (breast carcinoma) OR (breast malignant cancer) OR (breast malignant tumor) OR (breast malignant carcinoma) OR (mammary tumor) OR (mammary cancer) OR (mammary carcinoma) OR (mammary neoplasms)) AND ((non-alcoholic fatty liver disease [MeSH Terms]) OR (NAFLD) OR (NASH) OR (fatty liver) OR (liver steatosis) OR (steatosis, liver) OR (nonalcoholic steatohepatitis) OR (fatty liver, nonalcoholic)).

Inclusion of studies was conditional upon their fulfillment of all the following criteria: (1) exploring the association between NAFLD and breast cancer; (2) risk estimates (odds ratios (ORs), hazard ratios (HRs) or incidence rate ratios (IRRs)) with their corresponding 95% confidence intervals (CI) were either reported or calculable; (3) NAFLD was diagnosed by either ultrasound, radiology or histopathological examination according to the International Classification of Diseases, 9th Revision (ICD-9) or ICD-10 codes, and patients were in the absence of significant alcohol consumption and chronic viral hepatitis; (4) breast cancer was diagnosed by





histopathological examination. Female participants from the included studies in the meta-analysis had no restriction regarding of race, ethnicity or comorbidities. Exclusion criteria for studies were as follows: (1) reviews, animal studies, *in vitro* studies, genomic studies, meta-analyses, comments, meeting reports, case reports, erratum, no cancer topics, other cancer topics, clinical techniques and clinical models; (2) NAFLD diagnosis was based exclusively on serum liver enzyme levels or alternative surrogate markers such as the fatty liver index; (3) full text was not available to extract valid data; (4) studies in which NAFLD was caused by Selective Estrogen Receptor Modulator (SERM) or other drugs; (5) studies conducted in pediatric population (individuals under 18 years of age).

Two independent investigators (C.L. and Y. Li) reviewed all titles, abstracts and full texts of potentially relevant papers for data extraction and quality assessment. Any differences of opinion were resolved by consensus, with a third author (T.L.) consulted when necessary. Information on study design, sample size, study country, population characteristics, NAFLD diagnosis methods, follow-up duration, and evaluation of the outcomes of interest (the HR, 95% CI and p-value) was collected for every study. For studies that didn't provide HR but presented Kaplan-Meir curves depicting the recurrence-free survival (RFS), we employed Engauge Digitizer software to estimate the HR and 95% CI. <sup>103</sup> The quality of study was assessed via the Newcastle-Ottawa Scale (NOS), following the recommendations by the Cochrane Collaboration. <sup>104</sup> Employing a star system (with nine stars as the maximum), the NOS evaluates studies across three dimensions: how participants are selected, the comparability of study groups, and the ascertainment of outcomes of interest. Studies that score of 7-9 stars represent high-quality scores, 4-6 stars represent medium scores, and those that 1-3 stars represent low scores. All included studies for this meta-analysis were scored at least 7 stars, which were considered high quality. <sup>105</sup>

The primary outcomes for this meta-analysis were the breast cancer incidence in general population and the RFS rate in patients with breast cancer. HRs, IRRs, and ORs with their 95% CIs were extracted from all eligible studies for meta-analysis. When multiple adjustment models were present in studies, those with the most extensive adjustment for potential confounding risk factors were selected for extraction. The I-square ( $l^2$ ) statistic was used to assess statistical heterogeneity. As noted by Higgins and Thompson,  $l^2$  values of around 25% indicate low heterogeneity; around 50% indicate moderate heterogeneity; and around 75% indicate high heterogeneity. Studies with an  $l^2$ <50% were analyzed using a fixed effects model. Funnel plot and Begg's rank test were employed to evaluate publication bias.  $l^2$ 

All statistical tests utilized a two-sided design, with significance determined by a p-value less than 0.05. For the performance of all statistical analyses, the meta-analysis package in Review Manager (RevMan) Version 5.4 was employed; this software is from The Nordic Cochrane Centre, The Cochrane Collaboration, Copenhagen (2020).

### **Dietary interventions**

Four-week-old female C57BL/6 or MMTV-PyMT mice were given a high fructose diet (HFrD), which is the 60% Fructose Diet (Teklad, 89247; 66.8% kcal from carbohydrate, 13% kcal from lipid, and 20.2% kcal from protein), or a control diet (CD, 59.4% kcal from carbohydrate, 4.3% kcal from lipid, and 24.3% kcal from protein) for 10 or 18 weeks, respectively. Body weights, fasting glucose and insulin levels were monitored weekly. To examine the glucose and insulin levels, MMTV-PyMT mice or C57BL/6 mice underwent a 12-hour fast, and blood glucose levels were assessed with a glucometer (Haier, G-425-1). A mouse insulin enzyme-linked immunosorbent assay (ELISA) kit (Elabscience, E-EL-M1382) was used to assess serum insulin levels.

In some experiments, four-week-old female C57BL/6 mice were given a high fat diet (HFD, Research Diets, D12492; 60% kcal from lipid, 19% kcal from carbohydrate, and 20% kcal from protein) or CD for 16 weeks.  $^{108}$  For hepatic steatosis evaluation, livers were harvested from C57BL/6 or MMTV-PyMT mice after four weeks of CD or HFrD feeding  $^{27}$  and embedded in paraffin for subsequent analysis. For BODIPY staining, mammary tumors and adjacent fat pads were harvested from 12-week-old MMTV-PyMT mice or PyMT;  $Adipoq-Nrg4^{\Delta}$  mice fed either CD or HFrD for cryosection preparation. In some experiments, CD-fed or HFrD-fed C57BL/6 mice or  $Adipoq-Nrg4^{\Delta}$  mice were inoculated with 1  $\times$  10 $^{6}$  EO771 cells under the mammary fat pads. Four weeks later, mice were euthanized and mammary tumors were excised for cryosection preparation. In some experiments, four-week-old C57BL/6 mice, which were fed either a CD or HFrD, were inoculated with or without EO771 cells. Four weeks later, mice were euthanized and livers were excised for cryosection preparation.

### **Animal studies**

For EO771 tumor inoculation, female C57BL/6 and  $Adipoq\text{-}Nrg4^\Delta$  mice, which had been fed either CD or HFrD for four weeks since the age of four weeks, were inoculated with 1  $\times$  10<sup>6</sup> EO771 cells under the mammary fat pads. After tumor inoculation, they were fed either a CD or HFrD until the endpoint of the experiment. In some experiments, six-week-old female CD-fed C57BL/6 mice were inoculated with 1  $\times$  10<sup>6</sup> EO771 cells under the mammary fat pads or on the dorsolateral flank. Two weeks following tumor inoculation, mice were transplanted without or with normal livers or fatty livers.

Over a four-week period, tumor volumes were measured with a caliper at three-day intervals and calculated via the modified formula: volume = length  $\times$  width  $\times$  width/2. Length is defined as the longest dimension of tumors and width is perpendicular to the length. In some experiments, primary tumors were surgically removed under anesthesia four weeks after tumor inoculation. Two weeks after the surgery, mice were sacrificed and lungs were then harvested and embedded in paraffin for lung metastasis analysis.

To examine the onset of mammary tumors, eight-week-old female MMTV-PyMT mice and PyMT;  $Adipoq-Nrg4^{\Delta}$  mice, which were fed either a CD or HFrD since the age of four weeks, were palpated daily until mammary tumor was detected. The mice were fed either a CD or HFrD until the endpoint of the experiment. To assess lung metastasis of MMTV-PyMT mice, lungs were harvested from

# **Cell Metabolism**





22-week-old female MMTV-PyMT mice or PyMT; *Adipoq-Nrg4*<sup>Δ</sup> mice, which were fed either a CD or HFrD since the age of four weeks, and embedded in paraffin for subsequent analysis.

### Whole-mount mammary gland carmine staining

Mammary fat pads were harvested from eight-week-old female MMTV-PyMT mice, which had been fed either CD or HFrD for four weeks. Mammary whole-mount analysis was executed under the previously described procedure. <sup>109</sup> Briefly, mammary fat pads were excised, flattened on slides, and air dried for 5 min, followed by fixation overnight at room temperature in Carnoy's solution, which consists of 30% glacial acetic acid, 30% absolute ethanol, and 10% chloroform. Subsequent to this step, the specimens were rinsed with 70% ethanol and subjected to gradual rehydration, and stained with Carmine Alum (Stem Cell Technologies, 07070) overnight at 4°C. Subsequently, the samples underwent dehydration in ethanol, clearing in xylene, and storage in methyl salicylate at room temperature. Image acquisition was performed with a Stereo Microscope (Leica, M205FA). The level of mammary gland hyperplasia was quantified by calculating the ratio of the hyperplastic lesion area to the total area of specimen using Image J software.

# **Orthotopic mouse liver transplantation**

After being fed either CD or HFrD for four weeks, female C57BL/6 mice at the age of eight weeks were utilized as liver donors. Eightweek-old female C57BL/6 mice fed a CD were utilized as liver recipients, which had been inoculated with EO771 cells for two weeks. The performance of mouse orthotopic liver transplantation surgery followed the method described previously.<sup>29</sup> In brief, both donors and recipients were anesthetized with 1%-3% inhaled isoflurane (RWD Life Science, R510-22) and administered a subcutaneous injection of 0.05 mg/kg buprenorphine hydrochloride (Sigma-Aldrich, B-044S-1ML). Donor mice were placed under a digital microscope (DM3) and an incision was made along the midline of the abdomen extending from the xiphoid process to the pubis. The ligaments around the liver were cut to expose the proper hepatic artery (PHA), which was then cut off and ligated with 10-0 nylon suture. Subsequently, the extrahepatic bile duct (BD) was cut off. A bile duct stent was inserted into the BD and fixed with 7-0 silk. The veins around the infrahepatic inferior vena cava (IHIVC) were exposed and cut off. Heparin sodium (20 U per mouse) (Sigma-Aldrich, PHR8927) was injected into the tail vein using a 0.5-mL U-100 insulin syringe (28-gauge). Cold saline at 4°C was slowly injected into the donor liver via the IHIVC using a 5 mL syringe with a 27-gauge needle until the liver turned evenly pale. The portal vein (PV) located beneath the splenic vein was then cut to form an exit for the perfusion solution. The liver was retracted downward to expose the suprahepatic inferior vena cava (SHIVC), and the falciform ligament was incised. The anterior wall and posterior wall of the SHIVC were cut subsequently. Finally, the remaining ligaments and connective tissues surrounding the liver were cut. The grafts were immediately immersed in cold saline solution and stored for no more than 30 min. Recipients were injected subcutaneously with 100 mg/kg ceftriaxone (Macklin, C877598). The recipient mouse's liver was dissected in the same way as in the donor liver. The graft was positioned orthotopically within the abdominal cavity of the recipient. The bilateral edges of the recipient's SHIVC were sutured, ensuring that any air was expelled from the SHIVC cavity to avoid air-induced thrombosis. The PV, IHIVC and BD were connected as previously described.<sup>29</sup> The BD stent, PV and IHIVC cuffs were placed into their respective positions within the recipient and secured using a 7-0 silk ligature. The abdominal cavity was perfused with warm saline to ensure the absence of intra-abdominal bleeding. A continuous running 4-0 vicryl suture was used to close the abdominal incision in two layers. The recipient mice were then placed in a warm cage for recovery. Mice receiving either normal or fatty liver grafts were fed a CD until the endpoint of the experiment. To assess the changes of fatty livers after transplantation, three mice receiving fatty liver transplantation were sacrificed and hepatic steatosis was assessed using livers collected at day 2, 7 and 14 after transplantation. Two weeks after liver transplantation, primary tumors were surgically removed under anesthesia. Two weeks post-surgical resection, mice were euthanized, and their lungs were collected and embedded in paraffin for lung metastasis analysis.

# **Histological analyses**

For H&E staining, livers, lungs and mammary fat pads were fixed in a 4% paraformaldehyde (PFA) fix solution overnight at 4°C and then processed for paraffin embedding. Paraffin-embedded tissues were cut into 4-μm-thickness sections. Sections were deparaffinized, stained with H&E, and mounted using Permount Mounting Medium (Servicebio, WG10004160). H&E-stained sections were imaged using a digital slide scanner (NanoZoomer@S360).

To quantify mouse lung metastatic lesions, serial sections of the entire lung were obtained at an interval of 200 μm and H&E staining was performed. The identification of metastatic tumor cells was based on the following criteria: a high hematoxylin-to-eosin ratio, disrupted surrounding lung structure, abnormal nuclear size or shape, presence of abnormal mitotic spindles (or any combination thereof), and variations in cell size and shape. The lesions with at least one metastatic tumor cell were defined as lung metastatic lesions.<sup>110</sup> The average count of metastatic lesions across all lung sections from each mouse was quantified.

To assess hepatic steatosis, the percentage of steatosis in H&E-stained liver sections was quantified using ImageJ software as previously described.  $^{111}$  Briefly, three randomly selected liver sections of each mouse were analyzed. In each section, six randomly selected images at  $400 \times \text{magnification}$  were captured. Hepatic steatosis lesion was defined as the area with lipid droplets. The average percentage of the area of hepatic steatosis to total specimen area of each mouse was quantified. Fatty livers were defined as those with an average percentage of hepatic steatosis > 5%.





### Isolation of cells from mouse livers

Different types of cells were isolated from livers of C57BL/6 mice as previously mentioned. <sup>37</sup> Briefly, mice were euthanized with 40 mg/kg pentobarbital sodium. The livers were subjected to retrograde perfusion via the inferior vena cava with 10 mL Hank's balanced salt solution (HBSS, Gibco, C14175500BT) supplemented with 10 mM HEPES (Gibco, 15630080) and 100 U/mL penicillin and 100  $\mu$ g/mL streptomycin for 2 min. Subsequently, livers were perfused with 25 mL 0.5 mg/mL pronase solution (Sigma-Aldrich, P5147) for 5 min, followed by 35 mL 0.3 mg/mL collagenase D (Roche, 11088866001) containing 10 mM HEPES, 100 U/mL penicillin and 100  $\mu$ g/mL streptomycin for 7 min at 37°C. Livers were perfused at a rate of 5 mL/min. Both the perfusion and digestion stages were conducted in the presence of 1 mM flavopiridol to counteract transcriptional changes induced by digestion. After digestion, livers were gently dissociated using forceps in 20 mL warm DMEM/F12 medium, which contained 10% exosome-depleted FBS, 100  $\mu$ g/mL streptomycin, and 100 U/mL penicillin. Samples were then filtered through a 70  $\mu$ m nylon mesh. Centrifugation at 50  $\times$  g for 5 min at 4 °C was used to pellet hepatocytes. A fraction enriched in hepatocytes was acquired using a 40% Percoll density gradient (250  $\times$  g for 6 min). <sup>112</sup> Primary hepatocytes were cultured in DMEM/F12 with 10% exosome-depleted FBS. Supernatants were harvested to obtain leukocytes, fibroblasts (hepatic stellate cells, HSCs), liver sinusoidal endothelial cells (LSECs) and cholangiocytes.

Leukocytes, LSECs<sup>39</sup> and cholangiocytes<sup>40</sup> were isolated using magnetic-activated cell sorting (MACS) with anti-CD45 Microbeads (mouse) (Miltenyi Biotec, 130052301), anti-CD146 Microbeads (mouse) (Miltenyi Biotec, 130092007), and anti-CD326 (Ep-CAM) microbeads (mouse) (Miltenyi Biotec, 130105958) as previously described, respectively. Leukocytes were cultured in DMEM containing 10% exosome-depleted FBS. LSECs were cultured in DMEM with 10% exosome-depleted FBS and 10 nM VEGF (Sino Biological, 50159-MNAB). Cholangiocytes were maintained in DMEM with 10% exosome-depleted FBS containing 5 ng/mL epidermal growth factor (EGF, Corning, 354001) and 5 ng/mL hepatocyte growth factor (HGF, Sigma-Aldrich, GF155).

HSCs were isolated using gradient centrifugation as previously mentioned. He supernatants were centrifuged at  $580 \times g$  for 10 min at 4°C, and the resulting pellet was then resuspended in 8 mL Gey's balanced salt solution B (GBSS-B, Sigma-Aldrich, G9779) and 4 mL Nycodenz (Accurate Chemical, AN1002424). The mixture was centrifuged at  $1,380 \times g$  for 17 min at 4°C. After centrifugation, the intermediate layer containing HSCs was carefully harvested, washed with GBSS-B, and centrifuged at  $580 \times g$  for 10 min at 4°C. HSCs in the pellet were resuspended and cultured in DMEM with 10% exosome-depleted FBS.

# Preparation of conditioned medium (CM) from mouse livers and cells

To prepare CM from mouse livers, whole liver lobes were harvested from C57BL/6 mice fed either CD or HFrD for 4 weeks. Livers were perfused with 10 mL PBS, mounted in 3% low-temperature gelling agarose (Sigma-Aldrich, A9414), and sliced into 300- $\mu$ M sections with a vibratome (Leica VT1200s) in RPMI 1640 containing 100  $\mu$ g/mL streptomycin and 100 U/mL penicillin. Each liver slice was washed with PBS and incubated for 16 h in 11 mL RPMI 1640 containing 10% exosome-depleted FBS, 100  $\mu$ g/mL streptomycin and 100 U/mL penicillin at 37°C. The culture medium was harvested and subjected to centrifugation at 2,000  $\times$  g for 20 min to eliminate cellular and tissue debris. The culture medium was harvested and subjected to centrifugation at 2,000  $\times$  g for 20 min to eliminate cellular and tissue debris.

To prepare CM from cells, primary cells isolated from mouse livers, AML12 cells and EO771 cells were cultured in 11 mL RPMI 1640 (Gibco, 11875093) supplemented with 10% exosome-depleted FBS, 100  $\mu$ g/mL streptomycin and 100 U/mL penicillin at 37°C. After 48 hr, the culture medium was harvested and subjected to centrifugation for 20 min at 2,000  $\times$  g to eliminate cellular debris. Resulted samples were collected as CM and used for *in vivo* treatment or fractionation.

# **CM** fractionation

CM of mouse livers, primary cells from mouse livers, AML12 cells or EO771 cells were collected as aforementioned and then centrifuged at  $100,000 \times g$  for 2 hr at  $4^{\circ}$ C in a SW41 Ti swinging-bucket rotor (Beckman Coulter). The supernatants (S) containing soluble factors were collected for *in vivo* treatment. The pellets (P) were collected for *in vivo* treatment, or used for microvesicle and exosome isolation. To isolate microvesicles and exosomes, the pellets (P) were resuspended in 11 mL PBS and centrifuged at  $16,500 \times g$  for 45 min at  $4^{\circ}$ C. The resulting pellet containing microvesicles was then washed with PBS and resuspended in  $100 \,\mu\text{L}$  PBS. The resulting supernatant was collected and centrifuged at  $100,000 \times g$  for 2 hr at  $4^{\circ}$ C to obtain exosomes. The pelleted exosomes were washed with PBS and centrifuged at  $100,000 \times g$  for 2 hr at  $4^{\circ}$ C. Isolated exosomes were resuspended in  $100 \,\mu\text{L}$  PBS for subsequent experiments. The size and number of exosomes were examined using a NanoSight NS300 instrument (Malvern Instruments) with nanoparticle tracking analysis (NTA)  $3.0 \, \text{analytical}$  software (Malvern Instruments). The exosome protein concentration was measured using the detergent-insensitive Pierce BCA protein assay kit (Thermo Fisher Scientific, 23227).

# Serum exosome quantification

Mouse serum exosomes were isolated and quantified by detecting exosome protein concentration as previously described with slight modifications. <sup>20</sup> Briefly, C57BL/6 mice at four weeks of age were given either a CD or HFrD for four weeks. Fatty liver exosomes were isolated from liver CM of C57BL/6 mice fed HFrD as described previously. CD-fed mice were intravenously injected via tail vein without or with fatty liver exosomes at a dose of 3  $\mu$ g, 10  $\mu$ g, 30  $\mu$ g or 90  $\mu$ g in 100  $\mu$ L PBS. After 24 h, mouse serum was collected, diluted with PBS (200  $\mu$ L to 11 mL) and centrifuged at 2,000  $\times$  g for 20 min to eliminate cellular and tissue debris. The sample was subsequently centrifuged at 16,500  $\times$  g for 45 min at 4°C, aiming to remove microvesicles. The supernatant was then collected and subjected to centrifugation at 100,000  $\times$  g for 2 hr at 4°C to obtain exosomes. <sup>31</sup> Pierce BCA protein assay kit was used to quantify the exosome protein concentration.

# **Cell Metabolism**

# **Article**



# In vivo treatment with CM and CM fractions

For *in vivo* CM treatment, all CM was collected from slices of a whole mouse liver (nearly 11 mL) harvested from CD- or HFrD-fed C57BL/6 mice after incubation for 16 h. Using Amicon Ultra-15 centrifugal filters with 10 kDa cutoff (Millipore, UFC901008), CM was concentrated to 100  $\mu$ L through centrifugation at 4,000  $\times$  g at 4°C. <sup>20</sup> Concentrated CM (100  $\mu$ L per mouse) was administered intravenously through the retro-orbital venous sinus into C57BL/6 mice two weeks after EO771 cell inoculation and continued every other day until the endpoint of the experiment.

To treat C57BL/6 mice with fatty liver supernatant (S) or pellet (P) isolated from CM, all CM from slices of a whole liver (nearly 11 mL) harvested from HFrD-fed C57BL/6 mice were collected. Supernatants (S) from 11 mL CM were centrifuged at 4°C using Amicon Ultra-15 centrifugal filters with 10 kDa cutoff (Millipore, UFC901008) at  $4,000 \times g$  to a final volume of  $100 \, \mu L$ . Pellets (P) isolated from 11 mL CM were rinsed with PBS and resuspended in  $100 \, \mu L$  PBS. Concentrated supernatants ( $100 \, \mu L$  per mouse) or pellets ( $100 \, \mu L$  per mouse) were administered intravenously into C57BL/6 mice via retro-orbital venous sinus two weeks after EO771 cell inoculation and continued every other day until the endpoint of the experiment. In some experiments, C57BL/6 mice were administered microvesicles isolated from CM of slices of a whole liver (nearly 11 mL) harvested from HFrD-fed C57BL/6 mice.

### In vivo exosome treatment

To treat mice with exosomes, CM from mouse liver slices, primary hepatocytes or AML12 cells exposed to 0.5 mM PA for 24 h was pooled. Exosomes were isolated from CM and the concentration of exosome protein was measured. Exosomes were intravenously injected into each mouse at a dose of 30 μg exosomal protein (in 100 μL PBS), which is consistent with the dosage used in prior studies, <sup>30,113</sup> every other day. This concentration falls within the range of pathophysiological serum exosome concentration of diet-induced mouse models of NAFLD and NAFLD patients as previously reported.<sup>113</sup>

In some experiments, four-week-old female C57BL/6 or  $Adipoq-Nrg4^{\Delta}$  mice were inoculated with 1  $\times$  10<sup>6</sup> EO771 cells under the mammary fat pads. Two weeks after tumor inoculation, the mice were intravenously injected without or with 30  $\mu$ g exosomes for four weeks. These exosomes were isolated from CM of liver slices or primary hepatocytes of CD-fed or HFrD-fed mice with or without EO771 cell inoculation, or from PA-treated AML12 cells. Primary tumors were surgically removed under anesthesia four weeks after tumor inoculation. Mice were sacrificed two weeks after surgery, and lungs were then harvested for lung metastasis analysis. In some experiments, eight-week-old MMTV-PyMT mice were intravenously injected with or without 30  $\mu$ g fatty liver exosomes isolated from HFrD-fed mice every other day for four weeks. Afterwards, mammary fat pads were harvested and embedded in paraffin for subsequent analysis.

In some experiments, exosome release in mice was inhibited by injecting exosome release inhibitors as previously described. Briefly, exosome-releasing inhibitors GW4869 (MedChemExpress, HY-19363, 1.25 mg/kg/day) and Dimethylamiloride (DMA, MedChemExpress, HY-138866; 1  $\mu$ M/kg/day) were administered intraperitoneally to eight-week-old HFrD-fed MMTV-PyMT mice or HFrD-fed C57BL/6 mice immediately after tumor cell inoculation and continued every day until the endpoint of the experiment. 114

To assess the uptake of exosomes by a specific cell type,  $30\,\mu g$  isolated exosomes were resuspended in 1 mL PBS and incubated with 5  $\mu$ M/L Dil dye (Thermo Fisher Scientific, D3911) for 1 hr at room temperature in the dark. After being washed with PBS, the mixture was centrifuged at  $100,000\times g$  for 70 min and then resuspended in  $100\,\mu L$  PBS. C57BL/6 mice were intravenously injected with  $30\,\mu g$  Dil-labeled exosomes isolated from liver CM of HFrD-fed mice. After 24 h, mammary fat pads were harvested, fixed overnight at 4°C in 4% PFA solution and then embedded in the Tissue-Tek O.C.T. embedding compound (SAKURA, 4583). Embedded tissues were frozen overnight at -30°C and then sectioned into 20- $\mu$ m-thick cryosections. In some experiments, C57BL/6 mice were inoculated with 1  $\times$  10<sup>6</sup> EO771 cells under the mammary fat pads. Two weeks after tumor inoculation, mice were administered intravenously with 30  $\mu$ g Dil-labeled exosomes isolated from liver CM of HFrD-fed mice. After 24 h, tumors and adjacent mammary fat pads were harvested to prepare cryosections.

For BODIPY staining, eight-week-old female MMTV-PyMT mice were intravenously injected with 30  $\mu$ g exosomes isolated from liver CM of HFrD-fed mice every other day for four weeks. Mammary tumors and adjacent fat pads were harvested 24 h after the final treatment for cryosection preparation. In some experiments, four-week-old female C57BL/6 mice and Adipoq- $Nrg4^{\Delta}$  mice were inoculated with 1  $\times$  10<sup>6</sup> EO771 cells under the mammary fat pads. Two weeks after tumor inoculation, mice were administered intravenously with 30  $\mu$ g exosomes isolated from either liver CM of HFrD-fed mice or CM of PA-treated AML12 cells, every other day for two weeks. Mammary tumors were harvested 24 h after the final treatment for cryosection preparation.

In some experiments, mice were administered with or without 30  $\mu$ g exosomes isolated from liver CM of HFrD-fed mice for four weeks. Then,  $5 \times 10^5$  EO771 cells were intravenously injected into the mice via tail vein. Mice were administered with or without 30  $\mu$ g exosomes from liver CM of HFrD-fed mice for four weeks. Mice were then sacrificed and lungs were harvested for lung metastasis analysis.

For spontaneous colorectal cancer tumorigenesis, eight-week-old female Apc-L850X mice were intravenously injected without or with 30 µg exosomes isolated from liver CM of HFrD-fed mice for four weeks. Then mice were sacrificed and colorectal tissues were collected. The number of colorectal tumors was counted. Tumor diameter was measured with a caliper. The total volume of tumors was determined by summing of all volumes of tumors in the colorectum of one mouse. <sup>116</sup>





### In vivo distribution of exosomes

Exosomes were stained with lipophilic fluorescent dye as previously mentioned. He fill Briefly, exosomes were isolated from CM of mouse livers, CM of PA-treated AML12 cells or EO771 cells. To visualize the biodistribution of exosomes *in vivo*, 30  $\mu$ g Dil-labeled exosomes were injected into C57BL/6 mice or *Adipoq-Nrg4*<sup> $\Delta$ </sup> mice via tail vein. After 24 h of injection, mice were anesthetized, and an *In Vivo* Imaging System (IVIS) Lumina Imaging System (Caliper Life Sciences) was used to detect Dil signals.

To detect exosome distribution, organs and fat tissues were harvested after mice were sacrificed. Samples were examined with fluorescence imaging using IVIS Lumina Imaging System. Fluorescence was detected using the Region of Interest (ROI) tool in the Living Image software. All experiments followed these imaging parameters: excitation filter 535 nm and emission filter 580 nm; f-stop set to 2; medium binning; and automatic exposure time. Fluorescence intensity expressed as radiant efficiency was illustrated via a pseudocolor spectrum–dark red representing the lowest intensity and yellow denoting the highest. Image analysis was performed using Living Image software v.3.0. (Caliper Life Sciences).

### **Neutralization of ErbB4 in exosomes**

To neutralize ErbB4 in exosomes, exosomes were isolated from CM of liver slices or primary hepatocytes isolated from HFrD-fed mice. Exosomes were treated with the neutralizing antibody as previously described with a slight modification. <sup>118</sup> Briefly, 30  $\mu$ g exosomes were resuspended in 1.5 mL PBS, followed by incubation with 20  $\mu$ g/mL anti-mouse ErbB4 antibodies (BioVision, A1047) or anti-mouse isotype control antibodies (Bioxcell, BE0083) overnight at 4°C. After being washed with PBS, the mixture was centrifuged at 100,000  $\times$  g for 70 min to eliminate unbound antibody. Then the pellets were resuspended in 100  $\mu$ L PBS and stored at 4°C, with a storage time not exceeding 24 h before use. Two weeks after tumor inoculation, C57BL/6 mice were administered intravenously with exosomes at a dose of 30  $\mu$ g exosomal protein in 100  $\mu$ L PBS for four weeks.

In some experiments, eight-week-old HFrD-fed C57BL/6 or HFrD-fed MMTV-PyMT mice were administered intraperitoneally with 0.5 mg/kg anti-mouse ErbB4 antibodies (BioVision, A1047) or anti-mouse isotype control antibodies (Bioxcell, BE0083) immediately after tumor inoculation and continued every three days until the endpoint of the experiment. 119

### Western blot

Cells, tissues, exosomes, and cytosolic or mitochondrial fractions of cells (as described in the cytosolic and mitochondrial fractionation section below) were lysed on ice for 15 min in RIPA lysis buffer (Thermo Fisher Scientific, 89900) with the addition of protease inhibitor cocktail (Thermo Fisher Scientific, 78440). The lysates were centrifuged for 20 min at 15,000 × g at 4°C to remove debris. The detergent-insensitive Pierce BCA protein assay kit (Thermo Fisher Scientific, 23227) was used to determine protein concentration. Samples were denatured at 95°C for 5 min after the addition of NuPAGE LDS-Sample buffer (4x) (Thermo Fisher Scientific, NP0008). Equal amounts of protein (30 μg) in 1 × loading buffer (Thermo Fisher Scientific, NP0008) were loaded onto SDS-polyacrylamide gel electrophoresis (PAGE). Subsequent to electrophoresis, proteins were transferred to polyvinylidene difluoride (PVDF) membranes (Roche, 03010040001) and blocked with 5% bovine serum albumin (BSA, Asegene, 43035) in Tris-buffered saline containing 0.1% Tween-20 (TBST) for 1 hr at room temperature. The membranes were then incubated with primary antibodies including rabbit anti-mouse CD81 (Abcam, ab109201, 1:1000), rabbit anti-mouse ALIX (Proteintech, 12422-1-AP, 1:1000), rabbit anti-mouse ARF6 (Proteintech, 20225-1-AP, 1:1000), rabbit anti-mouse calnexin (Proteintech, 10427-2-AP, 1:1000), rabbit anti-mouse ErbB4 (Proteintech, 19943-1-AP, 1:1000), rabbit anti-mouse Nrg1 (Proteintech, 10527-1-AP, 1:1000), rabbit anti-mouse Nrg2 (GeneTex, GTX12019, 1:1000), rabbit anti-mouse Nrg3 (Abcam, ab109256, 1:1000), rabbit anti-mouse Nrg4 (GeneTex, GTX64845, 1:1000), rabbit anti-mouse FATP1 (Affinity Biosciences, DF7716, 1:1000), rabbit anti-mouse FATP4 (Proteintech, 11013-1-AP, 1:1000), rabbit anti-mouse TRMT10C (Proteintech, 29087-1-AP, 1:1000), rabbit anti-mouse RPS16 (Abcam, ab177951, 1:1000), rabbit anti-mouse MRPS5 (Thermo Fisher Scientific, PA5-75889, 1:1000), rabbit anti-mouse ND6 (Affinity Biosciences, DF9676, 1:1000), rabbit antimouse ND5 (Proteintech, 55410-1-AP, 1:1000), rabbit anti-mouse CGI-58 (Immunoway, YN4673, 1:1000), horseradish peroxidase (HRP)-Conjugated α-Tubulin (Proteintech, HRP-66031, 1:1000), HRP-Conjugated GAPDH (Proteintech, HRP-60004, 1:1000) or mouse anti-mouse VDAC1 (Proteintech, 66345-1-Ig, 1:1000) in 5% BSA in TBST overnight at 4°C. Membranes were washed three times with TBST and subsequently incubated for 1 hr at room temperature with HRP-conjugated anti-rabbit antibody (Cell Signaling Technology, 7074, 1:3000) or HRP-linked anti-mouse antibody (Cell Signaling Technology, 7076, 1:3000). Chemiluminescent reagents (Thermo Fisher Scientific, 34095, 34580) were used to develop the membranes following the manufacturer's instructions. Blot intensity was measured with ImageJ.

# Lipoprotein isolation

Lipoproteins were isolated from mouse plasma using potassium bromide (KBr)-density gradient ultracentrifugation as previously described with slight modifications.  $^{120}$  Briefly, plasma density was adjusted to d=1.25 g/mL as the final density by mixing the plasma with solid KBr at a ratio of 0.398 g per mL of plasma. The mixture was topped with 0.9% saline to fill the SW41 Ti ultracentrifuge tube and ultracentrifuged at 260,000  $\times$  g at 4°C for 12 hr (Beckman Coulter). Afterwards, the top layer was removed to an Amicon Ultra 10 kDa centrifugal filter tube (Millipore, UFC901008) and centrifuged at 4,000  $\times$  g at 4°C for 10 min to condense lipoproteins. Lipoprotein samples were analyzed using the transmission electron microscope.

# **Cell Metabolism Article**



# Transmission electron microscope (TEM) analysis

Exosomes isolated from CM and lipoproteins isolated from mouse plasma were analyzed using negative staining with TEM as previously described.<sup>20</sup> Briefly, 30 μg exosomes or lipoproteins in 100 μL PBS were applied to a formvar/carbon-coated grid and left to settle for 1 min. The samples were blotted on filter paper and negatively stained with four consecutive drops of 1.5% aqueous uranyl acetate, with blotting performed between each drop. After the final drop, the grids were blotted and left to air-dry at room temperature for 10 min. The grids were incubated with a drop of BSA solution to block for 1 hr. Without rinsing, the grids were incubated with the rabbit anti-mouse ErbB4 antibody (Cell Signaling Technology, 4795T, 1:100) overnight at 4°C. After being washed with PBS, the grids were incubated with a 10-nm gold particle-conjugated secondary antibody (Abcam, ab270555, 1:100) at room temperature for 2 hr. Grids were rinsed with PBS and incubated for 15 min with a drop of 2.5% glutaraldehyde in 0.1 M phosphate buffer. After being rinsed in PBS and distilled water, the grids were air-dried and stained with a drop of 2% uranyl acetate for 30 min at room temperature. The grids were then analyzed using a transmission electron microscope (JEOL JEM-1200EX).

# **TEM** analysis for cryosections

TEM analysis for exosome detection in mammary fat pad cryosections was performed as previously mentioned. 42 Briefly, 30 µg exosomes isolated from HFrD-fed mice were resuspended in 1 mL PBS and incubated with 5 μg/mL FM1-43FX dye (Thermo Fisher Scientific, F35355) for 1 hr in darkness at room temperature. After being washed with PBS, samples were centrifuged at  $100,000 \times g$  for 70 min and resuspended in 100 μL PBS. C57BL/6 mice were injected intravenously with FM1-43FX-labeled exosomes via tail vein. After 24 h, mammary fat pads were harvested and fixed in 2.5% glutaraldehyde (pH 7.4) overnight at 4°C. The tissues were then incubated in 1% osmium tetroxide buffer for 2 hr at room temperature and washed three times with PBS. Following fixation, tissues were dehydrated using graded ethanol (30%, 50%, 70%, 80%, 90% and 95% ethanol, each for 15 min) and 100% ethanol three times, each for 15 min. The tissues were then placed in 100% acetone for 15 min and subsequently embedded in SPI-Pon 812 (SPI, 02660-AB) overnight at room temperature. Afterward, tissues were polymerized in SPI-Pon 812 (SPI, 02660-AB) overnight at 60-70°C. Ultrathin sections (60-80 nm) were cut using an ultramicrotome (Leica EM UC7) and transferred to formvar-coated copper slot grids. Grids were rinsed with distilled water and incubated with 2% uranyl acetate at room temperature for 30 min. The grids were then washed with distilled water and stained with 3% lead citrate at room temperature for 5 min. Following washing and airdrying, grids were imaged via a transmission electron microscope (JEOL JEM-1400).

# Isolation of primary cells from mouse mammary fat pads

Primary cell isolation from mammary fat pads was carried out following the method previously described. 11,20 Briefly, mice were intravenously injected with 30 μg Dil-labelled exosomes isolated from HFrD-fed mice in 100 μL PBS. After 24 h, mice were sacrificed and mammary fat pads were dissected. Subsequently, mammary fat pads were cut into small fragments and digested in DMEM/F12 medium containing 2 mg/mL collagenase type I (Biofroxx, 1904GR001) and 2% BSA with gentle shaking (80 rpm) at 37°C for 1 hr in darkness. Undigested tissue was removed after filtration using a 70 µm cell strainer. Afterward, the cells were washed with PBS containing 2% BSA and 2 mM EDTA, followed by collection through centrifugation at 300 x g for 5 min. Mature adipocytes were collected in the float layer, while other cell types were collected in the pellets. To remove red blood cells, cell pellets were incubated with RBC lysis buffer (Biolegend, 420301) at room temperature for 5 min. Cells were collected and used for flow cytometry.

# Isolation of tumor-infiltrating leukocytes

Tumor-infiltrating leukocytes were isolated from EO771 tumors in mice as previously described. 121 Briefly, two weeks after tumor cell inoculation, EO771 tumor-bearing mice were intravenously injected with 30 µg fatty liver exosomes isolated from HFrD-fed mice every other day for two weeks. After two weeks, mice were sacrificed and tumors were harvested. Then, tumors were minced into small pieces and digested in 10 mL DMEM/F12 medium containing 2 mg/mL collagenase type I (Biofroxx, 1904GR001), 100 μg/mL DNase I (Roche, 10104159001) and 2% BSA with gentle shaking (80 rpm) at 37°C for 1 hr. Undigested tissues were removed by filtration through a 70-µm cell strainer, and cell suspensions were collected. After centrifugation at 300 × g for 3 min, pellets were resuspended in 6 mL 40% Percoll (GE Healthcare, 170891) and carefully added on top of 6 mL 80% Percoll layer. The samples were centrifuged at 1,260 × g at room temperature for 20 min with the brake off. Leukocytes at the interface of the 40% and 80% Percoll layers were collected for subsequent flow cytometry and cell sorting.

# Flow cytometry and cell sorting

Primary cells isolated from mouse mammary fat pads or mouse tumors were rinsed with PBS and subsequently incubated with antimouse FcR (CD16/32, 1:500) (Biolegend, 156603) following the manufacturer's instructions. For the purpose of excluding dead cells, specimens were stained with Live/Dead Fixable Viability Dye (BD Bioscience, 565388, 1:1000) in PBS containing 2% FBS for 30 min at 4°C. Afterwards, cells were stained with Brilliant Violet 421 anti-mouse CD31 (Biolegend, 102423, 1:20), APC anti-mouse CD326 (Ep-CAM) (Biolegend, 118213, 1:20), Alexa Fluor 700 anti-mouse CD45 (Biolegend, 103127, 1:50), Brilliant Violet 510 anti-mouse CD45 (Biolegend, 103137, 1:20), PE/Cyanine7 anti-mouse CD3ɛ (Biolegend, 100319, 1:50), APC anti-mouse CD4 (Biolegend, 100515, 1:50) or FITC anti-mouse CD8a (Biolegend, 100705, 1:100) in PBS containing 2% FBS for 30 min at 4°C. In some experiments, intracellular staining was carried out using the Intracellular Fixation and Permeabilization kit (eBioscience, 88-8824-00) following the manufacturer's instructions. After permeabilization, cells were stained with Alexa Fluor 488 anti-mouse Vimentin (Biolegend, 699305, 1:50), PE anti-mouse Foxp3 (Biolegend, 320007, 1:20) in PBS containing 2% FBS for 30 min at 4°C, or rabbit



anti-mouse Perilipin 1 (Invitrogen, PA5-72921, 1:50) for 30 min at 4°C followed by incubation with 488-conjugated donkey anti-rabbit IgG (Thermo Fisher Scientific, A21206, 1:400) for 1 hr at 4°C. Brilliant Violet 421-conjugated Rat IgG2a (Biolegend, 400535, 1:20), APC-conjugated Rat IgG2a (Biolegend, 400512, 1:20), Alexa Fluor 700-conjugated Rat IgG2b (Biolegend, 400628, 1:20), Alexa Fluor 488-conjugated Rat IgG2a (Biolegend, 400525, 1:20), Brilliant Violet 510-conjugated Rat IgG2b (Biolegend, 400645, 1:20), PE/Cyanine7-conjugated Armenian Hamster IgG (Biolegend, 400921, 1:50), APC-conjugated Rat IgG2a (Biolegend, 400511, 1:50), FITC-conjugated Rat IgG2a (Biolegend, 400505, 1:100) and PE-conjugated Mouse IgG1 (Biolegend, 400139, 1:20) were used as isotype control antibodies.

Treg cells were isolated from tumor-infiltrating leukocytes by flow sorting as previously described with a slight modification.  $^{122}$  Cell sorting was performed using a Beckman MoFlo EQs cell sorter. Treg cells were defined by the following staining: Live/Dead $^{-}$ CD45 $^{+}$ CD3 $^{+}$ CD4 $^{+}$ CD25 $^{+}$ . Treg cells were subsequently analyzed by flow cytometry and qRT-PCR. For lipid content detection,  $1 \times 10^{5}$  Treg cells were stained with BODIPY (Thermo Fisher Scientific, D3922,  $1 \mu g/mL$  in PBS) at  $37^{\circ}$ C for 30 min in darkness.  $^{52}$  After being washed with PBS, the samples were analyzed using a flow cytometer (Beckman CytoFLEX S), and FlowJo software was used to process the data.

In some experiments, intracellular ROS level was assessed using 2', 7'-Dichlorodihydrofluorescein diacetate (H2-DCFDA, MedChemExpress, HY-D0940) staining as previously described. Briefly,  $1 \times 10^5$  3T3-L1 adipocytes or primary adipocytes were incubated with 5 mM H2-DCFDA dye for 30 min at 37°C in darkness. After being washed with PBS, the samples were analyzed using a Flow cytometer (Beckman CytoFLEX S), and data were processed using FlowJo software.

# **Immunofluorescence**

Paraffin-embedded samples were sectioned into consecutive slices of 4  $\mu$ m, deparaffinized and antigen retrieval in EDTA buffer (pH 8.0) using a pressure cooker for 3 min. Sections were treated with 5% BSA for 30 min at room temperature to block nonspecific binding before incubation with primary antibodies: rabbit anti-mouse ASC-1 (GeneTex, GTX47874, 1:200), rabbit anti-mouse CD31 (Abcam, ab222783, 1:200), rabbit anti-mouse Cytokeratin (Abcam, ab53280, 1:200), rat anti-mouse CD45 (Abcam, ab23910, 1:200), mouse anti-mouse Vimentin (Abcam, ab20346, 1:200), rabbit anti-mouse Nrg4 (GeneTex, GTX64845, 1:200), rabbit anti-mouse Tom20 (Proteintech, CL488-11802), rabbit anti-mouse Trmt10c (Proteintech, 29087-1-AP), rabbit anti-mouse FATP1 (Affinity Biosciences, DF7716), rabbit anti-mouse FATP4 (Proteintech, 11013-1-AP) and isotype control IgG antibody (Proteintech, 98136-1-RR) at 4°C overnight. After being washed with PBS, sections were incubated with Alexa Fluor secondary antibodies (Thermo Fisher Scientific, A21206, A21208, A21202, A31572, A31573, 1:200) according to the experiment's design. The samples were sequentially counterstained with DAPI (Beyotime, C1006) and underwent mounting in ProLong Diamond Antifade Mountant (Thermo Fisher Scientific, P36970).

Multiplexed immunofluorescence staining was performed using PANO4-plex MIF Kit (Panovue, 0079100020) following the manufacturer's protocol. <sup>124</sup> Briefly, after antigen retrieval and blocking, 4-µm-thick tissue sections were sequentially incubated with three primary antibodies: rabbit anti-mouse ASC-1 (GeneTex, GTX47874, 1:200), rabbit anti-mouse Nrg4 (GeneTex, GTX64845, 1:200) and rabbit anti-mouse Cytokeratin (Abcam, ab53280, 1:200), overnight at 4°C. The sections were subsequently incubated with the antirabbit HRP-conjugated secondary antibody (Panovue, 10015001030) at room temperature for 10 min, followed by incubation with tyramide signal amplification (TSA) fluorophores (PPD520, PPD620, PPD690) for 10 min. After each staining cycle, the sections underwent microwave heat treatment. Once staining was complete, all slides underwent counterstaining with DAPI for 5 min and were subsequently mounted using ProLong Diamond Antifade Mountant.

High-resolution images were captured using a confocal laser-scanning microscope (Leica TCS SP8 STED 3X) equipped with a  $40 \times \text{oil}$  immersion objective. For three-dimensional (3D) reconstructions, image stacks were acquired from the *z-stack* recordings, with frames taken at an average interstack interval of  $0.5 \, \mu \text{m}$ . Each sample had ten to  $15 \, z$  sections. Image reconstructions were performed using the Leica software package. The mean fluorescence intensity was quantified using the intensity plugin of the Leica software package. For colocalization analysis, Pearson's correlation coefficients between the values obtained on the Alexa Fluor 488 and 555 channels were measured using the colocalization plugin of the Leica software package.

For assessing exosome uptake by particular cell types, three sections with three random fields at 40  $\times$  magnification were captured for each mouse. Dil-labeled exosome-positive cells were counted using the cell counter plugin of ImageJ software. A similar method was employed to quantify the number of specific cells. The ratio of exosome-positive cells to the total number of specific cells was calculated

In some experiments,  $20-\mu m$ -thick cryosections of mammary tumors and adjacent mammary fat pads or livers were incubated with 1  $\mu g/mL$  BODIPY (Thermo Fisher Scientific, D3922) at 37°C for 30 min in darkness to detect the level of lipid. The section was rinsed with PBS three times and then counterstained with DAPI (Beyotime, C1006) at room temperature for 5 min. Images were captured with a confocal laser-scanning microscope (Leica TCS SP8 STED 3X) equipped with a 40  $\times$  oil immersion objective. The mean fluorescence intensity of BODIPY within the abnormal ducts, tumor areas, or liver tissues was quantified using the intensity plugin of the Leica software package.

# Liquid chromatography-tandem mass spectrometry (LC-MS/MS)

LC-MS/MS was conducted on protein of exosomes extracted from CM of normal or fatty livers of C57BL/6 mice. Briefly, 20 μg exosomal protein was denatured in 8 M urea, followed by reduction in 10 mM dithiothreitol (DTT, Sigma-Aldrich, 43816), and alkylation using 55 mM iodoacetamide (IAA, Sigma-Aldrich, A3221). After being washed with 300 μL acetonitrile (ACN, Sigma-Aldrich, 271004),

# **Cell Metabolism**





samples were freeze-dried and then digested with 300  $\mu$ L 0.01  $\mu$ g/ $\mu$ L trypsin (Promega, V5280) at 37°C overnight. The digestion was stopped using 300  $\mu$ L 10% trifluoroacetic acid (TFA). Resulted peptide mixtures were desalted using Oasis HLB 1cc (10 mg) Extraction Cartridges (Waters, 186000383), dried, and resuspended with 20  $\mu$ L 0.1% formic acid (FA). The peptide concentration was measured using the Pierce quantitative colorimetric peptide assay (Thermo Fisher Scientific, 23275). Peptidomic profiling was conducted on an Easy 1200 LC system with an Orbitrap Fusion mass spectrometer. Approximately 5  $\mu$ g peptides of each sample were separated by a 75  $\mu$ m  $\times$  150 mm capillary column packed with stationary phase (1.9  $\mu$ m particle size, C18 AQ) with an 8-38% B gradient (80% ACN, 0.1% FA, H<sub>2</sub>O) from 3 min to 53 min at a flow rate of 300 nL/min. An MS1 scan was accessed at a range of 350-1500 m/z (60000 resolution, auto injection time, 100% AGC, 1.0 s Cycle time, -45V/-60V Faims CV) followed by MS/MS data-dependent acquisition and detection in the lon trap, with parameters including 100% AGC, 30 NCE for HCD supplemental activation, and 1.6 m/z quadrupole isolation width.

Using Proteome Discoverer (v2.4.0) with Andromeda, peptidomic data were processed and aligned against an in-house constructed database based on Mus musculus (uniport-mouse-musculus-17440, fasta) and the endogenous regulatory oligopeptide knowledgebase (EROP). The tolerance for precursor MS was set to 10 ppm, and that for fragment MS/MS to 0.6 Da. Label-free quantification (LFQ) was used for data analysis in Proteome Discoverer. LC-MS/MS was conducted at the Bioinformatics and Omics Center, Sun Yat-Sen Memorial Hospital, Sun Yat-Sen University.

### siRNA transfection

Mouse primary hepatocytes were seeded in 6-well plates ( $2 \times 10^5$  cells per well). Following overnight incubation to allow cell attachment, siRNA transfection was carried out using the Lipofectamine RNAiMAX (Invitrogen, 13778030) in accordance with the manufacturer's protocol. Briefly, 25 pmol siRNAs and 5  $\mu$ L Lipofectamine RNAiMAX were mixed with 100  $\mu$ L Opti-MEM I Reduced Serum Medium (Gibco, 31985070) and added to each well. After 48 hr, cells were lysed and RNA was extracted for qRT-PCR analysis. In some experiments, the cultured medium was replaced with DMEM/F12 containing 10% exosome-depleted FBS and incubated for an additional 48 hr to collect CM for exosome isolation.

### Flow cytometry analysis of ErbB4 levels on exosomes

Exosomes were bound to latex beads before flow cytometry analysis as previously described.  $^{125}$  Briefly, 30  $\mu$ g exosomes in 100  $\mu$ L PBS were incubated with 10  $\mu$ L aldehyde/sulphate latex beads with 4- $\mu$ m diameter (Invitrogen, A37304) for 15 min at room temperature. Then the mixture was diluted to 1 mL with PBS and allowed to rotate for 30 min at room temperature. The reaction was stopped with 100 mM glycine in PBS containing 2% BSA, followed by incubation for 30 min at room temperature with agitation. Exosome-bound beads were washed once in 2% BSA in PBS and centrifuged at 14,800  $\times$  g for 1 min. The beads were subsequently blocked with 10% BSA at room temperature for 30 min with agitation, followed by a wash in 2% BSA and centrifugation at 14,800  $\times$  g for 1 min. The beads were then resuspended with 20  $\mu$ L 2% BSA in PBS and incubated with 3  $\mu$ L mouse anti-mouse ErbB4 antibodies (Santa Cruz Biotechnology, sc-8050) for 30 min with rotation at 4°C. After being washed with 2% BSA in PBS, the samples were resuspended with 20  $\mu$ L 2% BSA in PBS and incubated with 3  $\mu$ L Alexa Fluor 488-conjugated secondary antibodies (Thermo Fisher Scientific, A21202) for 30 min with rotation at 4°C. The beads were rinsed with 2% BSA, subjected to centrifugation at 14,800  $\times$  g for 1 min, and resuspended in 200  $\mu$ L 2% BSA in PBS. Beads only incubated with secondary antibodies were used as the control. The samples were examined by flow cytometry as aforementioned.

# **Enzyme-linked immunosorbent assay (ELISA)**

Exosomes were obtained from liver CM or primary hepatocyte CM of tumor-free mice fed either CD, HFrD or HFD, or from liver CM of EO771 tumor-bearing mice fed either CD or HFrD, or from CM of PA-treated AML12 cells, and quantified by NTA. ErbB4 levels on the surface of exosomes were quantified using the mouse ErbB4 ELISA kit (Abebio, AE45297MO) in accordance with the manufacturer's instructions. Briefly, exosome suspensions were added to a 96-well plate pre-coated with anti-mouse ErbB4 antibody ( $10^8$  exosomes in  $100~\mu$ L PBS for each well) and incubated at  $37^{\circ}$ C for 2 hr. After being washed three times, the plate was added with the biotin-conjugate antibody specific to ErbB4 ( $100~\mu$ L solution in each well) and incubated at  $37^{\circ}$ C for 1 hr. Then, the ELISA plate was washed three times, and  $100~\mu$ L horseradish peroxidase-conjugated streptavidin was added to each well and incubated at  $37^{\circ}$ C for 1 hr. After being washed three times, each well was filled with  $100~\mu$ L substrate solution and incubated at  $37^{\circ}$ C for 15-20 min. The reaction was stopped by adding  $50~\mu$ L stop solution to each well. Absorbance was measured at 450~nm using a microplate reader (TECAN Spark). Using the linear range of the ELISA data, the amount of ErbB4 present on exosomes surface was calculated

For detection of the exosomal TRMT10C levels, exosome suspensions were subjected to two cycles of 10-second pulse sonication using a Sonifier (Ultrasonics, VCX130, USA). The lysed exosome samples were then processed for TRMT10C analysis using the mouse TRMT10C ELISA kit (Abebio, AE22369MO) following the manufacturer's instructions. The absorbance and the concentration of TRMT10C were obtained as described above.

# **Gene knockout using CRISPR/Cas9**

Mouse sgRNAs targeting Sh3tc2, Pgrmc2, ErbB4, Gas2l2, Trpa1, Fatp1, Fatp4, Sgsm2, Timmdc1, Eif5, Ddx19a, Trmt10c or II6 were constructed using lentiCRISPR v2 vector (Addgene). As the control, a CRISPR-Cas9 vector containing a non-targeting sgRNA was utilized.





For Sh3tc2, Pgrmc2, ErbB4, Gas2l2, Trpa1, Sgsm2, Timmdc1, Eif5, Ddx19a and Trmt10c knockout in AML12 cells, Fatp1, Fatp4 and II6 knockout in EO771 cells, and Trmt10c knockout in 3T3-L1 pre-adipocytes, lentiviral transduction with indicated sgRNA was performed on  $5 \times 10^5$  cells placed in 6-well plates, with a multiplicity of infection (MOI) of 5 used for AML12 cells, 10 for EO771 cells, and 10 for 3T3-L1 pre-adipocytes, under conditions of  $37^{\circ}$ C,  $5 \mu g/mL$  polybrene (Sigma-Aldrich, TR-1003), and a 12-hour duration. Selection of cells was performed with 2.5  $\mu g/mL$  puromycin (MedChemExpress, HY-B1743A) over 2 weeks. Table S9 lists all targeting sequences.

### Online data analysis

Gene expression data of *Nrg1*, *Nrg2*, *Nrg3* and *Nrg4* across different mouse tissues were retrieved from the Gene database (Gene: 211323, 100042150, 18183, 83961).

# **Adipogenic differentiation**

3T3-L1 pre-adipocytes were induced to differentiate into adipocytes using a differentiation kit (HyCyte, EFMX-D102R) in accordance with the manufacturer's protocols. Briefly, 3T3-L1 pre-adipocytes were grown in DMEM containing 10% FBS until 90% confluency. Then cells were cultured with the differentiation induction complete medium for 72 hr, followed by culturing in differentiation maintenance complete medium for 24 h. A total of three circles of culture medium change were performed. The purity of differentiated adipocytes was confirmed to exceed 90% by detecting perilipin-1 expression using flow cytometry as aforementioned.

# Quantification of free fatty acid (FFA)

Levels of FFA released by cells *in vitro* and serum FFA were quantified as previously described. <sup>126,127</sup> Briefly, primary adipocytes were isolated from mammary fat pads, genital fat pads, mesenteric or perirenal fat tissues of C57BL/6 mice or MMTV-PyMT mice injected with exosomes derived from liver CM of CD-/HFrD-fed mice. Additionally, mammary adipocytes were isolated from CD-fed or HFrD-fed C57BL/6 mice, *Adipoq-Nrg4*<sup>Δ</sup> mice, MMTV-PyMT mice or PyMT; *Adipoq-Nrg4*<sup>Δ</sup> mice, or mice injected with or without exosomes derived from PA-treated AML12 cells or primary hepatocytes of HFrD-fed mice. Primary adipocytes were cultured in DMEM medium for 3 hr and the medium was then collected for FFA quantification. The concentration of FFA was measured using a colorimetric kit (Wako, 294-63601). The detergent-insensitive Pierce BCA protein assay kit was used to measure the protein concentration of the samples. The concentration of FFA was normalized to the concentration of protein to obtain a relative level of FFA.

In some experiments, 3T3-L1 adipocytes were cultured in DMEM medium supplemented with 10% FBS for 3 days in the presence or absence of PA-treated AML12 cell-derived exosomes ( $10 \mu g/mL$ ). Then, 3T3-L1 adipocytes were washed with PBS and cultured in fresh DMEM medium, which was collected for FFA quantification after 3 hr. 3T3-L1 adipocytes pretreated with H<sub>2</sub>O<sub>2</sub> ( $200 \mu M$ ) or N-acetyl-L-cysteine (NAC, 0.5 mg/mL) for 2 days after exosome incubation were used as positive and negative controls, respectively. In some experiments, 3T3-L1 adipocytes were pretreated with or without 40  $\mu M$  Atglistatin (MedChemExpress, HY-15859) or DMSO for 8 h at 37°C. Then the medium was replaced by DMEM and incubated for an additional 3 hr at 37°C with or without 40  $\mu M$  Atglistatin. The culture medium was collected for FFA quantification.

For quantification of serum FFA levels, four-week-old female C57BL/6 mice were administered intravenously without or with 30  $\mu$ g exosomes isolated from liver CM of HFrD-fed mice for four weeks. Then, serum samples were collected and used for FFA quantification.

# Assessment of lipid transfer between cells

To assess lipid transfer between cells, a co-culture experiment was performed as previously described. Briefly, 3T3-L1 adipocytes or primary adipocytes isolated from mouse mammary fat pads ( $1 \times 10^4$  cells per well) were cultured in the upper chamber of a 6-well transwell system with a 0.4- $\mu$ m membrane (Corning, 3412). In some experiments, 3T3-L1 adipocytes were pretreated *in vitro* without or with 10  $\mu$ g/mL exosomes isolated from liver CM of CD-fed or HFrD-fed mice, or exosomes isolated from CM of PA-treated AML12 cells for 3 days. Cells were subsequently stained with BODIPY stain (Invitrogen, D3922, 1  $\mu$ g/mL in PBS) for 4 hr at 37°C to label intracellular lipids. Subsequently, adipocytes were washed three times with 1  $\times$  PBS containing 0.2% fatty acid-free BSA to remove the uncombined dye. EO771 cells were cultured in 6-well plates ( $5 \times 10^4$  cells per well) and cultured overnight. The 6-well 0.4- $\mu$ m transwells containing BODIPY-labeled adipocytes were then placed onto the wells containing EO771 cells in 6-well plates and co-cultured for 24 h. EO771 cells were harvested and washed with PBS. EO771 cells positive for BODIPY were detected by flow cytometry or immunofluorescence staining.

# **Isolation of primary tumor cells**

Primary tumor cells were isolated from mammary tumors of 22-week-old MMTV-PyMT mice and EO771 tumor-bearing C57BL/6 mice as previously described.  $^{129,130}$  Briefly, tumors were minced into small pieces and digested in 10 mL DMEM/F12 medium containing 2 mg/mL collagenase type I (Biofroxx, 1904GR001) and 2% BSA with gentle shaking (80 rpm) at 37°C for 1 hr. Undigested tissues were filtered out using a 70- $\mu$ m cell strainer. Following centrifugation at 300  $\times$  g for 3 min, pellets were resuspended in 100  $\mu$ L PBS with 2% BSA and 2 mM EDTA and incubated with CD326 (Ep-CAM) Microbeads (Miltenyi Biotec, 130105958) at 4°C for 15 min. Ep-CAM-positive tumor cells were isolated using LS columns (Miltenyi Biotec, 130-042-401) in accordance with the manufacturer's protocols. Total RNA was then extracted from tumor cells and analyzed using qRT-PCR analysis.

# **Cell Metabolism**

# **Article**



# **Quantitative real-time PCR (qRT-PCR)**

Trizol reagent (Invitrogen, 15596026CN) was used to extract total RNA from cells or tissues according to the manufacturer's protocols. The extracted RNA was then reverse transcribed into cDNA using Hifair III 1st Strand cDNA Synthesis Kit (YEASEN, 11141ES60). Quantitative real-time PCR was conducted using TB Green Premix Ex Taq II (Tli RNaseH Plus) (Takara, RR820A). The calculation of relative gene expression levels was performed with reference to the internal control. Table S9 contains the primer sequences.

### **Lentiviral vector-mediated overexpression**

To induce mouse TRMT10C overexpression in AML12 cells or 3T3-L1 pre-adipocytes, the sequence encoding mouse TRMT10C was inserted into the lentiviral vector pCDH-CMV-MCS-EF1-Puro. AML12 cells or 3T3-L1 pre-adipocytes ( $5 \times 10^5$  cells per well) placed in 6-well plates underwent transduction with lentiviral particles, with 5  $\mu$ g/mL polybrene at 37°C for 12 hr; the MOI was 5 for AML12 cells and 10 for 3T3-L1 pre-adipocytes. For IL-6 overexpression in 3T3-L1 pre-adipocytes, the sequence encoding mouse IL-6 was inserted into the lentiviral vector pCDH-CMV-MCS-EF1-Puro. 3T3-L1 pre-adipocytes ( $5 \times 10^5$  cells per well) in 6-well plates were transduced with lentiviral particles (MOI of 10) and 5  $\mu$ g/mL polybrene in 6-well plates at 37°C for 12 hr.

For mouse mitochondrial ND5 and ND6 overexpression in 3T3-L1 pre-adipocytes, nuclear-form Nd5 or Nd6 genes, with the mitochondrial targeting sequence from subunit VIII of mouse cytochrome c oxidase added to the 5'-terminus<sup>131</sup> were directly synthesized and subcloned into the lentiviral vector pCDH-CMV-MCS-EF1-Puro. Then  $5 \times 10^5$  3T3-L1 pre-adipocytes were transduced with lentiviral particles (MOI of 10) and  $5 \mu g/mL$  polybrene in 6-well plates at  $37^{\circ}$ C for 12 hr. The vectors were designed and constructed by IGEbio (Guangzhou, China). To obtain resistant cells, the cells were selected with 2.5  $\mu g/mL$  puromycin over a 2-week period.

# Lipidomic analysis

Lipids were extracted from purified exosomes as previously described. <sup>132</sup> Briefly,  $1.5 \times 10^{10}$  exosomes isolated from liver CM of CD-fed or HFrD-fed mice or from CM of PA-treated AML12 cells were suspended in 100  $\mu$ L PBS and mixed with 900  $\mu$ L precooled lipid extraction solution (chloroform: methanol = 2:1). The mixture was vortexed vigorously for 30 s. Samples were incubated at -20°C for 1 hr for complete lipid partitioning. To achieve phase separation, centrifugation was performed at 14,000  $\times$  g for 20 min at 4°C. Then the lipid-containing chloroform phase (lower layer) was carefully collected using a syringe to avoid interface contamination, transferred to a clean vial, and freeze-dried. Analysis of dried lipid extracts was performed by ultra-performance liquid chromatography-tandem mass spectrometry (UPLC-MS/MS) as previously described. <sup>132</sup> Briefly, reconstitution of lipid extracts was performed in 100  $\mu$ L isopropanol/acetonitrile/water (2:1:1, v/v/v) and normalization was carried out using protein concentration derived from the protein disc retained during lipid extraction. Chromatographic separation was performed using an Ultimate 3000 UPLC system (ThermoFisher Scientific, United States) equipped with a Waters Acquity UPLC BEH C18 column (particle size, 1.7  $\mu$ m; 100 mm (length)  $\times$  2.1 mm (i.d.)) and coupled to Orbitrap Exploris 480 mass spectrometer. The mobile phases consisted of mobile phase A, consisting of LC-MS grade water: acetonitrile (4:6, v/v), 10 mM ammonium acetate and 0.1% formic acid. The flow rate was 0.35 mL/min and the gradient was set as follows: 0-2 min,30% B to 43% B, 2-2.1 min, 43% B to 55% B, 2.1-12 min, 55% B to 65% B, 12-18 min, 65% B to 85% B, 18-18.5 min, 85% B to 100%, 18.5-19.5 min, 100% B, 19.5-20 min, 100% B-30% B, 20-23 min, 30% B.

The acquisition of data was carried out in full MS scan mode and ddMS2 scan mode for positive and negative electrospray ionization with the following parameters: spray voltage 3.5 kV (ESI+) or 3.0 kV (ESI-), sheat gas (Arb):50, ion transfer tube temp (°C):350, vaporizer temp (°C):350. The full scan range (m/z) was set as 114-1700, and orbitrap resolution was 60000. For the ddMS2 scan mode, the scan range mode was set as defined m/z range and the scan range was set as 114-1700. A resolution of 30,000 was set for the MS and the HCD collision energy (%) was set as 25,35,45. The raw data was acquired using Xcalibur software and the lipidomic identification was performed using LipidSearch 4.0.

# **Cell proliferation assay**

Hepatocytes isolated from CD-fed or HFrD-fed mice were cultured for 48 hr. Following collection, CM underwent filtration through a 0.22- $\mu$ m filter and was then diluted 1:1 with complete RPMI 1640. <sup>133</sup> EO771 cells were seeded in a 96-well plate, with 1,000 cells per well. After adherence, EO771 cells were treated with diluted CM for 24 h. The Cell Counting Kit-8 (CCK-8) was used to assess the proliferation of EO771 cells in line with the manufacturer's instructions. Briefly, cultured medium was replaced with 100  $\mu$ L fresh RPMI 1640, and 10  $\mu$ L CCK-8 (APExBIO, CCK8-K1018-5) was added into each well (time point set as 0 hr). Then, the plate was incubated at 37 °C for 60 min, after which the absorbance at 450 nm was read using a TECAN Spark microplate reader. Cell proliferation assays were also performed at time points of 24, 48, 72 and 96 hr.

In some experiments, 3T3-L1 adipocytes were seeded in the upper chamber of a 96-well 0.4- $\mu$ m transwell system (Corning, 3381) and treated with or without 10  $\mu$ g/mL exosomes from liver CM of CD-fed or HFrD-fed mice, in the absence or presence of 40  $\mu$ M Atglistatin (MedChemExpress, HY-15859) for three days. Then, 3T3-L1 adipocytes were washed with PBS and the cultured medium was replaced with 2 mL fresh DMEM without FBS. After 3 hr, the medium was collected for FFA quantification. In some experiments, EO771 cells (1,000 cells per well) were seeded in the lower chamber of a 96-well plate and cultured overnight to allow adherence. The 96-well 0.4- $\mu$ m transwells containing indicated 3T3-L1 adipocytes were then placed onto the wells containing EO771 cells in 96-well plates and co-cultured. Cell proliferation assays were performed at time points of 0, 24, 48, 72 and 96 hr.





### Cytosolic and mitochondrial fractionation

Cytosolic and mitochondrial fractions were prepared from primary adipocytes using the isolation kit (Thermo Fisher Scientific, 89874) in accordance with the manufacturer's instructions. 97 Briefly, 1 × 106 primary adipocytes from C57BL/6 mice mammary fat pads were incubated for 15 min in 2 mL ice-cold mitochondria isolation buffer. After homogenizing the cells, nuclei and unbroken cells were removed by centrifuging at  $600 \times g$  for 10 min. Samples were then centrifuged at  $10,000 \times g$  for 10 min. The mitochondrial fraction-containing pellet and the cytosolic fraction-containing supernatant of cells were were collected separately. Cell fractions were then lysed in RIPA lysis buffer for western blot analysis or in TRIzol reagent (Invitrogen, 15596026CN) for RNA extraction.

### **Mitochondrial RNA purification**

Total mitochondrial RNA was isolated from mitochondrial fractions of primary adipocytes or 3T3-L1 adipocytes as aforementioned. Purification of Poly (A)+ mRNA was performed using the Hieff NGS mRNA Isolation Master Kit (YEASEN, 12603ES24) following the manufacturer's protocol. The mirVana miRNA Isolation Kit (Invitrogen, AM1561) was used to isolate the small RNA fraction (200 ng; <200 nucleotides (nt), primarily consisting of mature tRNA)<sup>134</sup> from total mitochondrial RNA, in accordance with the manufacturer's protocol. 135

### Quantitative analysis of RNA modification levels using UPLC-MS/MS

RNA modification levels were measured using UPLC-MS/MS assay as previously mentioned. Briefly, purified RNAs (200 ng) were digested into nucleosides using 180 U/µL S1 nuclease (Takara, 2410A), 30 U/µL alkaline phosphatase (Takara, 2250A) and 0.002 U/μL phosphodiesterase I (Sigma-Aldrich, P3243-1VL) for 3 hr at 37°C. After the solution was complete hydrolysis, 10 μL of it was subjected to ultraperformance LC-MS/MS analysis. Separation of the nucleosides occurred on a C18 column (1.8 μm, 2.1 mm × 100 mm), with detection performed by a triple quadrupole-linear ion trap mass spectrometer (QTRAP), QTRAP LC-MS/ MS System, which features an ESI Turbo Ion-Spray interface. Controlled by Analyst 1.6.3 software (Sciex), the system functioned in positive and negative ion modes. Nucleosides quantification relied on the nucleoside-to-base ion mass transitions of 268.1 to 136.2 (A), 282.1 to 150.2 ( $m^{1}$  A), 284.1 to 152.2 (G), and 298.1 to 166.1 ( $m^{1}$  G). Standard curves for the pure nucleosides of each methylated base were utilized to calculate RNA modification levels.

### m<sup>1</sup>A RNA immunoprecipitation-qPCR

m<sup>1</sup>A RNA immunoprecipitation-qPCR (m<sup>1</sup>A-RIP-qPCR) was conducted as previously described.<sup>60,61</sup> Briefly, mitochondrial RNAs were extracted from mammary adipocytes or 3T3-L1 adipocytes as aforementioned. Then, 2 μg mitochondrial RNAs were mixed with 1 μg rabbit anti-mouse m<sup>1</sup>A antibodies (Abcam, ab208196) in 100 μL IP buffer at 4°C overnight. Then, 5 μL Pierce Protein A/G beads (Thermo Fisher Scientific, 88802) were added to the mixture, and incubation proceeded for 1 hr at room temperature. Following three washes with IP buffer, elution of RNAs was done twice using elution buffer. m<sup>1</sup>A IP RNAs were then recovered through ethanol precipitation. Input and immunoprecipitated RNAs were subjected to qRT-PCR analysis.

# Oxygen consumption rate (OCR) assay

Mitochondrial function of 3T3-L1 adipocytes was assessed using the Seahorse XF96 analyzer (Agilent) as previously described.<sup>64</sup> Briefly, 2,000 3T3-L1 adipocytes per well in gelatin-coated XF96 cell culture microplates were washed with pre-warmed Seahorse XF Base Medium (pH 7.4) for two times. Then, cells were allowed to equilibrate for 60 min in pre-warmed Seahorse XF Base Medium (pH 7.4) containing 25 mM glucose and 1 mM pyruvate, placed in a 37°C incubator without CO2. Cells were then moved to a temperature-controlled Seahorse analyzer to measure basal respiration parameters. The mitochondrial stress test was performed with sequential treatment of the following reagents. Oligomycin (1 μM), which acts as a coupled respiration inhibitor, was added, and respiration measurements were conducted to evaluate ATP production and proton leak. Maximal respiration was measured after the addition of 2.0 µM flurorcarbonyl cyanide phenylhydrazone (FCCP). Spare respiratory capacity and nonmitochondrial respiration were then assessed following the addition of 0.5 μM rotenone and 0.5 μM antimycin A. Data were analyzed using the Wave software (Agilent Technologies).

### Mitochondrial ribosome profiling

Mitochondrial ribosome profiling was performed as previously reported. 62 Briefly, 3T3-L1 adipocytes were rapidly rinsed with icecold PBS containing 100 μg/mL chloramphenicol (Sigma-Aldrich, C0378) and 100 μg/mL cycloheximide (Sigma-Aldrich, 239765) followed by immediate immersion into liquid nitrogen. Cells were then put on ice and incubated with 1 mL 1.5 x lysis buffer. Cell lysates were homogenized and centrifuged at 5,000 × g for 10 min. The supernatant was digested with 7,500 U/mL micrococcal nuclease (Beyotime, D7201S) in the presence of 40 μL SUPERase-IN RNase inhibitor (Invitrogen, AM2696) and 5 mM CaCl<sub>2</sub>. After 1 hr of gentle shaking at 25°C, digestion was stopped using EGTA with a final concentration of 6 mM. A 5%-45% gradient sucrose solution was prepared using a fully automated density gradient preparation and separation system (Biocomp, Canada). The sample was layered onto 11 mL 5%-45% sucrose gradients and centrifuged at 210,000  $\times$  g for 2.5 hr at 4°C using the Beckman SW-41Ti rotor. Live UV absorption at 254 nm was used to track the mitochondrial polysome-enriched fractions (Biocomp, Canada). The fractions resulting from the sucrose gradient were used for protein and RNA extraction.

RNA was extracted from each fraction using TRIzol reagent. Protein was extracted from each fraction as previously described. 136 Briefly, 150 μL of each fraction was precipitated using methanolcholoform-H<sub>2</sub>O precipitation with sequential addition of 600 μL ice-

# **Cell Metabolism**



**Article** 

cold methanol, 225  $\mu$ L chloroform and 450  $\mu$ L H<sub>2</sub>O. After being thoroughly inverted, the mixture was centrifuged at 20,000  $\times$  g for 4 min at 4°C. After the aqueous layer was carefully removed, 1 mL pre-chilled methanol was added, mixed by inversion, and centrifuged again at 20,000  $\times$  g for 4 min at 4°C. After discarding the supernatant, the protein pellet underwent air-drying at room temperature. Then, 50  $\mu$ L 1  $\times$  NuPAGE LDS-Sample buffer was added, and frequent pipetting was performed to dissolve the protein pellets. Since cytoplasmic fractions 1-3 had a higher protein abundance, 2  $\mu$ L of these fractions, and 20  $\mu$ L fractions 4-9 (representing different ribosomal fractions) were loaded onto an SDS-PAGE to perform western blot analysis.

### **ATGL** activity assay

The EnzChek lipase substrate (Thermo Fisher Scientific, E33955) was used to detect ATGL activity as previously mentioned with slight modifications.  $^{137,138}$  Briefly, primary mammary adipocytes or 3T3-L1 adipocytes were washed with cold PBS and lysed in 20 mM Tris-HCl and 0.0125% Zwittergent 3-18 (Sangon Biotech, A600556-0001) by repeated passage through a 30-gauge syringe. The protein concentration of cell lysates was measured using a BCA assay and normalized to 2.0 mg/mL. The microplate reader (TECAN Spark) was used for fluorescence measurements. The maximum excitation and emission wavelengths were identified as 482 nm and 515 nm, respectively, with a 495 nm filter cutoff. The ATGL activity assay was conducted at 37°C in a black 96-well plate (Corning, 3915). The cell lysate (50  $\mu$ g) was incubated with 0.62  $\mu$ M EnzChek lipase substrate in the presence of 0.15 M NaCl, 20 mM Tris-HCl (pH 8.0), 0.0125% Zwittergent 3-18 and 1.5% fatty acid-free BSA in a total volume of 100  $\mu$ L. All samples were carried out in triplicate. Relative fluorescent unit (RFU) of each well was recorded at 9 min, with background hydrolysis values subtracted. The ATGL activity of each sample was calculated as the ratio of its RFUs to those of the control group and shown as the relative fluorescence.

### Detection of ErbB4<sup>+</sup> exosomes in human plasma

Collection of fresh human plasma was done in sterile tubes, followed by immediate storage at -80°C. Cryopreserved human plasma was thawed on ice before use. Plasma was diluted with PBS (200  $\mu$ L to 11 mL) as previously described with minor modifications<sup>20</sup> and followed by centrifugation at 2,000  $\times$  g for 20 min to get rid of cellular and tissue debris.<sup>31</sup> The sample was subsequently centrifuged at 16,500  $\times$  g for 45 min at 4°C to remove microvesicles. The resulting supernatant was then centrifuged at 100,000  $\times$  g for 2 hr at 4°C.<sup>31</sup> After being washed with PBS, the pelleted exosomes were centrifuged at 100,000  $\times$  g at 4°C for 70 min, followed by resuspension in 100  $\mu$ L PBS for flow cytometry analysis.

# **QUANTIFICATION AND STATISTICAL ANALYSIS**

Statistical analyses were conducted using GraphPad Prism 9.0, unless specified otherwise in the figure legends or methods. Results are presented as mean  $\pm$  standard deviation (SD), with reproducibility verified by carrying out at least three independent experiments. Statistical mean comparisons were performed using Student's t-test or the Mann-Whitney U test for two groups, and for multiple groups, one-way ANOVA or Kruskal-Wallis test, or two-way ANOVA followed by Tukey's multiple comparison test, unless stated otherwise. Plots of Kaplan-Meier survival curves were created, with the log-rank test applied to make comparisons between the survival curves. The optimal cutoff point was determined using X-tile statistical software. Multivariable Cox regression analysis was employed to identify independent prognostic factors. P < 0.05 was considered statistically significant. Sample sizes in this study are comparable to those reported in previous publications.